



Delft University of Technology

Remote Sensing of Damage Feedbacks and Ice Shelf Instability in Antarctica

Izeboud, M.

DOI

[10.4233/uuid:f3b71918-9432-484f-81d0-51d00be2baf1](https://doi.org/10.4233/uuid:f3b71918-9432-484f-81d0-51d00be2baf1)

Publication date

2024

Document Version

Final published version

Citation (APA)

Izeboud, M. (2024). *Remote Sensing of Damage Feedbacks and Ice Shelf Instability in Antarctica*. [Dissertation (TU Delft), Delft University of Technology]. <https://doi.org/10.4233/uuid:f3b71918-9432-484f-81d0-51d00be2baf1>

Important note

To cite this publication, please use the final published version (if applicable).
Please check the document version above.

Copyright

Other than for strictly personal use, it is not permitted to download, forward or distribute the text or part of it, without the consent of the author(s) and/or copyright holder(s), unless the work is under an open content license such as Creative Commons.

Takedown policy

Please contact us and provide details if you believe this document breaches copyrights.
We will remove access to the work immediately and investigate your claim.

An abstract painting with thick, textured brushstrokes in shades of blue, white, yellow, and brown, suggesting a rugged, icy landscape. The composition is dominated by diagonal and horizontal strokes, creating a sense of depth and movement. The colors are layered, with some areas appearing more saturated than others, giving it a dynamic and somewhat chaotic feel.

Remote Sensing of Damage on Antarctic Ice Shelves

Maaïke Izeboud

Remote Sensing of Damage Feedbacks and Ice Shelf Instability in Antarctica

Maaïke Izeboud

Remote Sensing of Damage Feedbacks and Ice Shelf Instability in Antarctica

Proefschrift

ter verkrijging van de graad van doctor
aan de Technische Universiteit Delft,
op gezag van de Rector Magnificus prof. dr. ir. T.H.J.J. van der Hagen,
voorzitter van het College voor Promoties,
in het openbaar te verdedigen op maandag 28 oktober 2024 om 15:00 uur

door

Maaïke IZEBOUD

Master of Science in Civil Engineering, Technische Universiteit Delft, Nederland,
geboren te Vlissingen, Nederland.

Dit proefschrift is goedgekeurd door de promotoren.

Samenstelling promotiecommissie:

Rector Magnificus,	voorzitter
Dr. S.L.M. Lhermitte,	TU Delft / KU Leuven, Belgium, <i>promotor</i>
Prof. dr. ir. R.F. Hanssen,	TU Delft, <i>promotor</i>

Onafhankelijke leden:

Prof. dr. E. Eisemann,	TU Delft
Prof. dr. A.E. Hogg,	University of Leeds, United Kingdom
Prof. dr. R.S.W. van de Wal,	Universiteit Utrecht
Dr. R.C. Lindenberg,	TU Delft
Prof. dr. S.C. Steele-Dunne,	TU Delft

Overig lid:

Dr. ir. B. Wouters,	TU Delft
---------------------	----------



Nederlandse Organisatie voor Wetenschappelijk Onderzoek

Keywords: Damage, Antarctica, Ice Shelves,
Multi-Source Remote Sensing, Machine Learning

Printed by: Ridderprint || www.ridderprint.nl

Cover: Artistic impression of the shear zone at Pine Island Glacier,
by M. Izeboud, oil on board.

Copyright © 2023 by M. Izeboud

ISBN 978-94-6506-476-5

An electronic version of this dissertation is available at
<http://repository.tudelft.nl/>.

Ik heb het nog nooit gedaan, dus ik denk dat ik het wel kan.

Vaak (ten onrechte) toegeschreven aan Pippi Langkous



Contents

Summary	1
Samenvatting	3
1 Introduction	7
1.1 The Antarctic Ice Sheet	7
1.1.1 Antarctic mass balance	9
1.2 The importance of ice shelves	9
1.2.1 Ice shelf instability	11
1.3 Damage on ice shelves	13
1.3.1 Damage types and traits	13
1.3.2 Modelling fractures, damage and calving	14
1.3.3 Challenges with damage modelling	15
1.4 Damage observed with remote sensing data	17
1.4.1 Data types	17
1.4.2 Challenges with detecting damage from observations	18
1.5 Research Objectives	19
1.6 In this thesis	20
2 Damage Detection with NeRD	23
2.1 Introduction	24
2.2 Normalised Radon transform Damage detection (NeRD)	25
2.2.1 The Normalised Radon Transform	27
2.2.2 Damage Signal and Orientation	28
2.2.3 Proof of Concept	29
2.3 Study Area and Data	30
2.3.1 Study Area	30
2.3.2 Satellite Imagery	32
2.4 Methods	33
2.4.1 Sensitivity Analysis	33
2.4.2 Application of NeRD	35
2.4.3 Validation	36
2.5 Results	37
2.5.1 Sensitivity Analysis	37
2.5.2 Damage Detection at the Amundsen Sea Embayment	42
2.5.3 Validation	43
2.5.4 Damage Evolution	46
2.6 Discussion	49
2.7 Conclusion	50

3	Assessment of Antarctic damage change over two decades	53
3.1	Introduction	54
3.2	Data for damage detection	54
3.2.1	Satellite observations	55
3.2.2	Annual Ice Shelf Masks	56
3.3	Methods	56
3.3.1	Damage detection with NeRD algorithm	56
3.3.2	Damage quantification	57
3.3.3	Damage observation uncertainty	57
3.4	Results	58
3.4.1	Antarctic wide damage	58
3.4.2	Observations of damage change	59
3.4.3	Damage development & ice shelf retreat	61
3.5	Discussion	62
3.6	Conclusion	64
4	Antarctic ice shelves vulnerable to damage in future climate warming	67
4.1	Introduction	68
4.2	Data for damage predictor	68
4.2.1	Feature selection	68
4.2.2	Observational data	69
4.2.3	ISMIP-6 ice sheet model data	69
4.2.4	Spatial resolution	70
4.3	Random Forest model development	70
4.3.1	Training, testing and validation datasets	70
4.3.2	Hyperparameter tuning	71
4.3.3	Projected damage change ensembles	71
4.4	Results	73
4.4.1	Damage link to ice dynamics	73
4.4.2	Damage projected in future climate scenarios	75
4.5	Discussion	76
4.6	Conclusion	78
5	Conclusions and perspectives	81
5.1	Automated damage detection method	81
5.2	Assessment of damage and damage change related to ice shelf retreat	82
5.3	Impact of damage on ice shelf stability	83
5.4	Perspectives and recommendations	84
5.4.1	Model evaluation with damage detected from observations	84
5.4.2	Towards monitoring fracture initiation and calving	85
5.5	Final note	86
A	Appendix: Code and Data Availability	89
B	Appendix: Supplementary Figures for Chapter 2	91
C	Appendix: Supplementary Material for Chapter 3 and 4	97
D	Appendix: Some more damage maps	105

CONTENTS

Bibliography	109
Acknowledgements	119
List of paintings	121
Curriculum Vitae	122
List of Publications and Presentations	123

Summary

The timing and magnitude of global sea level rise remains difficult to predict, driven for a large part by the potential instability of ice shelves in Antarctica. Ice shelves, the floating extension of the Antarctic ice sheet, govern the mass loss of the ice sheet by providing resistance (buttressing) to the grounded ice — thereby modulating the ice flow to the ocean. The short-term collapse or long-term weakening of ice shelves can result in drastic increases of ice discharge and Antarctic mass loss. Understanding the processes that affect the weakening, retreat, and instability of ice shelves is therefore essential in order to improve sea level rise predictions.

Damaged areas on ice shelves, consisting of fractures, crevasses and/or rifts, are first indicators of its weakening. As ice shelves weaken, they can provide less buttressing to the ice sheet, causing accelerated ice flow, heightened internal stress, and increased strain rates. This creates a feedback loop, further promoting damage development and ice mass loss through increased discharge. Moreover, the propagation of crevasses or rifts through the ice shelf eventually leads to calving of (often large) ice bergs. Observable damage is therefore an important precursor to this mode of mass loss. Damage has been considered key for the collapse of the Larsen B ice shelf and the retreat of Pine Island Glacier and Thwaites Glacier. Despite its significance for future ice shelf stability, damage processes remain one of the least understood in marine ice sheet dynamics. This dissertation therefore aims to improve our understanding of damage impacts on ice shelf weakening and retreat from an observational perspective.

First, a new, automated method was developed that can detect fractures and damage areas in satellite imagery across the Antarctic domain (Chapter 2). Quantifying damage effectively and accurately is a challenging task, caused by the complex surface of Antarctica, cloud and snow cover, illumination/viewing angles, and variable signal-to-noise levels in satellite imagery. The Normalised Radon Transform Damage detection (NeRD) method overcomes these challenges and robustly captures multiple scales of damage features and their orientations. A major novelty of NeRD is its straightforward applicability to different optical or radar satellite imagery of any spatial resolution.

NeRD is used to produce unprecedented observational assessments of Antarctic-wide damage changes over the past decades (Chapter 3). Damage maps were produced for 1997 and annually between 2015-2021, showing both long-term changes and short-term variations. The observations reveal a long-term overall reduction of damage, attributed to the calving of compromised ice shelf regions. The most significant reductions are observed in the Amundsen Sea Embayment and Bellingshausen Sea Embayment sectors. On the majority of ice shelves, a cyclic growth and decline of damaged areas is detected that is strongly correlated to ice shelf area changes. These observations demonstrate the link between damage-induced weakening and subsequent calving and retreat.

To better understand the relationship between damage and ice shelf weakening, a Random Forest regression (machine learning) model was constructed based on the damage maps and observations of key ice flow parameters (Chapter 4). This model was used to provide projections of damage changes in future climate scenarios, based on projected values of the ice flow parameters. The projections highlight the sensitivity of future damage development to emission pathways. Intensified damage development is predicted under high emission (warming) scenarios, particularly in regions where ice shelves thin and accelerate. Largest vulnerabilities are predicted in the Amundsen, East Indian, and Ross Sea Sectors.

The analyses and assessments of this dissertation confirm two main pathways of how damage impacts ice shelf stability and Antarctic mass loss: damage directly leads to ice shelf calving and retreat while the weakening of the ice shelf indirectly leads to mass loss through accelerated ice discharge. New insights are obtained by showing the sensitivity of damage-induced ice shelf weakening and retreat to future climate warming. However, damage processes will need to be better constrained in order to quantify its impact on Antarctic mass loss. We therefore underscore the importance of including damage impacts in ice sheet models and are hopeful that the produced damage maps can be of use in this endeavor, as without doing so we are likely underestimating future ice shelf retreat and Antarctic mass loss.

Samenvatting

De snelheid en hoogte van zeespiegelstijging in de komende jaren blijft lastig te voorspellen, met name vanwege een onzekere hoeveelheid massaverlies van de Antarctische ijskap. Deze onzekerheid wordt vooral bepaald door de potentiële instabiliteit van de ijsplaten in Antarctica. Ijsplaten, de drijvende uiteindes van de Antarctische ijskap, behouden het massaverlies van de ijskap door weerstand te bieden tegen de ijsstroom van land naar zee. Het verzwakken of instorten van de ijsplaten kan leiden tot een drastische toename van de ijsafvoer en dus het massaverlies van Antarctica. Het is daarom essentieel om ons inzicht in het (eventuele) destabiliseren van ijsplaten te verbeteren, zodat de voorspellingen van zeespiegelstijging kunnen worden verbeterd.

Beschadigde gebieden op een ijsplaat, bestaande uit breuken, spleten, scheuren of kloven in het ijs, zijn de eerste tekenen van verzwakking. Verzwakte ijsplaten kunnen minder weerstand bieden tegen de ijskap, wat leidt tot een snellere ijsstroom en meer interne spanning en rek. Dit bevordert vervolgens weer de ontwikkeling van extra schade en scheuren, waardoor een sneeuwbal effect ontstaat die de ijsplaat in toenemende mate verzwakt en het verlies van ijsmassa versterkt. Daarnaast zorgt de opening en groei van scheuren of kloven door de ijsplaat uiteindelijk tot het afkalven van (vaak grote) ijsbergen. Het opdoemen van ijsscheuren en -breuken is daarom een belangrijk symptoom van deze vorm van massaverlies. Ijsscheuren hebben een sleutelrol gehad bij het instorten van de Larsen B ijsplaat en het terugtrekken van de Pine Island en Thwaites ijsplaten. En, ondanks het belang van ijsscheuren op de toekomstige stabiliteit van ijsplaten, zijn de processen omtrent verzwakking één van de minst goed begrepen in de dynamica van de ijskap. In dit proefschrift was het doel daarom om de invloed van ijsscheuren op de stabiliteit van ijsplaten beter te begrijpen, vanuit het perspectief van observaties.

Als eerste is een nieuwe, geautomatiseerde methode ontwikkeld om ijsscheuren te detecteren in satelliet beelden van Antarctica (hoofdstuk 2). Het effectief en nauwkeurig detecteren van ijsscheuren in satelliet beelden is echter een uitdagende taak vanwege het ruwe oppervlak van Antarctica, bewolking of sneeuwbedekking die het zicht ontnemen, een veranderende lichtinval of kijkhoek van de satelliet, en de hoeveelheden ruis in de data. De NormalisEd Radon Transform Damage detection (NeRD) methode overkomt deze uitdagingen en kan op robuuste wijze de ijsscheuren, spleten en kloven, alsmede hun oriëntatie, identificeren. NeRD is een unieke methode die direct kan worden toegepast op zowel optische als radarbeelden van verschillende resolutie.

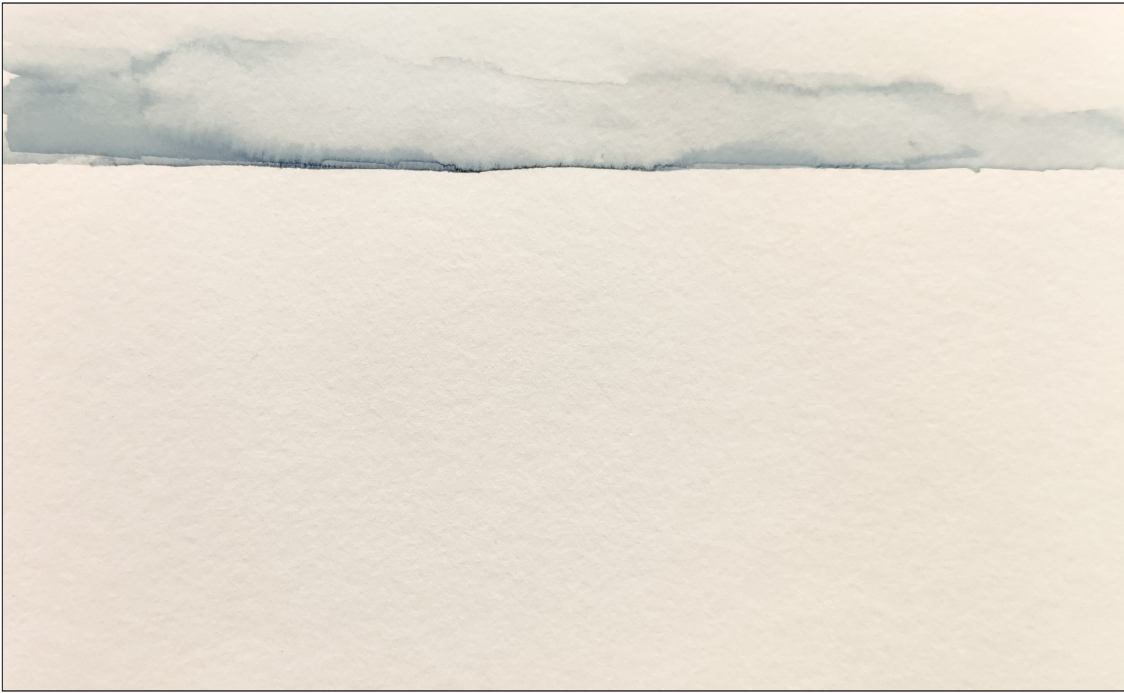
NeRD is vervolgens toegepast om nieuwe, ongeëvenaarde scheurkaarten van Antarctica te produceren, en voor het eerst de veranderingen van beschadigingen op ijsplaten in de afgelopen decennia te bepalen (hoofdstuk 3). Er zijn scheurkaarten gemaakt voor 1997 plus jaarlijks tussen 2015-2021, die zowel langetermijnveranderingen als kortere variaties laten zien. De waarnemingen laten een algehele afname van beschadigde gebieden op de lange termijn zien, vanwege het afkalven en verdwijnen van deze stukken ijsplaat. De grootste afname wordt waargenomen in de Amundsen- en Bellingshausen

zeebaai. Op de meeste ijsplaten wordt een cyclische groei en afname van beschadigde gebieden waargenomen, wat sterk gecorreleerd blijkt met veranderingen in het ijsplaatoppervlak. Deze waarnemingen tonen het verband aan tussen de door scheuren veroorzaakte verzwakking en het daaropvolgend afbreken van de ijsplaat.

Om het verband tussen ijsscheuren en verzwakking van de ijsplaat beter te begrijpen, werd een Random Forest regressiemodel (machine learning) opgesteld, aan de hand van observaties van belangrijke parameters voor de ijsstroom (hoofdstuk 4). Dit model kon vervolgens projecties maken van ijsplaatverzwakking voor toekomstige klimaatscenario's. De voorspellingen laten zien dat de hoeveelheid verzwakking op ijsplaten afhangt van de hoeveelheid klimaatwarming. In scenario's met hoge broeikasgas uitstoot wordt een ergere mate van verzwakking voorspeld. Kwetsbare ijsplaten zijn met name de ijsplaten die dunner worden en versnellen, zoals in de Amundsen zeebaai, Oost-Indische zee-sector en de Ross zee-sector.

De waarnemingen en analyses omtrent ijsplaatverzwakking in dit proefschrift bevestigen de tweevoudige invloed van ijsscheuren op de stabiliteit van ijsplaten en uiteindelijk massaverlies in Antarctica: ijsscheuren zorgen voor het afbreken en verdwijnen van ijsplaten, en de algemene verzwakking zorgt voor meer ijsmassa verlies door de versnelling van de ijsplaten. Nieuw inzicht toont de gevoeligheid van deze processen voor toekomstige klimaatverandering. Deze processen zullen echter nog beter moeten worden afgebakend voordat de invloed op het massaverlies van Antarctica kan worden gekwantificeerd. We onderstrepen daarom het belang van een verbeterde representatie van ijsscheuren en ijsplaat verzwakking in numerieke ijskap modellen, en hopen dat de geproduceerde Antarctische scheurkaarten daarbij van waarde zijn. Doen we dat niet, dan onderschatten we waarschijnlijk toekomstige ijsplaat- en massaverlies van Antarctica.

CONTENTS



Chapter 1

Introduction

On the diamond ice, out past the northern ridges, is an empty place, where
the wind laments and no one listens

Mark Lawrence, *The book of the ice*

Antarctica is one of Earth's most awe-inspiring, enigmatic environments that only few get to see in person. It is remote and harsh, as well as dark for months each year, which has made expeditions and scientific research a challenge – in the past and present.

1.1 The Antarctic Ice Sheet

The Antarctic ice sheet is the world's largest mass of ice. It covers an area of roughly 1.3 times the size of Europe, and about all (98%) of the Antarctic continent. The ice sheet holds an equivalent ice mass of ~58 m global mean sea level rise; a lot more than the Greenland Ice Sheet that holds a potential of approximately ~7 m global mean sea level rise. The Antarctic ice sheet has been losing mass in the past decades, contributing approximately 7.4 mm to global mean sea level rise between 1992 and 2020, which is happening at an accelerated rate since the 1990s (Fox-Kemper et al., 2021). Although the Antarctic mass loss is expected to continue in the coming centuries (Pattyn and Morlighem, 2020), how fast and how much Antarctica will contribute to future sea level rise remains uncertain. By 2100, the projected contributions to sea level rise range between 0.03 and 0.34 m, depending on the rate of climate warming (Fox-Kemper et al., 2021).

These projections, however, do not include potential instabilities that can strongly increase Antarctic mass loss on century to multi-century time scales – with an Antarctic contribution to sea level rise up to a meter by 2100, and multi-meter contributions by 2300, under high emission scenarios (Figure 1.2, Fox-Kemper et al., 2021; Edwards et al., 2021; van de Wal et al., 2022). Due to these potential instabilities, Antarctica is currently the largest source of uncertainty in sea level rise projections. Although the likelihood of such extreme scenarios occurring is low, understanding the processes that govern Antarctic mass loss is essential due to the potentially high impacts of high-end sea level rise on coastal communities – both in terms of magnitude and timing of sea level rise.

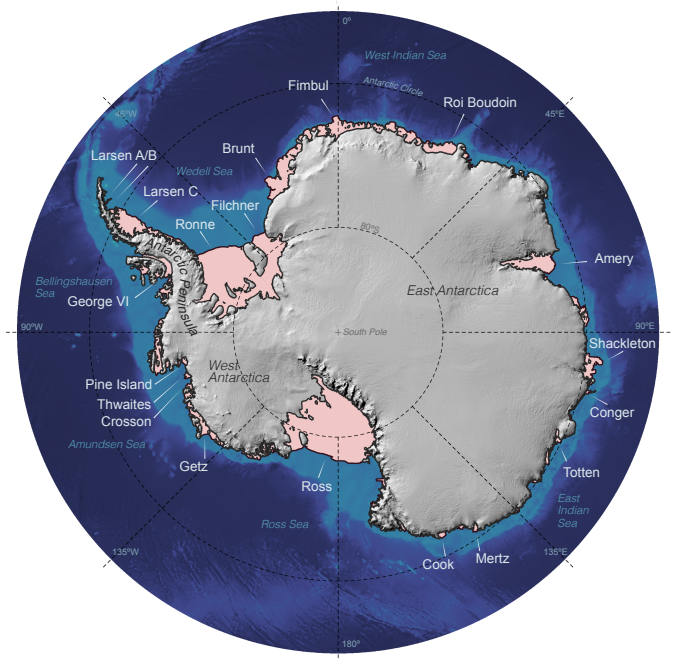


Figure 1.1: **Reference map of Antarctica** showing relevant names and locations for this dissertation. All ice shelves are shown in pink, the grounded ice sheet in in gray (shaded for elevation (Matsuoka et al., 2018)), the ocean bathymetry from Bedmap2 in blue (Fretwell et al., 2013) and the grounding line at their interface (Rignot et al., 2016). As a sense of scale: the Ross ice shelf is approximately the same size as Spain.

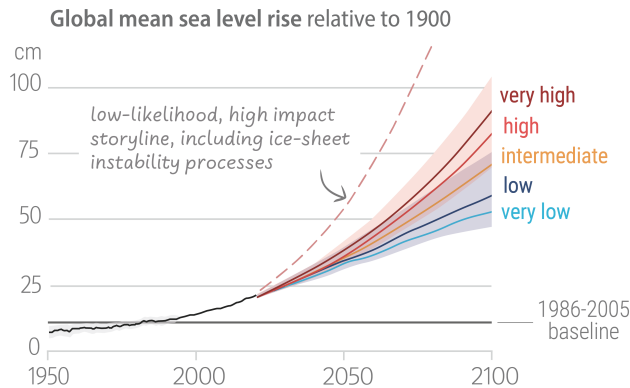


Figure 1.2: **Figure from IPCC AR6 Synthesis Report (Calvin et al., 2023):** Global mean sea level change in centimetres, relative to 1900. Observational (past) changes are shown in black. The future changes to 2100 (coloured lines and shading) are predictions of ice sheet and glacier models; likely ranges are shown for Shared socio-economic pathways (i.e. different climate scenarios) SSP1-2.6 and SSP3-7.0.

1.1.1 Antarctic mass balance

On the ice sheet, snow accumulates at the surface and slowly compacts into firn (Veldhuijsen et al., 2023) and consolidates as ice, adding to the total mass of the ice sheet (Shepherd et al., 2018). The ice sheet loses mass through the melting or sublimation of snow/ice at the surface or base, or the discharge of ice into the ocean at the margin. The high-altitude land ice flows through glaciers toward lower altitudes around the perimeter of the continent, due to gravity (Cuffey and Paterson, 2010). Where the flow of ice meets the sea, the ice starts to float and forms ice shelves: floating extensions of the ice sheet. Ice shelves make up roughly 75% of the perimeter of the Antarctic ice sheet (Figure 1.1), and cover an area comparable in size to the Greenland Ice Sheet (Rignot et al., 2013). The position where the grounded ice starts to float, is termed grounding line.

Ice shelves govern/moderate the mass loss of the ice sheet by providing resistance (buttressing) to the upstream grounded ice: they modulate (and slow down) the flow of grounded ice into the ocean – which contributes to sea level rise. Because of this buttressing effect, ice shelves are considered the ‘safety band’ of Antarctica (Dupont and Alley, 2005; Fürst et al., 2016).

1.2 The importance of ice shelves

Ice shelves are essential in modulating Antarctic mass loss, and one of the most vulnerable parts of the Antarctic Ice Sheet. Compared to the inland ice sheet with an average thickness of more than 2 km, ice shelves are relatively thin (100 m to 1 km) and located at low elevations. They are sensitive to changes in atmospheric and ocean conditions (Davison et al., 2023), as they melt at the surface in response to warm air temperatures as well as at the bottom (basal melt) due to warm ocean temperatures (Liu et al., 2015; Alley et al., 2019). Ice shelves also lose mass at their front (terminus), where ice breaks and forms ice bergs (calving) when fractures extent through the full thickness of the ice.

Although mass changes of ice shelves themselves do not directly contribute to sea level rise, as they are already afloat, it can have an immediate and substantial impact on the upstream, grounded ice sheet. Ice shelf thinning or retreat can reduce the buttressing force provided by the ice shelf (Reese et al., 2017; Gudmundsson et al., 2019; Greene et al., 2022), leading to an increase in the speed of the upstream grounded ice (Rott et al., 2018; Jenkins et al., 2018; Rydt et al., 2021), and an increase in the ice sheet contribution to global sea level rise. Indeed, current Antarctic ice loss is dominated by acceleration, retreat and rapid thinning of major outlet glaciers in West Antarctica, driven by the melting of ice shelves by warm ocean waters (Meredith et al., 2019; Rignot et al., 2013; Davison et al., 2023) (see also Figure 1.3).

The large majority (~87%) of ice shelf area provides buttressing to the ice sheet (Fürst et al., 2016), and a hypothetical, sudden and sustained removal of all ice shelves would lead to a large-scale destabilisation of the ice sheet with an approximated sea level rise of 1–12 meters over 500 years (Sun et al., 2020). Two major processes are commonly associated with the destabilisation of the ice sheet: Marine Ice Sheet Instability (MISI) and Marine Ice Cliff Instability (MICI). MISI is hypothesised to occur for parts of the Antarctic ice

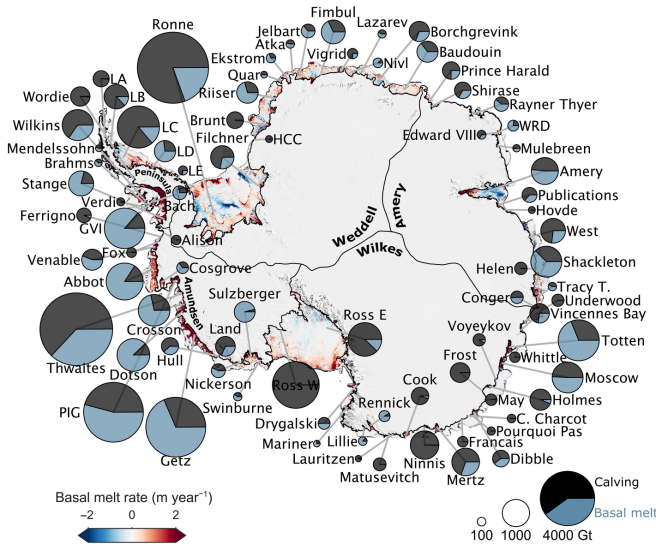


Figure 1.3: **Figure from Davison et al. (2023)**, showing cumulative ice shelf freshwater flux (i.e. mass loss) from 1997 to 2021 overlain on the 2010–2021 average ice shelf basal melt rates and a MODIS image mosaic (Haran et al., 2018). Only ice shelves with a freshwater flux greater than 50 Gt are plotted.

sheet that are situated on a retrograde bed. This process describes how basal melt yields thinner ice shelves, thereby increasing the grounded ice flux and retreating the grounding line. On retrograde slopes this progressively increases the area susceptible to basal melt, as well as enables intrusion of warm, deep ocean waters; both which increase melt and can potentially induce an (irreversible) cycle of grounding line retreat and increased discharge (Weertman, 1974; Bulthuis et al., 2019; Levermann and Feldmann, 2019; Pattyn and Morlighem, 2020). Ice shelves in the West Antarctic Ice Sheet are identified to be especially vulnerable for this type of retreat (Ritz et al., 2015; Scambos et al., 2017; Gardner et al., 2018). Some have worried that this process has been initiated for the Thwaites glaciers, although there is limited observational evidence to support this (Joughin et al., 2014; Scambos et al., 2017; Alley et al., 2021). MICI theorises that the height of ice cliffs is limited by the strength of ice. If an exposed ice cliff, e.g. after the sudden loss of an ice shelf, is sufficiently high it could be unable to support its own weight. This could trigger an instability resulting in an accelerated cycle of cliff collapse and retreat (Bassis and Walker, 2012; Pollard and DeConto, 2016; Crawford et al., 2021). MICI has been described in theory and has been offered as an explanation for fast ice sheet retreat seen in past interglacial periods (Pollard and DeConto, 2016), but there have yet been no known observations of MICI (Bassis et al., 2023).

Both ice sheet destabilising processes depend on the stability and viability of ice shelves. However, despite the importance of ice shelves for stabilising large portions of the Antarctic Ice Sheet, and much research into documenting changes, the processes governing ice shelf thinning and retreat remain a major uncertainty in future sea level rise projections

(Fox-Kemper et al., 2021; Davison et al., 2023; Bassis et al., 2023). Understanding the potential instability of ice shelves is therefore crucial in order to improve predictions of the timing and magnitude of Antarctica's contribution to sea level rise.

1.2.1 Ice shelf instability

Stable ice shelves advance and retreat in recurring cycles (Fricker et al., 2002; Lazzara et al., 2008). Many ice shelves exhibited a stable cycle of calving front advance and retreat in the past decades to centuries (Alley et al., 2023; Andreasen et al., 2023; Davison et al., 2023), but there is a growing catalog of evidence that both long-term and short-term environmental forcings are increasingly pushing ice shelves outside of their stable regimes (Bassis et al., 2023; Millan et al., 2023; Wille et al., 2022). Ice shelf instability is affected by multiple processes that weaken the ice shelf and could lead to rapid retreat or even collapse (the sudden and massive break up) of an ice shelf. The processes responsible for ice shelf retreat are all related to the role of failure, fracture, and calving of ice shelves. While most fracture initiation and calving is controlled by internal glaciological stress within the ice, ice shelves are also susceptible to atmospheric and oceanic conditions, and other external forces exerted on the ice shelves.

Basal melt, controlled by ocean temperatures, leads to thinning of ice shelves and so reduces their buttressing ability (Paolo et al., 2015; Adusumilli et al., 2020; Davison et al., 2023), which is especially pronounced if thinning result in the unpinning of the ice shelf from bathymetric highs (pinning points) (Tinto and Bell, 2011; Berger et al., 2016; Wild et al., 2022; Benn et al., 2022; Zinck et al., 2023). Basal melt also produces crevasses at the bottom of the ice shelf that eventually lead to calving (Liu et al., 2015; Alley et al., 2019). Basal melt has been occurring most strongly in the Bellingshausen and Amundsen Sea due to the intrusion of warm Circumpolar Deep Water, and has been the main cause for increased discharge and mass loss of the Antarctic Ice Sheet in the past decades (Jenkins et al., 2018; Holland et al., 2019).

Changes in atmospheric temperatures or weather (wind) patterns can increase surface melt and meltwater ponding (Husman et al., 2024). If surface melt lakes drain through fractures in the ice, ice shelf flexure occurs which can lead to rapid fragmentation (Mobasher et al., 2016; Banwell et al., 2019). This hydrofracturing process was the driving factor of the collapse of the Larsen B Ice Shelf in 2002 and Wilkins Ice Shelf in 2008 (Rack and Rott, 2004; Scambos et al., 2009). About 60% of ice shelves (by area) that provide significant buttressing are thought to be vulnerable to hydrofracture if inundated with water (Lai et al., 2020).

Ice shelf flexure is also induced by ocean tides and sea surface slopes (swell), leading to fracturing and calving. The presence of sea ice and ice mélange can provide stability to an ice shelf by dampening ocean swell and waves (Lipovsky, 2018; Massom et al., 2018). The removal of sea ice or mélange (e.g. by changing wind patterns) can lead to the disintegration of (already weakened) ice shelves (Massom et al., 2018; Larour et al., 2021; Christie et al., 2022). This has been considered key for the rapid retreat of the Voyeykov ice shelf in East Antarctica in 2007 (Arthur et al., 2021) as well as the for the fast retreat and immediate speed-up of the Crane, Hektoría and Green glaciers on the Antarctic Peninsula in 2022 (Ochwat et al., 2023).

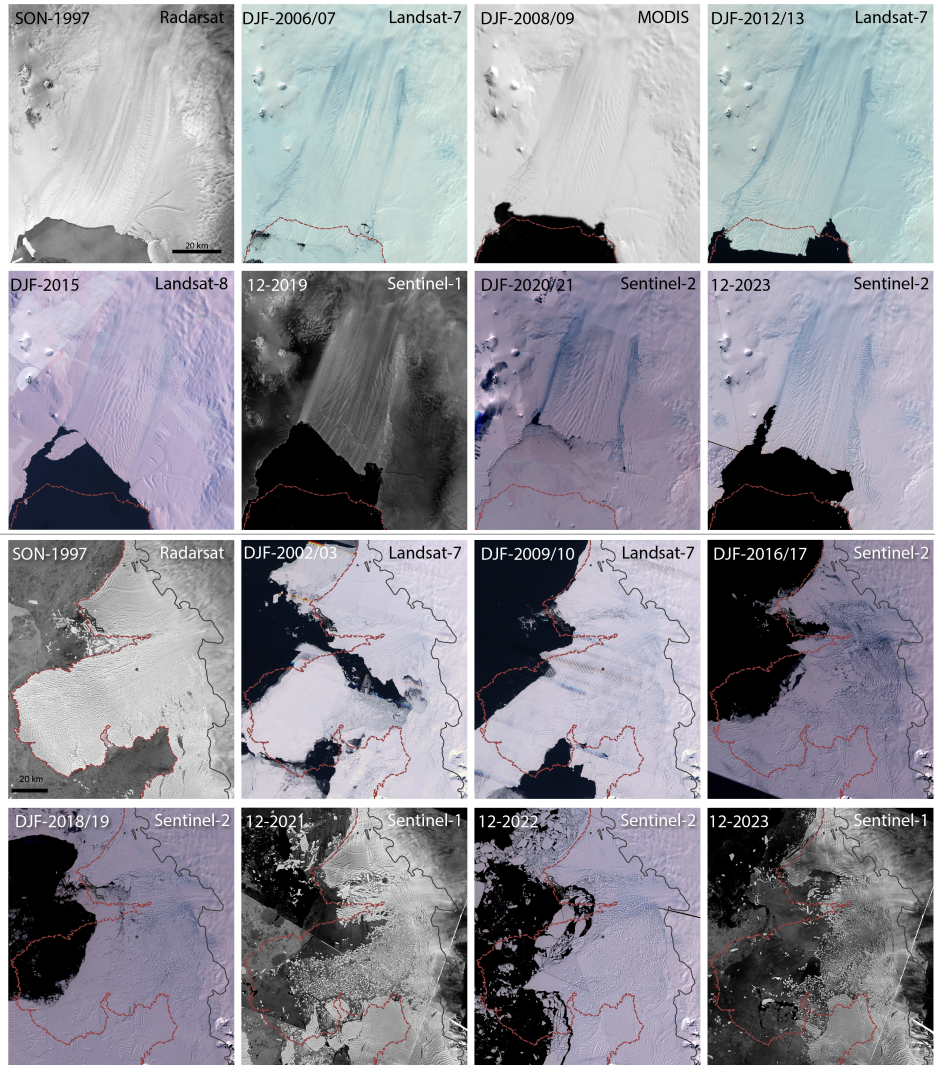


Figure 1.4: Examples of satellite imagery for the fast retreat of Pine Island and Thwaites Ice Shelves. Timeseries of observations of Pine Island Ice Shelf (top) and Thwaites Ice Shelf (bottom), obtained from satellite sources of varying spatial resolution: RAMP Radarsat (100 m), Landsat 7/8 (30 m), MODIS (250 m), Sentinel-1 IW (10 m) and Sentinel-2 (30 m). Observations are combined into a single image by either constructing a median composite of multiple images in austral summer (December, January, February; DJF), autumn (September, October, November; SON), or an image mosaic of the most recent images (December of selected year). The calving front location of 1997 is plotted on the other panels.

Furthermore, the development of fractures and heavily damaged areas on an ice shelf weaken the structural integrity of the ice shelf themselves. Fractures and damage effectively soften the ice (Albrecht and Levermann, 2014), reducing its load-bearing capacity and thereby the ability of the ice shelf to provide buttressing (Sun et al., 2017). As the buttressing effect of an ice shelf decreases, the ice flow speeds up, increasing internal stresses and promoting additional damage development; initiating a positive feedback (Lhermitte et al., 2020; Surawy-Stepney et al., 2023a).

In short, the development of fractures and damage areas on an ice shelf are (first) signs of its weakening, and can affect both the ice flow and calving rate (Rydt et al., 2019). Despite their importance for ice shelf retreat, to what extent damage is present at Antarctic ice shelves is not well quantified. Neither do we have assessments of how damage areas have been changing over time. Therefore we still have limited understanding of how damage relates to ice shelf weakening and observed retreat. Overall, it remains one of the most poorly understood processes in marine ice sheet dynamics (Albrecht and Levermann, 2012; Pattyn et al., 2017; Lhermitte et al., 2020; Fox-Kemper et al., 2021).

1.3 Damage on ice shelves

Crevasses and fractures are visible manifestations of the stresses within glacier ice, initiated when local stresses exceed the strength of the ice (Veen, 1998b). Stresses in the ice are often concentrated in specific regions of the ice flow, such as steep elevation drops (i.e. ice falls), areas of high lateral drag, or imposed by pinning points under an ice shelf (Berger et al., 2016; Colgan et al., 2016). Fractures that initiate in these regions are advected downstream with the ice, further evolving (or healing) depending on the downstream stress and strain fields (Vaughan, 1993).

1.3.1 Damage types and traits

‘Damage’ is an umbrella term used in this dissertation to encompass the various shapes and sizes of fracture features, such as cracks, crevasses, fractures and rifts. In literature, ‘crevasses’ or ‘fractures’ are sometimes used interchangeably to indicate open fractures in the surface of the ice. Colgan et al. (2016) define fractures as smaller openings than crevasses. The modelling community more strictly distinguishes *fracture* mechanics as a method to determine *crevasse* depth or opening (e.g., Veen, 1998b,a; Weertman, 1980; Levermann et al., 2012; Benn and Åström, 2018), versus *damage* mechanics that represent degradation of the bulk material properties of the ice (e.g., Murakami et al., 1988; Pralong et al., 2003; Krug et al., 2014; Mobasher et al., 2016). This distinction is less strict in observational assessments that talk about both crevasses (e.g., Colgan et al., 2011; Gong et al., 2018; Chudley et al., 2021), fractures (e.g., Lai et al., 2020; Pang et al., 2023; Surawy-Stepney et al., 2023b) and damage (e.g., Libert et al., 2022; Surawy-Stepney et al., 2023a).

Observed crevasses range in width from millimetre-scale cracks to several (tens of) meters (Colgan et al., 2016); their horizontal length can be tens to a (few) hundred meters. Air-filled crevasses are observed up to 45 m deep in Antarctica. When filled with water,

the added pressure can lead to drastic increases of crevasse depth, called hydrofracturing. This can occur on short time scales and can trigger explosive ice shelf disintegration when occurring on an extensive area of the ice shelf. Hydrofracturing has been recognised as the driving process behind the collapse of Larsen B ice shelf in 2002, which occurred on the scale of a few weeks (Rack and Rott, 2004; Banwell et al., 2013).

Rifts are crevasses that have propagated through the entire thickness of an ice shelf. Rifts can become very large openings within the ice, with widths of hundreds of meters (e.g. ~ 270 m observed at Amery Ice Shelf (Fricker et al., 2005)) and lengths of many (hundreds of) kilometers (Joughin and MacAyeal, 2005). Rifts can be filled with ice mélange: a mixture of snow, sea ice and ice bergs. Ice mélange is associated with rift propagation as well as changes in ocean circulation (Poinelli et al., 2023). When one or more rifts propagate horizontally through the ice shelf they eventually calve large tabular ice bergs. These rifts propagate often on time scales of decades or longer (Rydt et al., 2019; Joughin and MacAyeal, 2005; Lazzara et al., 2008), but also instantaneously remove decades of accumulated ice mass once calving occurs. For example, in July 2017, iceberg A-68 calved an approximate 5800 km^2 from the Larsen C ice shelf (Larour et al., 2021), an area twice as large as Luxembourg; in May 2021, $170 \text{ km} \times 25 \text{ km}$ (4320 km^2) A-76 ice berg calved from Filchner-Ronne Ice Shelf (Andreasen et al., 2023), an area roughly as large as the island Mallorca, Spain.

1.3.2 Modelling fractures, damage and calving

Fracture mechanics

Fracture mechanics considers the failure and fracturing of ice under loading and is used to estimate crevasse depth. The orientation of loading with respect to crevasse orientation is important and used to distinguish three modes of failure: mode I (tensile or opening), mode II (sliding or in-plane shear) and mode III (tearing or out-of-plane shear) (Colgan et al., 2016). Mode I has historically received the most attention due to its clear relationship to rifting and crevassing (Benn and Åström, 2018; Bassis et al., 2023). However, mixed mode failure of Mode I + II has been associated with ice cliff failure (Bassis et al., 2023), and mixed mode failure of mode I + III has been deemed important to correctly attribute observed crevasse orientation with respect to the orientation of principal tensile stress or by rotation during advection (Veen, 1998b; Colgan et al., 2016).

Crevasse depths is commonly estimated by the Nye zero stress model, which assumes a penetration depth until the horizontal stress vanishes (Nye and Wills, 1957; Jezek, 1984), or by linear elastic fracture mechanics (LEFM), which relate the penetration depth to the point where stress singularity is equal to the material fracture toughness (Smith, 1976; Weertman, 1980). LEFM modelled crevasses can penetrate deeper and are generally assumed to apply to isolated crevasses, whereas the Nye zero stress model is assumed to apply to closely spaced crevasses (Clayton et al., 2022).

Damage mechanics

Damage mechanics is used as alternative to fracture mechanics. In continuum damage models, damage represents the degradation of the bulk material properties – affecting the load bearing capacity of the ice. It represents the collective weakening of ice due

to a distribution of cracks and localised failure processes in the ice (Pralong et al., 2003; Pralong and Funk, 2005). Creep-based damage models have been successful in reproducing surface and bottom crevasses predicted by LEFM and Nye zero models in idealised scenarios (Duddu et al., 2020) and have shown promise in simulating the propagation of rifts in idealised and real ice shelves (Huth et al., 2021, 2023).

Alternatively, a pseudo-damage parameter can be estimated from the ratio of crevasse depth to ice thickness, with crevasse depth as initiated by the Nye zero stress model, and then considering a positive feedback between ice rheology and crevasse damage (Sun et al., 2017) or the crevasse stability depending on necking and melt presence (Bassis and Ma, 2015). These approaches depend on strain rates rather than stresses (Albrecht and Levermann, 2012) and provide a connection between damage evolution and environmental forcing capable of explaining contemporary observations on ice tongues and ice shelves (Kachuck et al., 2022).

Calving

Calving occurs when fractures or rifts separate an ice berg from the glacier or ice shelf. Crevasse depth and damage models do not explicitly predict single fractures or calving events but rather an abstraction of fields of crevasses and the macroscopic effect these have on calving. More simplified approaches to estimate the calving flux of ice shelves are formulated, such as fixed-front calving laws, minimum ice thickness calving, strain rate-based calving laws (eigencalving) (Alley et al., 2008; Hindmarsh, 2012; Levermann et al., 2012) or stress-based calving laws (von Mises calving) (Morlighem et al., 2016; Wilner et al., 2023). Both the fixed-front and minimum ice thickness calving laws are simplified approximations and easy to implement in numerical models. The eigencalving and von Mises calving laws can be tuned to reproduce the calving front behaviours of many glaciers and ice shelves (Albrecht and Levermann, 2012, 2014; Morlighem et al., 2016). However, for both approaches the tuning parameter varies significantly between different ice shelves and glaciers, and thus it is difficult to judge how reliably these laws can be extrapolated to new conditions (Bassis et al., 2023; Wilner et al., 2023). Lastly, discrete element models (DEMs) can model and resolve the calving and detachment of individual ice bergs. These models are used to study the brittle fracture of ice across a range of spatial and temporal scales and the mechanical impact of mélange on the calving front, but do not include the long-term viscous creep of the ice.

1.3.3 Challenges with damage modelling

The development of increasingly complex calving laws has outpaced law validation, leading to significant uncertainty in the applicability of calving laws at the ice sheet scale (Wilner et al., 2023). There is limited evidence that current generation of models can predict ice shelf collapse or disintegration (Kachuck et al., 2022; Bassis et al., 2023). Extensive calibration or evaluation of modelled crevasses or damage has been challenging due to the limited availability of large-scale observations of damage, and the few studies that did show large discrepancies (Enderlin and Bartholomäus, 2020; Gerli et al., 2023b). As a result of these model limitations, we cannot yet quantify the impact of damage on ice shelf stability and mass loss outside of idealised scenarios, and have so far been unable to provide projections for future weakening states of ice shelves.

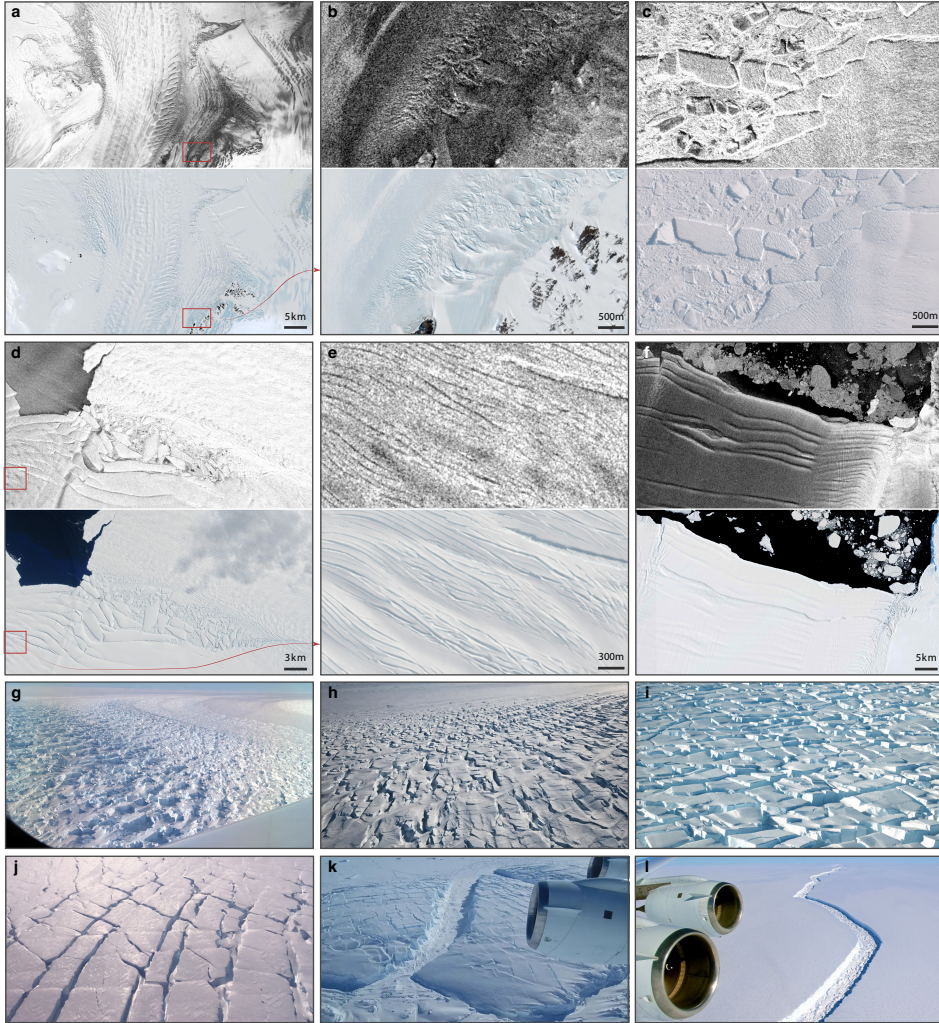


Figure 1.5: **Damage examples.** Panels (a-f): SAR (top) and Optical (bottom) observations of the same damage type, observed within 5 days of each other. Data obtained from the Copernicus Browser. Panels (g-l): aerial photos of damage features in Antarctica, not at the same locations as upper panels. (g) Denman glacier, NASA/John Sonntag; (h) Pine Island, Ian Joughin; (i) Pine Island, US National Science Foundation; (j) Thwaites, Britney Schmidt; (k) Thwaites, NASA/Jim Yungel; (l) Larsen C, NASA/Stuart Rankin (hyperlinks to image sources included in digital version of this document).

1.4 Damage observed with remote sensing data

Satellite observations provide an extensive record of data that can be used to map fractures and damage areas across Antarctic ice shelves and the ice sheet. Damage is visible in multi-spectral imagery and Synthetic Aperture Radar (SAR) images (i.e. crevasse extent; horizontal properties), as well as in altimeter data (i.e. crevasse depth; vertical properties).

1.4.1 Data types

Multi-spectral (optical) imagery

Optical imagery provides passive observations of the earth's surface. The sensor measures the amount of sunlight reflected by the surface (i.e. taking a picture). The visibility of desired observable features therefore depend on the illumination by the sun. This has multiple implications: (a) observations can only be obtained during day-time, which means there are no observations throughout polar night for the Antarctic ice sheet; (b) features can be obscured by other objects. The largest limitation this poses is due to the presence of cloud cover, or snow covering surface fractures (creating snow-bridged crevasses); (c) The sun angle determines the strength and direction of shadows, influencing the visibility of crevasses in the images. The sometimes rough surface of the Antarctic ice can make it difficult to distinguish the rough snow surface from fractures. In optical imagery, fractures look like dark lines, as the deep crevasses are in shadow with respect to the white icy surroundings.

SAR imagery

SAR imagery is obtained using an active sensor, that sends and receives a microwave signal. An important attribute of SAR imagery is that the signal is independent of day or night-time, and penetrates cloud cover. This enables observations throughout the year regardless of atmospheric conditions. The signal furthermore penetrates the first few meters of snow, and so can detect crevasses obscured by a (shallow) snow bridge. The radar signal is scattered at the surface through (multiple) interaction(s) with surface features, varying the amount of energy that is received back at the sensor. However, due to (random) interference of multiple scattering events, the retrieved image from the SAR sensor contains more noise, called speckle, than images from optical sensors. These high noise ratios can make it difficult to resolve small scale features. Figure 1.5 provides examples of the same damage features in both optical and SAR imagery to show this difference. Smooth, flat surfaces reflect fewer of the incoming signal, and are therefore less bright in the image than rough surfaces. Fractures, characterised by vertical walls that reflect much of the signal back to the sensor, are generally bright linear features in SAR imagery. The look-angle of the sensor influences these signal returns as well.

Altimetry and DEMs

Altimetry remote sensing actively sends and receives a laser or radar signal, operating with short wavelengths (near-infra red or visible range). The lasers measure very precisely along their ground track, and can therefore be used to study crevasse depth and

with (Fricker et al., 2005; Liu et al., 2014; Wang et al., 2021). By combining multiple tracks, 3-D analysis of crevasse morphology can be achieved, although these have been limited to a single glacier or ice shelf (Li et al., 2021; Herzfeld et al., 2021). The use of digital elevation models (DEM; a product obtained from e.g. altimetry (Bamber et al., 2009) or photogrammetry (Porter et al., 2018)), that provide a 2-D field of elevation rather than along-track narrow lines, can be a useful alternative for larger scale crevasse depth assessments, though at the cost of temporal resolution (Chudley et al., 2021).

1.4.2 Challenges with detecting damage from observations

Extracting the horizontal properties of fractures and damage from satellite imagery is a complicated task due to three major challenges. Firstly, the same fracture may appear different in different satellite images due to the complex and rough snow surface of the Antarctic, cloud and shadow effects in optical imagery, or speckle and noise in SAR imagery. Some examples of the same damage pattern in both optical and SAR images are shown in Figure 1.5. Secondly, there are morphological similarities between full-thickness rifts, surface expressions of basal fractures, and flow lines (Luckman et al., 2012; McGrath et al., 2012a) that are difficult to distinguish from fractures (Colgan et al., 2016; Ely and Clark, 2016). Thirdly, the spatial resolution of the available data determines the size and scale of the features that can be resolved. For rifts of multiple kilometers, this is a somewhat trivial issue, but for small-scale crevasses or closely spaced crevasse fields, an observational resolution of 10 m (Landsat 8 panchromatic band or Sentinel-1 Interferometric Wide mode) versus 250 m (MODIS) is a fundamental difference. Figure 1.5 also includes some aerial photos to illustrate the differences in scale between observable damage features.

As a result of these challenges, for practical purposes, fractures were often mapped manually in the past. Most studies in practice either perform an extensive manual mapping of fine resolution features (e.g. Scambos et al., 2009; Kaluziński et al., 2019), or focus on large-scale rifts in data with coarser spatial resolution that cannot capture small scale features (e.g., Glasser and Scambos, 2008; Hulbe et al., 2010; Lai et al., 2020). Other approaches to detect damage have been developed based on adapted image processing techniques. For example by using edge detection techniques on optical imagery (e.g., Colgan et al., 2011; Bhardwaj et al., 2016; Hui et al., 2016; Gong et al., 2018; Vries et al., 2023), edge detection techniques on Interferometric SAR data (e.g., Rignot, 1998; Hogg and Gudmundsson, 2017; Libert et al., 2022) or by utilising high resolution elevation profiles (e.g., Enderlin and Bartholomäus, 2020; Chudley et al., 2021). These approaches, however, often required specific preprocessing and postprocessing and/or are not easily applied on a large spatiotemporal scale; a limit incurred due to (a combination of) computational costs, the limited transferability of these methods to different regions, or the unavailability of the used data over longer time periods.

Machine Learning for damage detection

With the advent of machine learning in the past decade(s), efficient methods suitable for applications on large amounts of (satellite) data – and so Antarctic wide scale applications – have become possible. This has led to the first fracture map of Antarctica in 2020, developed by Lai et al. (2020), which was produced using a Convolutional Neural Network

(CNN) trained on the MODIS mosaic of Antarctica (MOA). More studies have used similar approaches, such as a CNN developed by Pang et al. (2023) applied to three MOA's, and CNN's developed by Zhao et al. (2022); Surawy-Stepney et al. (2023b) applicable to Sentinel-1 SAR data.

However, many automated methods to detect fractures also detect a great deal of non-fracture features, such as flow lines or suture lines, that cannot be distinguished and excluded. Furthermore, CNN hyperparameters require extensive and repeated tuning, which is still dependent on manual methods. The training samples are also manually labeled and influence the training result. This comes at the cost of efficiency, leading to hysteresis in monitoring the instability of large ice shelves. Efforts are made to account for these issues, such as including external datasets to filter fractures from non-fractures (Lv et al., 2022), or developing more detailed machine learning approaches that can differentiate between different types of fracture features (Surawy-Stepney et al., 2023b).

Lastly, a remaining limit of current existing automated fracture detection approaches is that these have been calibrated to a dataset with a specific spatial resolution and from a specific (satellite) data source. These methods are not transferable to other data sources of varying spatial resolution, and so pose limitations on the temporal coverage of their applications, as they are tied to a single satellite mission (such as Rignot, 1998; Libert et al., 2022; Surawy-Stepney et al., 2023b) or to constructed mosaics (such as Lai et al., 2020; Pang et al., 2023).

1.5 Research Objectives

To recap, the short-term collapse or long-term weakening of ice shelves can result in drastic increases of ice discharge and Antarctic mass loss, which is a major uncertainty in sea level rise predictions. Damaged areas on ice shelves are first indicators of its weakening, but despite their significance for future ice shelf stability, damage processes remain poorly understood. There are few quantifications of the damage extent across all Antarctic ice shelves, and even less on how this has changed over time, partially due to challenges in developing robust detection methods. As a result, extensive calibration or evaluation of modelled crevasses and damaged areas has been difficult. Therefore, to improve our understanding of damage impacts on ice shelf weakening and retreat, more insights from the observational perspective on damage and damage changes are a first essential step. And, in order to get these insights, a suitable method to detect damage from observations is required.

The main goal of this thesis is **“To expand our knowledge of the abundance of damage and its development on Antarctic ice shelves, and to improve our understanding of its impact on ice shelf weakening and retreat”**. This will be investigated from an observational perspective. The following research questions are formulated to support the achievement of this goal:

1. **How can an effective and robust method be devised to detect damage on Antarctic ice shelves from multi-source satellite imagery?**
2. **What is the current extent of damage across Antarctic ice shelves, and how has this damage evolved over the past decades?**
3. **To what extent is detected damage correlated to ice shelf retreat?**
4. **How is detected damage linked with mechanical weakening of ice shelves?**
5. **What is the importance of damage on future ice shelf weakening and retreat?**

1.6 In this thesis

Chapter 2: Damage Detection on Antarctic Ice Shelves using the Normalised Radon Transform

This chapter relates to research question (1) and aims to develop a method that can provide large spatiotemporal assessments of damage on Antarctic ice shelves.

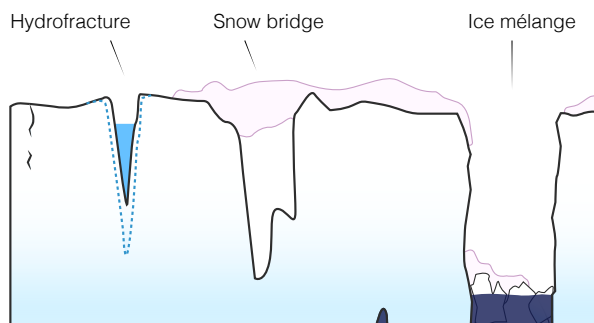
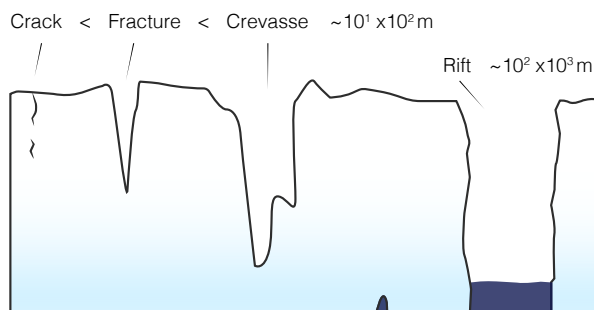
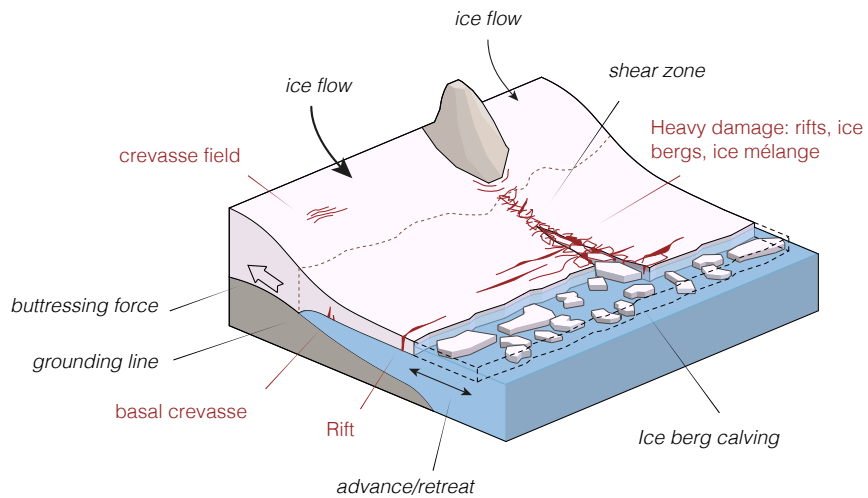
Chapter 3: Assessment of Antarctic damage change over two decades

By utilising the developed method in Chapter 2, an extensive assessment is made of detected damage on Antarctic ice shelves, addressing research question (2). The assessments are used to infer insights for question (3) on the correlation between damage and ice shelf retreat.

Chapter 4: Antarctic ice shelves vulnerable to damage in future climate warming

This chapter relates to research question (4-5). Further expanding on the outcome from Chapter 2 and 3, the assessments of damage are used to investigate their link to ice shelf weakening. The found relationship is used to gain insights in future scenarios.

Chapter 5 summarizes and discusses the individual chapters, along with recommendations and implications for future research.



SOME ICE SHELF TERMINOLOGY



Chapter 2

Damage Detection on Antarctic Ice Shelves with the Normalised Radon Transform

This chapter is published as: Izeboud, M. and Lhermitte, S., 2023. Damage detection on Antarctic ice shelves using the normalised radon transform. *Remote Sensing of Environment*, 284, 113359, <https://doi.org/10.1016/j.rse.2022.113359>

Studying the impacts of damage on ice shelf stability starts with the ability to detect and assess the amount of damage on the large Antarctic domain. Most prior existing methods have spatial constraints that limit their applicability on different or large regions. Efforts have been made to develop methods that can be applied on Antarctic wide scales, although progress in this regard has been very recent (2020 and later). These emerging methods are, so far, tuned to a single data source, limiting their applicability on long time scales that extend beyond a single satellite mission. The first necessary step is therefore to develop a generalised method that can be applied to all Antarctic ice shelves, for multiple years. This chapter aims to develop a method that can be applied to both Optical and SAR imagery that will support both a wide spatial and temporal application. In this chapter we consider the research question: ‘How can an effective and robust method be devised to detect damage on Antarctic ice shelves from multi-source satellite imagery?’

In Section 2.2 we introduce the concept of the Normalised Radon Transform as a Damage Detection method, NeRD. In Section 2.3 and 2.4 we describe the study area and specifics on how we develop and test the proposed NeRD method. In Section 2.5 we show the sensitivity of NeRD to different sensor and image resolutions, demonstrate its application to ice shelves in the Amundsen Sea Embayment and evaluate the result. We conclude by showing the potential of NeRD to assess damage evolution (2.5.4), and discuss its uncertainties and potential in Section 2.6 and 2.7.

2.1 Introduction

Antarctic ice shelves modulate grounded ice flow through buttressing. Their weakening or disintegration is crucial for the timing and magnitude of grounded ice loss and onset of instabilities (Sun et al., 2017; Benn and Åström, 2018; Vieli et al., 2007; Albrecht and Levermann, 2012), and thereby for the sea level contributions from Antarctica (Fox-Kemper et al., 2021). The development of damage areas in the shear zones of an ice shelf are first signs of structural weakening. Damage areas typically consist of highly crevassed areas, rifts and open fractures containing dense ice mélange (Lhermitte et al., 2020; Borstad et al., 2012). The development of damage in the shear zones of an ice shelf can result in further speedup, shearing and weakening, hence promoting additional damage development. This feedback potentially preconditions ice shelves for disintegration and enhanced grounding line retreat (Lhermitte et al., 2020). For example, damage has been considered key for the ice shelf collapse of Larsen B and the retreat of Pine Island Glacier and Thwaites Glacier (Glasser and Scambos, 2008; Borstad et al., 2012). Although this damage feedback has been identified as key to future ice shelf stability, it is one of the least understood processes in marine ice sheet dynamics.

Remote sensing data provides the possibility to detect fractures and damage areas across Antarctic ice shelves and the ice sheet. Where laser altimetry is used to map vertical properties, quantifying the continuous distribution of fractures in the horizontal dimension remains unsolved (Wang et al., 2021; Herzfeld et al., 2021; Li et al., 2021). Assessing horizontal properties of fractures and damage from satellite imagery can be a complicated task due to three major challenges. Firstly, there are morphological similarities between full-thickness rifts, surface expressions of basal fractures, and flow lines (Luckman et al., 2012; McGrath et al., 2012a) that are difficult to distinguish (Colgan et al., 2016; Ely and Clark, 2016). As a result, for practical purposes, fractures are often mapped manually. Secondly, the spatial resolution of available data and the research focus of the individual studies determines the size and scale of the features that are resolved. Damage comes in all shapes and sizes: from small surface crevasses in densely crevassed fields to full-thickness rifts near the ice front of multiple kilometers long, to the complex and irregularly shaped ice mélange in damaged shear zones. Thirdly, similar damage may appear different in different images due to changing illumination or viewing conditions, the complex surface of the Antarctic, snow or cloud cover, or variable signal-to-noise levels (speckle) in SAR imagery (Colgan et al., 2016). These challenges imply that most studies in practice either perform an extensive manual mapping of fine resolution features, such as Scambos et al. (2009); Kaluzienski et al. (2019) or focus on large-scale linear rifts in data with coarser spatial resolution (e.g., MODIS) that cannot capture small scale features (Glasser and Scambos, 2008; Lai et al., 2020).

Previous studies such as Bhardwaj et al. (2016) and Colgan et al. (2011) have developed approaches to perform fine-resolution crevasse or crevasse field detection on optical data, but these approaches are not easily applied on a large spatiotemporal scale. Bhardwaj et al. (2016) used band ratios from pan-sharpened Landsat 8 optical and thermal bands to create a fine resolution (15 m) but small spatial crevasse map, covering 4 km². Colgan et al. (2011) manually digitised crevasse fields after convolving a high-quality panchromatic aerial photograph (2 m resolution) with a Roberts cross-edge detector. Both studies

were limited to two dates on a single glacier. Alternatively, a first Antarctic-wide fracture map has been developed by Lai et al. (2020) using a deep Convolutional Neural Network (CNN). This CNN, however, was trained on manually labelled large-scale rifts and applied on a relatively coarse resolution MODIS mosaic (125 m), resulting in the loss of fine spatial detail of the damage features.

The Radon transform was proposed as an alternative, more robust approach to detect crevasses (Gong et al., 2018). The Radon transform can detect both linear fractures and more complex patterns of heavily damaged areas, where other edge detection methods fail or require extensive processing (Bhardwaj et al., 2016; Colgan et al., 2011; Roberts et al., 2013; Gong et al., 2018). The Radon transform was previously applied to both SAR and optical satellite data for flow line detection (Roberts et al., 2013) and crevasse detection (Gong et al., 2018). This dual application moreover highlights the potential to combine different data sources in a new detection approach, overcoming limitations from each individual source. Furthermore, the Radon transform can detect both feature orientation and feature signal strength, allowing insight in crevasse rotation and advection over time. One drawback of the Radon transform as damage detector developed by Gong et al. (2018), however, is the lack of consistency to quantify damage. The current method depends on the intensity of the (gray-scale) image pixels which often varies in space and time and even depends on the cut-out windows of the Radon transform. Different illumination conditions, look-angles, and sensors affect the image intensity, resulting in different crevasse signal values. These issues limit the application of the Radon transform as a method for generalised, automated damage assessments.

In this study we propose a novel method that builds upon the Radon transform method of Gong et al. (2018) to allow a generalised damage assessment. To this end, we have developed the NormalisEd Radon transform Damage detection (NeRD) method (Section 2.2) which can be applied directly to multiple satellite data sources across spatial or temporal domains, without requiring additional pre- or post-processing. This includes optical and SAR data from Sentinel-1, Sentinel-2 and Landsat 7/8. We apply NeRD to ice shelves in the Amundsen Sea Embayment (Section 2.3), and test the method for different parameter settings related to spatial resolution and data source (Section 2.4). The results are validated by comparing with a manually labeled damage map of multi-scale damage features, and with the existing CNN fracture map of Lai et al. (2020). In Section 2.5 we display the damage detection product, showing constructed damage maps for the study area including damage signal and damage orientation, the performance and evaluation of the NeRD method, and finally its application on a time series of the Pine Island Ice Shelf.

2.2 NormalisEd Radon transform Damage detection (NeRD)

The NormalisEd Radon transform Damage (NeRD) detection method builds upon the method of Gong et al. (2018) and Altena (2018), which were initially based upon the work of Roberts et al. (2013). NeRD is intended to be a robust and generalised, one-size-fits-all method that can be applied across image sources and results in a consistent, quantitative damage detection product.

Roberts et al. (2013) used the Radon transform to detect flow lines and their orientations on the Amery ice shelf using RADARSAT data, whereas Gong et al. (2018) used the Radon transform to detect crevasses and their orientations on the Austfonna ice cap (Svalbard) from Landsat 8 data. Both used a similar approach, consisting of: (i) pre-process the image with a Laplacian filter to enhance edge contrast and remove noise, (ii) extract cut-out windows from the image, (iii) apply the Radon transform to the cut-out windows, (iv) extract dominant feature signal strength and dominant feature orientation for every window, and finally, (v) post-processing. However, there are two issues in this approach that hinder a quantitative and consistent interpretation of the feature signals.

The first issue stems from Radon transform algorithm itself, and how it extracts the feature signal. The Radon transform is a line-detection algorithm that projects the image (or cut-out window) intensity along a radial line oriented at a specific angle (Oppenheim and Willsky, 1996). See for a schematic example Figure 2.1, where the line integral is displayed for two example projection angles. The standard deviation or variance of this line-integral indicates the level of contrast within the window at each angle and the maximum standard deviation across all angles is used to extract a feature signal and orientation (Roberts et al., 2013; Altena, 2018).

The drawback of the classical Radon transform is that the feature signal retrieved from the Radon transform line-integral is dependent on the pixels in the cut-out window. This manifests in three problems. First, the feature signal value depends on the number of pixels in each cut-out window. This results in higher signal values for larger windows. Second, the signal value is dependent on the average pixel intensity values, yielding higher signal values for brighter images. Third, the Radon transform returns false signals for uniform data. Because of these problems, the results of the classical Radon transform are inconsistent between different images or cut-out windows as the signal value of the Radon transform is relative to each processing window instead of a global value across the image. This limits a generalised implementation of damage detection.

In the NeRD method we propose to solve these three problems by normalisation of the Radon transform. Normalisation makes the Radon signal value independent of the number of pixels in the window, and unbiased to shifts in pixel intensity values. The false signals are then removed as a result, solving all three problems. See for example Figure 2.1a: the Radon transform without normalisation shows a varying line integral over the two projection axis for a uniform window. This means that the variance is non-null and yields a false signal. The normalised Radon transform, however, is a flat line, which (correctly) returns no signal. With NeRD, the damage signal value depends only on the contrast of a linear feature in the window, rather than on the size of the feature or window. Therefore, NeRD yields a consistent value that can be interpreted across all windows and between different images. Although the signal value is independent of the number of pixels in the window, it should be noted that the window size still determines which features can be detected. If the window is too large/small to reveal the features to be detected, it will not work and NeRD is consequently not completely independent of the window size. A proof-of-concept of implementing the normalisation step is provided in Section 2.2.3. Here further detail and examples are provided to illustrate how the three problems are solved.

The second issue of the Radon transform as applied by Roberts et al. (2013) and Gong et al. (2018) is introduced in the pre-processing of the image using an edge-enhancement Laplacian filter. This filter re-scales the gray-scale input image into binary black and white values and, consequently, maximises all edge-like surface features and removes noise. This potentially includes maximising surface roughness features such as snow dunes or sastrugi that should not be detected as damage. Additionally, the use of the Laplacian filter reduces all existing contrast gradations into binary 0/1 values. Consequently, the Radon transform is no longer able to distinguish between features that display different contrast strengths and provide a quantitative measure of strength of the damage signal. This quantitative measure can however be potentially useful to discriminate between damage features as we expect that strong and prominent contrasts correspond to large damage features, such as a rifts, while low contrast features presumably correspond to smaller scale damage features, such as surface crevasses. Similarly, an opening crevasse will show changes in contrast over time. As a solution to this issue we remove the use of a Laplacian filter as a pre-processing step and replace it with a post-processing step that removes noise from the output by setting a minimum signal threshold. This allows NeRD to detect continuous, quantitative damage signals without contaminating the product with noise.

In summary, the presented NeRD method consists of the following steps: (i) create cut-out windows from the image, (ii) apply the Normalised Radon transform to these windows, (iii) extract dominant feature signal strength and orientation for every window, (iv) quantify the damage signal value by removing noise from the signal and (v) post-processing. In the NeRD post-processing step we remove image borders and rock outcrops from the detection product.

2.2.1 The Normalised Radon Transform

The Radon transform is the line-integral of the image (or cut-out window) intensity along a projection axis (ρ) oriented at a specific angle (θ) (Oppenheim and Willsky, 1996). An example is shown in Figure 2.1 for rotation $\theta = 90^\circ$ and $\theta = 45^\circ$. By repeating the line-integration for axes oriented at all angles $\theta = 0^\circ$ to $\theta = 180^\circ$, a 2-D feature space $R(\rho, \theta)$ is constructed. In NeRD, a normalisation step similar to Öznergiz et al. (2014) is added to the Radon transform by normalizing the line-integral over each projected axis ρ to the number of pixels $N(\rho, \theta)$ within the integral. The Normalised Radon transform is computed as:

$$R_{norm}(\rho, \theta) = \frac{1}{N(\rho, \theta)} \sum_x \sum_y I(x, y) \delta(\rho - (x \cos \theta + y \sin \theta)) \quad (2.1)$$

where $I(x, y)$ denotes the value of the image intensity at (x, y) coordinates, and δ is the delta Dirac function (Oppenheim and Willsky, 1996; Öznergiz et al., 2014). The range of the transform coordinates is a half circle ($0 \leq \theta < \pi$). The result of the transform is a 2-D feature space at different azimuthal orientations (θ) as can be seen in Figure 2.2 panel a2-e2.

The variability of $R_{norm}(\rho, \theta)$ indicates the level of contrast for every projection axis. This maximises on the cross-section of narrow linear features, i.e. when the feature is

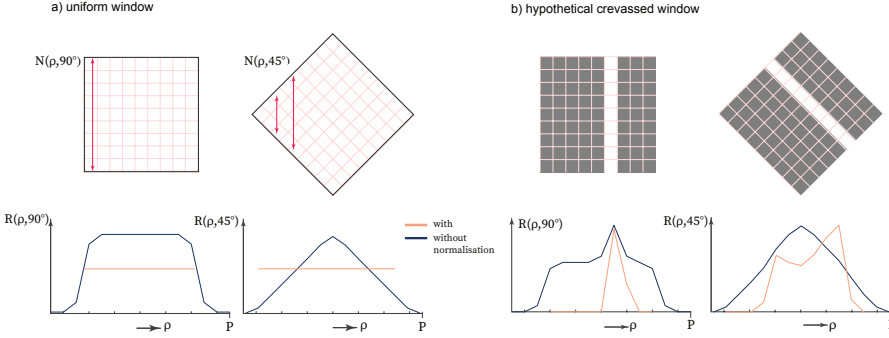


Figure 2.1: **Concept of the (Normalised) Radon transform** for two idealised image cut-out windows, **(a)** a uniform window (white value 1) without any variation in pixel values, **(b)** a window with a simplified representation of a crevasse (gray value 0.5 and white value 1). The figure shows the line-integral calculated for different projection axis ρ at angle θ , with (orange) and without (blue) normalisation. $R(\rho, \theta)$ is shown here for $\theta = 45^\circ$ and $\theta = 90^\circ$. N denotes the number of pixels in the line integral for every projection, P denotes the number of steps within the domain of the projection axis.

perpendicular to the projection axis. This shows in the line-integral as a sharp narrow peak, as is illustrated in Figure 2.1b. The signal response (σ) is therefore calculated as the standard deviation of R_{norm} for all projection angles, which is then filtered with a running median filter of size two ($\Delta = 1^\circ$) to remove noise (Gong et al., 2018):

$$s(\theta) = \sqrt{\frac{1}{P-1} \sum_{i=1}^P (R_{norm}(\rho, \theta) - \overline{R_{norm}})^2}, \quad (2.2)$$

$$\sigma(\theta) = \text{median}\{s(\theta - \Delta), \dots, s(\theta + \Delta)\}. \quad (2.3)$$

Here P denotes the number of steps within the domain of the projection axis ρ . For $\theta = [0, 90, 180]$, P is equal to the width of the window. For $\theta = 45^\circ$, P is equal to the diagonal of the window.

The signal response (σ) is shown in Figure 2.2 panel a3-e3. The projection angle with the maximum signal response $\sigma(\theta)$ is extracted as the dominant crevasse signal value of the window:

$$\sigma_{crev} = \max(\sigma(\theta)). \quad (2.4)$$

2.2.2 Damage Signal and Orientation

After extracting the crevasse signal (σ_{crev}) for every window, σ_{crev} is translated into a damage signal (\hat{D}). A signal $\sigma(\theta) > 0$ will be found by NeRD for any window with non-uniform pixel values. This includes noisy windows that contain no damage feature

and that should be removed from the damage detection product. We therefore apply a crevasse signal threshold τ_{crev} to remove the noise background signal. The damage signal \hat{D} is then defined as:

$$\hat{D} = \begin{cases} \sigma_{crev} - \tau_{crev}, & \text{if } \sigma_{crev} \geq \tau_{crev}, \\ 0, & \text{otherwise.} \end{cases} \quad (2.5)$$

The threshold τ_{crev} represents the ‘noisy signal value’. τ_{crev} is calculated separately, and varies slightly according to the data source and window size that σ_{crev} is calculated on (further detail in Section 2.4.2). Because R_{norm} values are between 0 and 1 the standard deviation and thus σ_{crev} has a maximum value of 0.5 (Shalom and Mandeville, 1982). Consequently, $\hat{D} \in [0, 0.5 - \tau_{crev}]$, where value 0 represents intact ice. The maximum value for \hat{D} is reached at maximum black/white contrast values. This can occur for full-depth rifts with ice/ocean contrasts but might also occur for surface crevasses with dark shadows. \hat{D} therefore does not directly present mechanical degradation of the ice such as the often used (depth integrated) isotropic scalar damage in continuous damage mechanics (CDM) modelling (Borstad et al., 2012, 2013, 2016; Sun et al., 2017).

The projection angle θ for which the maximum crevasse signal occurs is rotated 90° to represent the accompanying damage orientation $\alpha_{\hat{D}}$:

$$\alpha_{\hat{D}} = \theta - 90^\circ. \quad (2.6)$$

The interpretation of $\alpha_{\hat{D}}$ is more intuitive to interpret after a 90° rotation, as it then references the orientation of longitudinal direction of the feature with respect to the image horizontal. For example in Figure 2.1b, σ maximises at $\theta = 90^\circ$. At this angle, the line-integral results in the most pronounced sharp peak and thus has the largest signal response $\sigma(\theta)$. The resulting damage orientation will be $\alpha_{\hat{D}} = 0$ which intuitively corresponds to the horizontal line of the window. More examples and explanations are provided in Section 2.2.3.

2.2.3 Proof of Concept

In this section we illustrate that normalisation of the Radon transform solves the three issues mentioned earlier: i) it removes false signals, ii) the signal value is independent of the number of pixels in the window, and iii) the signal value is unbiased to average pixel intensity values. Consequently, NeRD solely depends on the contrast of the linear feature.

To illustrate the differences, we performed the Radon transform with and without normalisation on a set of idealised windows that portray simplified crevasses. The results are displayed in Figure 2.2, where every panel shows an idealised window in row 1, its 2-D feature space $R(\rho, \theta)$ with and without normalisation in row 2, and its signal response $\sigma(R)$ with and without normalisation in row 3 – from which σ_{crev} is extracted.

Panel Figure 2.2-a1 displays a uniform window with gray-scale values of 1. This example best illustrates the effect the number of pixels (N) have on the on the Radon transform. Without normalisation, $R(\rho, \theta)$ changes for different projection angles (panel a2), yielding $\sigma(\theta) \neq 0$ (panel a3). False local maxima signals appear at $0^\circ, 45^\circ, 90^\circ, 135^\circ$ and 180° (panel a3), and the maximum signal corresponds to $\theta = 0^\circ, 90^\circ$ or 180° . The false signals

are the result of the changing length of the projection axis for different rotation values as the projection axis varies between the window width ($\theta = 0^\circ, 90^\circ$ or 180°) and window diagonal ($\theta = 45^\circ$ or 135°). Consequently, for shorter projection axis, ρ is padded with zeros to fill the 2-D space of $R(\rho, \theta)$ to maximum length P . This padding creates an artificial jump in $R(\rho, \theta)$ values that results in false signals (see also Figure 2.1a). Now, with normalisation, padding with zeros and the artificial jump is unnecessary as P is allowed to vary with each projection angle. Therefore, a uniform window will result in $R_{norm} = 1$ and an extracted signal $\sigma_{crev} = 0$.

Panels Figure 2.2b-c illustrate that the Normalised Radon transform is independent of the average pixel intensity values. These examples show the same feature, with the same contrast value of 0.5: a background pixel intensity 0/0.5 and line intensity of 0.5/1, for panel b1 and c1 respectively. In these examples, the values of R_{norm} and σ_{crev} are identical despite the shift in the average intensity values: $\sigma_{crev} = 0.12$. Without normalization this is not the case: the signal response changes from $\sigma_{crev} \approx 0.9$ to 2.55 (panel b3-c3).

Finally, Figure 2.2d-e shows that the Radon Transform without normalisation gives more weight to long linear features, while the Normalised Radon transform puts more weight on linear features with high contrast values. This effect is illustrated in panels d1/e1 which show a long, high/low-contrast linear feature at $\theta = 90^\circ$ and a short, low/high-contrast feature at angle $\theta = 45^\circ$, respectively. In window d1 the extracted crevasse orientation is $\theta = 90^\circ$ ($\alpha_D = 0^\circ$) with and without normalisation, corresponding to the long, high-contrast feature. There is a difference in the value for σ_{crev} (panel d3), though. For window e1, however, the extracted crevasse orientation differ with or without normalisation. Without normalisation, the dominant signal remains at $\theta = 90^\circ$, here corresponding to the long, *low*-contrast feature, whereas the Normalised Radon transform yields $\theta = 45^\circ$, corresponding to the short, *high*-contrast feature. This indicates that Normalized Radon transform gives more weight to feature contrast than length.

2.3 Study Area and Data

2.3.1 Study Area

We applied the proposed NeRD method to the ice shelves in the Amundsen Sea Embayment in Antarctica. We considered all ice shelves between $100^\circ - 125^\circ$ West, which contains the Abbot, Cosgrove, Pine Island, Thwaites, Crosson, Dotson and Getz ice shelves.

The Amundsen Sea Embayment in West Antarctica is currently the largest contributor to sea-level rise (Pattyn and Morlighem, 2020). Most mass loss in the past decades is from Pine Island and Thwaites Glacier (Arndt et al., 2018; Meredith et al., 2019). Crosson and Dotson are two of the most rapidly changing outlets in West Antarctica (Lilien et al., 2018), but Thwaites Glacier is undergoing the largest changes of any ice-ocean system in Antarctica (Miles et al., 2021). The ice flow acceleration and ice shelf thinning is associated to grounding-line retreat (Pattyn and Morlighem, 2020; Arndt et al., 2018). Damage on these ice shelves has been considered key to their retreat (Glasser and Scambos, 2008; Borstad et al., 2012; Lilien et al., 2018; Lhermitte et al., 2020). Also Getz ice shelf was shown to be accelerating (Chuter et al., 2017).

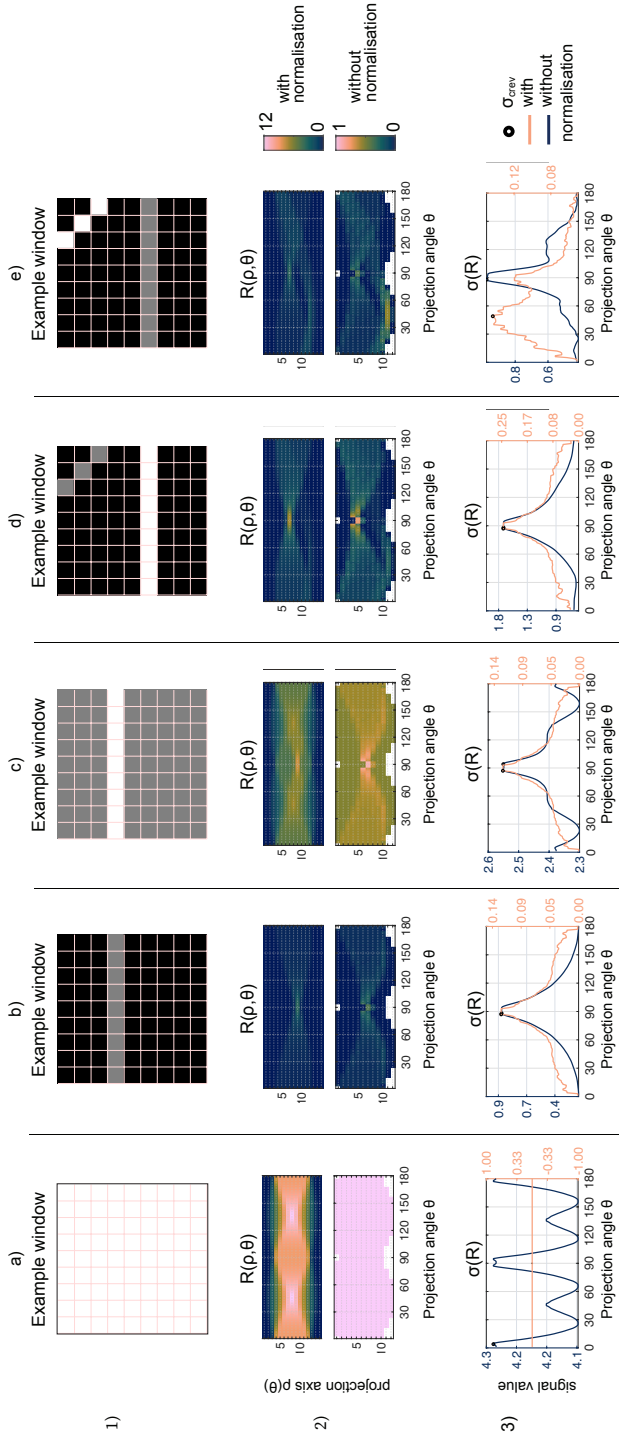


Figure 2.2: **Idealised scenarios to illustrate the differences between the Radon transform with and without normalisation.** Panel (a-e) represent different scenarios to which the Radon transform is applied: (a1-e1) show an idealised window with a hypothetical crevasse, (a2-e2) show the corresponding 2-D feature space $R(\rho, \theta)$ without and with normalisation (respectively top and bottom), and (a3-e3) the signal response $\sigma(\theta)$ with and without normalisation - from which σ_{crev} is extracted (black dot).

Given the presence of multiple fast changing, fast flowing and heavily damaged ice shelves in the Amundsen Sea Embayment, assessing the amount of damage in this area is of primary interest to improve our understanding of the link between damage, mechanical weakening and ice shelf instability.

2.3.2 Satellite Imagery

To evaluate the NeRD method, we applied it to a variety of satellite data sources ranging from Sentinel-2 Level-1C, Landsat 7 and Landsat 8 Collection 1 Tier 2 Top of Atmosphere Reflectance images and Synthetic Aperture Radar (SAR) Sentinel-1 Ground Range Detected images. All images were pre-processed in Google Earth Engine (Gorelick et al., 2017) and were exported at the same 30 m resolution as images from the Landsat series in WGS 84 Antarctic polar Stereographic projection (EPSG:3031). Sentinel-1 (10 m) and Sentinel-2 (10 m and 20 m) images were re-sampled using the nearest neighbour method. The MEaSUREs Antarctic ice shelf boundaries dataset of Rignot et al. (2016) was used to select satellite imagery over the ice shelves in the study area, and later to plot the grounding line on the spatial figures.

The satellite imagery was pre-processed in two ways to obtain a single, frame-filling image for every austral summer (December, January, February; DJF). Firstly, the optical satellite images were obtained by constructing a *median composite* image. This consisted of the following steps: subsetting the image collection to DJF data only, filtering for cloud cover ($< 20\%$) and compositing into median annual DJF composites of the Red (R), Green (G), Blue (B) reflectance bands. Calculating the DJF median of the image collection introduces a resolution loss of surface features due to a blurring effect as a result of glacier displacement. Especially fast flowing ice shelves, such as Pine Island, Thwaites and Crosson, show significant ice displacement throughout one austral summer with velocities up to 5 km/year (Gardner et al., 2019; Mouginot et al., 2017a). Shortening the image composite interval would reduce this blurring effect, but severely limits the available images, often leaving large gaps in the data. To show the capability of NeRD as an automated approach, applied to automatically retrieved data of sufficient quality, it was opted in this study to work with optical DJF median composites rather than monthly composites or individual scenes.

Secondly, SAR images were obtained by constructing a *spatial mosaic* image, stitching individual scene together until the export frame was filled. SAR data does not require filtering for cloud cover, and thus a qualitative image for a chosen period can be generated automatically without compositing. The SAR images were not filtered to remove speckle noise, as a noise removal step is already included in the NeRD method. The Sentinel-1 collection was filtered to only include HH polarization images of Interferometric Wide Swath instrument mode and descending orbit in the defined DJF period.

Supplementary Figure 1 displays the retrieved Sentinel-2 median composite images for DJF 2020-2021 for Pine Island, Thwaites, Crosson and Getz ice shelves. Supplementary Table 1 provides an overview of image median composites and spatial mosaics used in this study for each satellite source.

2.4 Methods

NeRD is intended to be a generalised, one-size-fits-all method: a method that can be applied to images from different spatial or temporal domains and yield results that can be compared. Therefore, we first performed sensitivity tests to show the robustness of NeRD (Section 2.4.1) to its inputs before applying NeRD to the Amundsen Sea Embayment study area (Section 2.4.2) and validating the results (Section 2.4.3). In a final step we have applied NeRD to a timeseries of imagery over the Pine Island Glacier to analyse its temporal consistency.

2.4.1 Sensitivity Analysis

The sensitivity of NeRD to its parameter settings and input was tested in two experiments. The first ‘resolution sensitivity’ experiment focuses on the choice of processing window size in combination with the image pixel resolution. The second ‘sensor sensitivity’ experiment considers the sensitivity of the result to different data inputs. For this we consider both the choice of spectral bands in optical data, as well as the difference between optical and SAR data.

Resolution Sensitivity

First, the sensitivity of the NeRD method to the choice of window size was tested. The choice of window size is a compromise between desired high output resolution, and accurate feature detection. On the one hand feature detection in small window sizes yield high output resolution. On the other hand, feature detection in small windows is more susceptible to noise because the linearity of a feature typically is less pronounced in small windows where linear features have lower length to width ratios. Since the high length to width ratios of linear features determines the signal value in R_{norm} , it will result in lower damage signals. Consider for example an open rift of 100 m wide and 10 km long. A small window of 10x10 m can ‘fall into’ the rift and miss its detection. Detection is possible if the small window covers the edge of the rift, and the edge is discernible as a linear feature from surrounding surface irregularities (noise) within the window. A larger window improves the confidence of feature detection over noise (Roberts et al., 2013) as a larger window size (e.g. 1 km x 1 km) spans the rifts opening and clearly shows the orientation of the rift. A drawback of this larger window size is that other features which are present in the window might be overridden by the large rift. The output of larger window sizes therefore potentially misses valuable spatial variations. As such, a balanced choice of window size relative to feature size is essential. Therefore, to test the effects of window size on the detected NeRD damage we performed a sensitivity experiment by varying the window sizes between 10x10 and 25x25 pixels, implying window sizes of 300x300 and 750x750 m, respectively. An example for these two window sizes is shown in Figure 2.3a and b.

Second, the sensitivity of the NeRD method to the image pixel resolution was tested. The resolution of the image mainly determines the minimum feature size that can be resolved, but also affects the contrast of features. Since wide linear features (e.g. rifts) can be located in a multitude of pixels in high spatial resolution imagery, the contrast of the rift edge/trough is effectively spread over more pixels. This lowers the length to

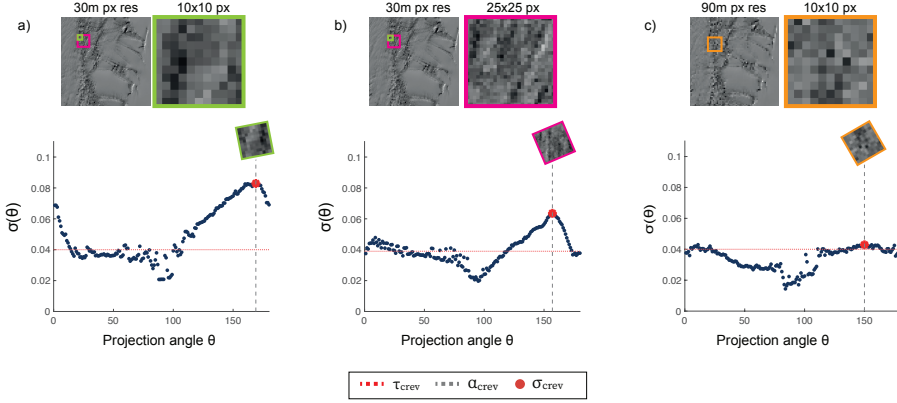


Figure 2.3: **Example of NeRD applied to different windows** of a Sentinel-2 RGB median composite of DJF 2019-2020, zoomed in to the western shear zone of Pine Island Ice Shelf. The image has been converted to a grayscale image with values between 0-1. The top row shows the selection of (a) a 10x10 (green) and (b) 25x25 (magenta) pixel windows from the image with 30 m pixel resolution, and (c) a 10x10 (orange) pixel window from a down-sampled image to 90 m pixel resolution. The bottom row shows the standard deviation $\sigma(\theta)$ of the normalised radon transform line integral at different projection angles θ . The resulting crevasse signal σ_{crev} at angle θ are denoted with a red dot and grey dashed line. The crevasse signal threshold τ_{crev} is shown as the red dashed line.

width ratio of the feature within a given window, and consequently reduces the ability of NeRD to detect it. To assess this effect of resolution on feature contrast, we apply NeRD on 10x10 windows of high-resolution images (30 m pixel resolution), and down-sampled versions of the same images (90 m pixel resolution). We down-sampled the images from 30 m to 90 m pixel resolution using a nearest neighbour approach that ensures that the contrast between every pixel group is enhanced. See an example for these two resolutions in Figure 2.3a and c.

For both the window size and pixel resolution tests, NeRD was applied to Sentinel-2 median image composites of DJF 2020-2021 in the Amundsen Sea Embayment study area. The number of detected damage pixels were counted, including all pixels where $\hat{D} > 0$, to allow a pixel-wise comparison between the individual experiments. To this end, the results of the low resolution tests (750 m window size or 90 m pixel resolution) were re-sampled back to the same grid as the high-resolution tests (300 m window size or 30 m pixel resolution).

Sensor Sensitivity

In the sensor sensitivity experiments we tested the effects of i) different spectral bands in optical data and ii) different data sources (optical versus SAR) on the obtained the damage product. For this purpose, the NeRD method was applied to the red (R; B4), green (G; B3), blue (B; B2), and short-wave Infrared (SWIR; B11) bands of a Sentinel-2 median image

composite (DJF 2019-2020) individually. Next, the robustness of the NeRD method to data acquired from different sensors was tested by applying it to both optical Sentinel-2 and Landsat 8 data and Sentinel-1 SAR data, which all were sampled to the same 30 m grid resolution to allow direct comparison. For this sensitivity experiment all images were processed on 10x10 pixel windows (30 m pixel resolution).

2.4.2 Application of NeRD

We have applied NeRD to the Amundsen Sea Embayment study area on Sentinel-2 median image composites of DJF 2020-2021. The images were processed on 10x10 pixel windows (300 m), based on the outcome of the sensitivity tests. The damage signal \hat{D} was quantified following Equation 2.5, for which a representative value of $\tau_{crev} = 0.040$ was determined (see next Section 2.4.2).

After validation of the results in the study area we applied NeRD with the same 10x10 px window size to a timeseries of median image composites on the Pine Island Glacier, consisting of two Landsat 8 median composites (DJF 2013-2014 and 2015-2016) and two Sentinel-2 median composites (DJF 2017-2018 and 2019-2020). This was done to analyse the temporal consistency of NeRD in more detail.

Noise Removal

The threshold (τ_{crev}) is a representative signal value of typical undamaged, noisy windows that is used to remove noise from the crevasse signal (Equation 2.5). This noise value depends on the variability of pixel intensity values within the processing window. What this means is that it can vary with different window sizes, as this will impact the signal to noise ratio of a feature. Moreover, τ_{crev} will vary with the use of a different data source since the amount of noise in the image differs between optical and SAR sources. τ_{crev} was therefore calculated for all window sizes used in this study, which range from 5x5 to 110x110 pixels, in combination with each Sentinel-1/2 and Landsat 7/8 data source. Although not every window size is used in combination with every data source, τ_{crev} is calculated for every combination to demonstrate its variability between data sources.

We selected three areas on the Pine Island (58 km²), Dotson (27 km²) and Getz (36 km²) glaciers that do not show any apparent signs of damage in the Sentinel-2 median composites and then exported images within the same area for every data source. Using these ‘undamaged’ areas, the crevasse signal threshold τ_{crev} was calculated as the mean crevasse signal value of all undamaged windows:

$$\tau_{crev} = \overline{\sigma_{crev,undamaged}}. \quad (2.7)$$

The resulting τ_{crev} values are shown in Table 2.1 and range from $\sigma \approx 0.03$ to 0.06. Changes of τ_{crev} between different window sizes are small. τ_{crev} changes more significantly from data source to data source: for 10x10 pixels, τ_{crev} ranges from low thresholds 0.032 (Landsat 7) and 0.040 (Sentinel-2) to high thresholds 0.050 (Sentinel-1) and 0.051 (Landsat 8).

Table 2.1: Crevasse signal threshold τ_{crev} , defined as the averaged crevasse signal value, $\overline{\sigma_{crev}}$, for undamaged areas. Values are aggregated for all windows in selected undamaged areas. Values are calculated depending on window size and data source.

window size		Number of windows	Crevasse signal threshold, τ_{crev}			
			Sentinel		Landsat	
			S1	S2	L7	L8
150m	5x5 px	8732	0.058	0.046	0.027	0.049
300m	10x10 px	2251	0.050	0.040	0.032	0.051
700m	25x25 px	376	0.044	0.039	0.037	0.065
3300m	110x110 px	27	0.042	0.034	0.027	0.031

2.4.3 Validation

Validation of NeRD method consisted of two comparisons: i) a comparison of detected damage pixels to manually labelled ground-truth damage map and ii) a comparison with the CNN fracture map of Lai et al. (2020).

Firstly, a manually labelled damage map was constructed using QGIS (Team, 2009) on the Sentinel-2 median image composites of DJF 2020-2021 in the Amundsen Sea Embayment area (30 m resolution). QGIS enables an interactive and dynamic view of the image, allowing us to map multiple types of damage features, including: i) individual linear features, ii) polygons with densely crevassed fields and iii) polygons with heavily damaged, disintegrated areas with open rifts and ice mélange. Polygons covering surface crevasse fields or heavily damaged areas are visibly distinctive by the feature size included in the area. The identified linear features can indicate rifts, snow covered rifts, or basal crevasses (McGrath et al., 2012b). The resulting labels are shown in Supplementary Figure 2. We predominantly identify surface crevasse fields on the ice tongue of Pine Island glacier, heavy damage in the shear zones of Pine Island, Crosson and Thwaites glaciers, and large linear features predominantly on Crosson and Getz glaciers. The labelled damage vectors were rasterised onto the 300 m grid of the produced damage maps, to determine True Positive (TP), True Negative (TN), False Positive (FP) and False Negative (FN) detected pixels. With these, the accuracy, precision, recall and f1-score metrics were calculated to assess the performance of NeRD (Stehman, 1997; Taha and Hanbury, 2015):

$$\begin{aligned}
 accuracy &= \frac{TP + TN}{P + N}, \\
 precision &= \frac{TP}{TP + FP}, \\
 recall &= \frac{TP}{TP + FN}, \\
 f1 - score &= \frac{FP}{N}.
 \end{aligned}$$

Because of a strong imbalance between the number of damaged to undamaged pixels the macro-averaged f1-score was calculated. This is the unweighted mean of the metrics calculated for each label, and gives a relatively high penalty to errors in the minority (damaged pixels) class (Taha and Hanbury, 2015).

Second, NeRD was compared in a two-resolution approach to the CNN fracture map of Lai et al. (2020). The CNN architecture consists of multiple convolution and max-pooling layers that encode and decode the data. The input/output resolution is 125 m, corresponding to the MOA2009 dataset to which the CNN is applied. The receptive field of the CNN, however, spans 3500 m for each pixel (calculated based on Araujo et al. (2019)). We therefore compare results from NeRD to both these scale levels. To this end, we applied NeRD on a Landsat 7 DJF 2008-2009 median image composite which covers the same austral summer as MOA2009 (Haran et al., 2014), at two resolutions: once using 5x5 pixel windows and 110x110 pixel windows (30 m pixel resolution). This corresponds to 150 m and 3300 m window sizes respectively, thus comparing detected damage at similar resolutions as the CNN input/output and receptive field resolution. Additionally, NeRD was applied directly to the 125 m resolution MOA2009 image itself, with a 10x10 pixel window size (1250 m). The combination of these approaches allows to compare (a) the ability of NeRD and the CNN to resolve damage features and (b) the likeness of the results when applied to the same data.

2.5 Results

2.5.1 Sensitivity Analysis

Resolution Sensitivity

The map and bar-chart in Figure 2.4 and 2.5 show the sensitivity of NeRD to window size and pixel resolution, highlighting that the changes in detected damage pixels in both resolution sensitivity tests are small as both high and low resolution tests detect similar features. Although the detected damage area is somewhat larger in the low resolution tests, Figure 2.4 shows that this increase in damage area occurs adjacent to the high-resolution detected damage areas. These pixels therefore do not necessarily represent newly detected damage features, but mostly represent a widened detection of the same features. We therefore make a distinction in the bar-chart in Figure 2.5, where damaged pixels are grouped into four classes: (i) pixels that are detected in both pixel- or both window resolution tests (blue bars), (ii) pixels that are detected only by low pixel- or low window resolution test, but are directly adjacent to high resolution detected damage pixels (green bars), (iii) the remaining pixels that are detected only by low resolution test (pink bars), and (iv) pixels that are detected only in the high resolution test (orange bars). As group (i) and (ii) represent the same features, they can be combined for interpretative purposes.

On Pine Island, Thwaites and Crosson ice shelves, approximately 50% of the total damaged pixels are detected by both pixel- or both window resolution tests (blue bars). Adding to that the adjacent detected damage pixels of group ii (green bars), the figure shows that a total of 73%-83% of the detected damage features are represented in both resolution

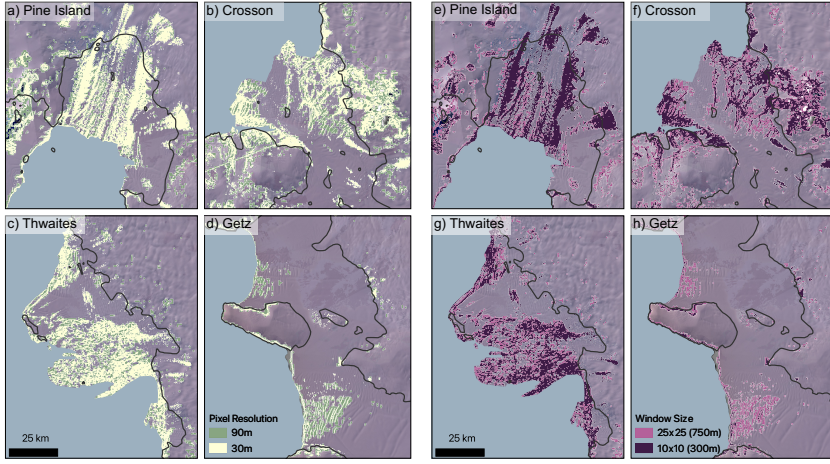


Figure 2.4: **Resolution sensitivity.** Binary detected damage (pixels where $\hat{D} > 0$) for two resolution sensitivity experiments on the selected ice shelves in the study area: Pine Island (a & e), Thwaites (b & f), Crosson (c & g) and Getz (d & h). Panels (a-d): detected damage for different pixel resolutions, native (30 m) versus down-sampled (90 m) resolution. Panels (e-h): detected damage for different window sizes, 10x10 pixels (300 m) and 25x25 pixels (750 m). Data is overlaid on used input images, Sentinel-2 RGB median image composites (DJF 2020-2021), grounding lines (dark grey line, Rignot et al. (2016)) and an ocean mask (light blue area, adjusted from Mouginot et al. (2017b)).

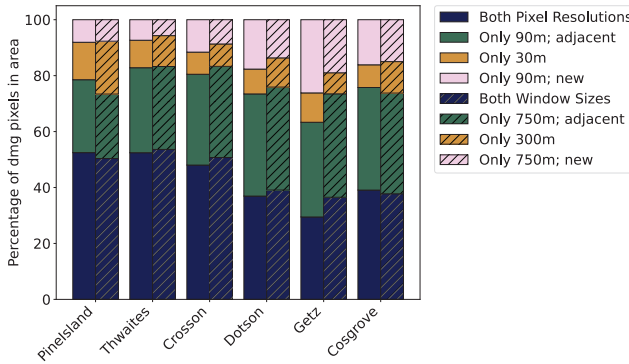


Figure 2.5: **Resolution sensitivity.** Bar-chart of detected damage pixels grouped per ice shelf, normalised for the total number of pixels detected by both pixel resolution tests (uniform bars) or both window resolution tests (hashed bars). The pixels are grouped by: pixels that are detected in both pixel- or both window resolution test (blue bars), pixels that are detected only by the low resolution test but are directly adjacent to high resolution detected damage pixels (green bars), the remaining pixels that are detected only by low resolution test (pink bars), and pixels that are detected only in the high resolution test (orange bars).

tests on these three ice shelves. On Pine Island, 13.4% (18.9%) damage pixels are detected by only the high pixel (window) resolution tests (orange bars), versus 8.1% (7.7%) pixels by only the low pixel (window) resolution tests (pink bars). In this case a lower pixel (window) resolution decreases the detection of damage features: a net effect of -5.3% (-11.2%). For the other ice shelves, however, the lower resolution tests yields roughly the same or more detected damage features. The latter is especially the case on Getz ice shelf, where 26.2% (19.0%) of the damage pixels are detected only by the low pixel (window) resolution tests, with respect to 10.5% (7.5%) pixels that are only detected by the high resolution tests - a net increase of 15.7% (11.5%). Figure 2.4d and 2.4h show that this increase in detected damage pixels improves the detection of large rifts. The effect is larger for the low pixel resolution tests (90 m pixel resolution) than for the low resolution window size test (25x25 pixels), indicating that down-sampling the high resolution image with contrast enhancement benefits the detection of these wide linear features.

Overall, the sensitivity tests highlight that NeRD is robust to choice of window size and pixel resolution: the changes in detected damage pixels are small and changes in detected damage patterns minimal. A reduction of pixel/window resolution can increase as well as decrease the detected damage features, but is only beneficial for areas with predominantly (large) linear damage features. With this in mind, and the intention to get a high resolution damage map of multiple types of damage, we therefore continue with the application of NeRD on 30 m pixel resolution images, applied to 10x10 pixel window sizes.

Sensor Sensitivity

This experiment considers both sensitivity of NeRD to the choice of spectral bands in optical data, as well as the differences when applied to optical or SAR data.

We show the sensitivity of NeRD to the R, G, B and Short-Wave Infra Red (SWIR) spectral band of Sentinel-2 (spatial mosaic of DJF 2019-2020) in Figure 2.6. The figure displays detected damage for each spectral band individually (Panel a, b, c, e) with the original band data in the top row. Panel (d) shows an RGB plot of the individual bands (top) and cumulative detected damage on the individual R,G,B bands (bottom), such that the color scheme indicates in which band(s) damage has been detected. The majority of the pixels in panel (d) are colored white, meaning damage is detected in all bands. This test confirms that differences between R, G and B bands are small, and that the most complete detection will be achieved when using all three bands. This test also shows that the SWIR band is very sensitive to any remaining cloud properties or variability of this band between individual scenes that are used to construct the DJF image. Because of this, we have excluded SWIR as a potentially useful band.

Figure 2.7 and Table 2.2 show the results of the second sensitivity test. For this, NeRD is applied to three different data sources: Sentinel-2, Landsat 8 and Sentinel-1 respectively. Table 2.2 shows that NeRD detects almost twice as much damage pixels in the Sentinel-1 image than in the Sentinel-2 and Landsat 8 images. Despite this quantitative difference, the map in Figure 2.7 clearly shows that the areas with high damage signal values are detected on all data sources. This includes almost the entirety of the western shear zone, the ice front and the damage in the Western tributary. This result indicates the robustness

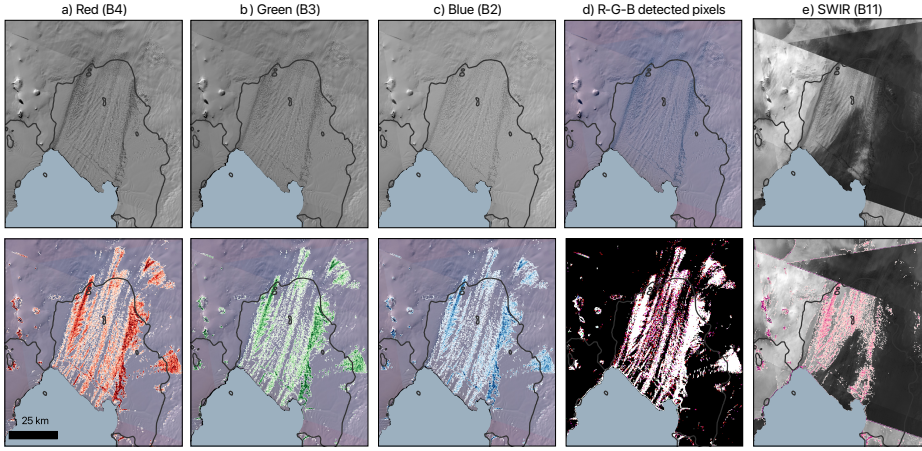


Figure 2.6: **Sensor sensitivity.** Detected damage by NeRD applied to the separate optical bands **(a)** Red, **(b)** Green, **(c)** Blue and **(e)** Short-Wave Infra-Red of a Sentinel-2 image of the summer 2019-2020 **(d, top)**. Panel (d, bottom) shows an RGB plot of the Red, Green and Blue detected damage together, such that color scheme indicates in which band(s) damage was detected. A purple color is damage detected in both red and blue bands, white indicates detection in all three bands. Grounding lines (dark grey line, Rignot et al. (2016)) and an ocean mask (light blue area, adjusted from Mouginot et al. (2017b)) are added to the plot.

of the method to identify the consistent heavy damage patterns across the different data types.

Most of the pixels that are detected in Sentinel-1 but not in Landsat 8 or Sentinel-2 are pixels with low damage signal values ($\hat{D} < 0.10$); see Figure 2.7d. Moreover, these pixels are located mainly on the ice shelf tongue, where mostly small scale surface crevasses are found. The difference in detection between SAR and optical data on these small scale features can be attributed to the pre-processing of the data sets. The use of median composites for optical data results in a blurring effect, caused by ice displacement. This blurring also explains why the large open rift near the ice front is only partially detected in the optical images.

Overall the results of the sensor sensitivity indicate the robustness of the method to consistently identify damage patterns across the two data types. Although the amount of detected damage varies, differences arise mostly for low damage values. This result emphasises the complementarity of SAR and optical data for damage detection.

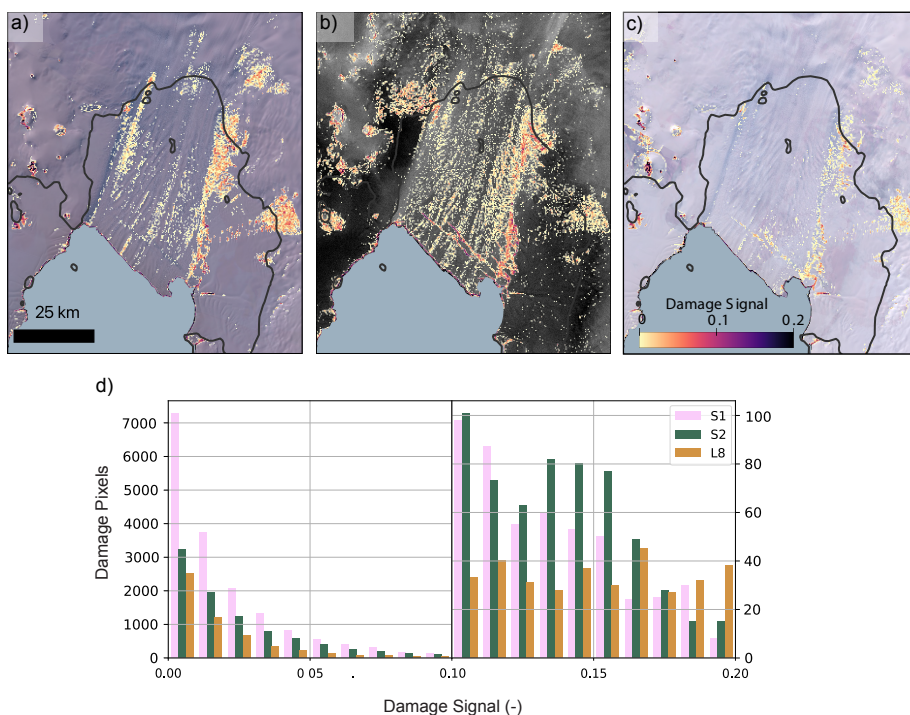


Figure 2.7: **Sensor sensitivity.** Damage detected on images of the Pine Island Glacier in December 2019 for (a) Sentinel-2, (b) Sentinel-1 and (c) Landsat 8 image, using window sizes of 10x10 pixels (300 m). (d) the binned pixel count of detected damage pixels for the range of damage signal values for each source. Sentinel-2 and Landsat 8 images are median composites and Sentinel-1 is a spatial mosaic of DJF 2019-2020. Grounding lines (dark grey line, Rignot et al. (2016)) and an ocean mask (light blue area, adjusted from Mouginot et al. (2017b)) are added to the plot.

Table 2.2: **Sensor sensitivity.** Detected damaged pixels counted for the different sensors, Sentinel-2 (S2), Sentinel-1 (S1) and Landsat 8 (L8). The table compares (not) overlapping damage pixels between the sensors. Each row compares the percentage of that sensor that overlaps with the other in the columns. The cell that displays the overlap of a sensor with itself (i.e. overlap of Sentinel-2 with Sentinel-2) is *italic*, indicating the amount of pixels that is only detected by that sensor and no other.

		Detected px in combination with sensors..			
	Total \hat{D} px	All-sensors (%)	.. with S1 (%)	.. with L8 (%)	.. with S2 (%)
Sentinel-2	9442	33.5	25.8	12.7	<i>28.0</i>
Landsat 8	5939	53.2	9.8	<i>16.7</i>	20.3
Sentinel-1	16975	18.6	<i>63.6</i>	3.4	14.3

2.5.2 Damage Detection at the Amundsen Sea Embayment

Figure 2.8 shows the damage detected as result of the NeRD method across the ice shelves in the Amundsen Sea Embayment. Most damage pixels and the strongest damage signals (\hat{D}) are detected on the Pine Island, Crosson and Thwaites ice shelves. The results show moreover that high damage signals ($\hat{D} > 0.1$) are mostly found in the shear zones of these ice shelves, while lower damage values are detected on the ice tongues. Inspection of the source imagery (Supplementary Figure 1) shows that these areas with high damage signal values consist of heavily damaged ice, containing fully fractured rifts and ice mélange, while the damage area on the ice tongue are mostly surface crevasses (Supplementary Figure 2). NeRD also detects large linear rifts near the ice front of the Getz ice shelf, although these rifts show lower damage signal values: $\hat{D} \approx 0.02$ to 0.03 . This lower value of \hat{D} can be explained by lower image contrasts of rifts as a result of snow cover. This lower contrast also explains why the rifts in the upstream area of Getz are not detected by NeRD as the contrast in their cross-section is even lower there.

NeRD also detects the ice front for many of the ice shelves in the Amundsen Sea Embayment. The sharp gradient of the bright calving front and the darker sea in the optical images results in a strong damage signal. Although the calving front is not considered damage in the scope of this study, calving front detection could be considered a useful by-product of the NeRD method.

Interpretation of the NeRD damage on the grounded ice is more complicated than on the floating ice shelf. For example, nunataks upstream of Crosson ice shelf create shadows and contrast edges over the surrounding ice that are falsely detected as damage, as well as the coastline. Further post-processing can remove this by masking all the grounded ice or adding an ice height constraint to the data. We have refrained from doing so now, to fully illustrate NeRD capacities.

Damage Orientation

The orientation of the damage features ($\alpha_{\hat{D}}$) are displayed as a quiverplot in Figure 2.9, scaled in size to their respective damage signal value. For Pine Island, Thwaites, Crosson and Getz ice shelves a small part of the ice shelf is selected to comprehensively visualise the detected damage orientations.

Firstly, Figure 2.9 shows a good alignment of detected damage orientations to the visible edges of damage features. This is clear on Crosson and Getz ice shelf, where large rifts are tracked well, including a consistent alignment to the calving front (detected as damage feature) on Getz ice shelf and the consistent detected orientation of the two edges of open rifts on Crosson. In the shear zone of Pine Island, Crosson and Thwaites ice shelves the damage orientations are more chaotic, especially in the presence of ice rubble. Thwaites shows a relatively aligned damage field due to the block-wise structure of ice bergs in combination with the sun incidence angle that enhances the shadows of ice edges in one direction.

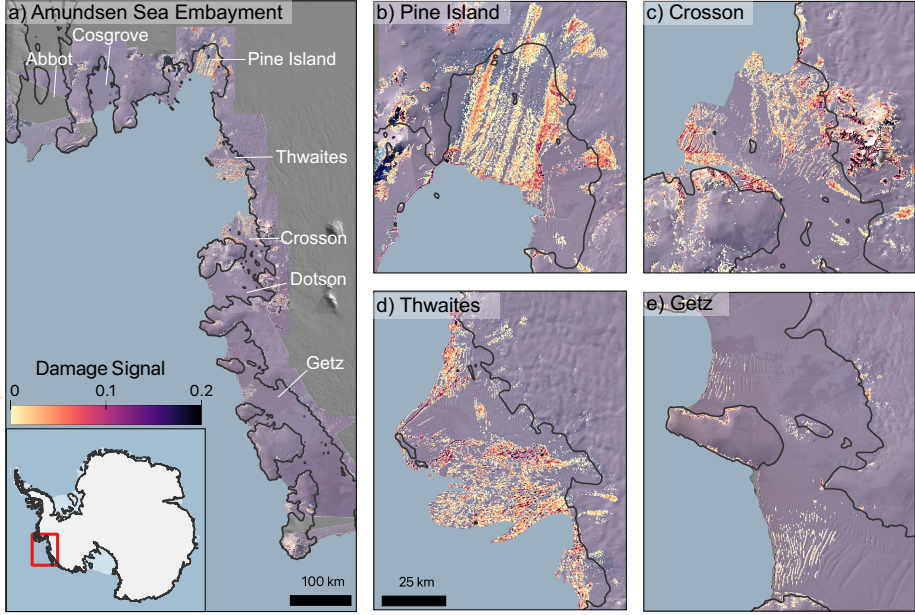


Figure 2.8: **Detected damage** (\hat{D}), as result of the NeRD method applied to ice shelves in the Amundsen Sea Embayment on Sentinel-2 median image composites for DJF 2020-2021, using red (B4), green (B3) and blue (B2) spectral bands. Panel (a) shows the full study area, panel (b-e) show zoom boxes for selected ice shelves. Grounding lines (dark grey line, Rignot et al. (2016)) and an ocean mask (light blue area, adjusted from Mouginot et al. (2017b)) are added to the plot.

2.5.3 Validation

Validation to Manual Labels

The validation of detected NeRD damage with manually labeled damage is shown in Figure 2.10, displaying true negatives (TN), false negatives (FN), false positives (FP) and true positives (TP). The corresponding confusion matrices are included in Supplementary Figure 3.

Firstly we note that the validation shows frequent detection of false positive damage pixels on grounded ice, which is especially prevalent upstream of Pine Island and Crosson ice shelves. This is the result of the earlier mentioned difficulties with terrain shadows. These false positive pixels over grounded ice restrict the obtained macro averaged precision in the Amundsen Sea Embayment study area to 0.69. For further validation metric calculations, all grounded ice was removed using the grounding line from Rignot et al. (2016). The grounded ice pixels are still visualised in Figure 2.10 to give a full representation of the validation. Removing the damage detection on grounded ice increases the macro averaged precision in the study area to 0.81.

The validation results show a good overall performance of the NeRD method, with an

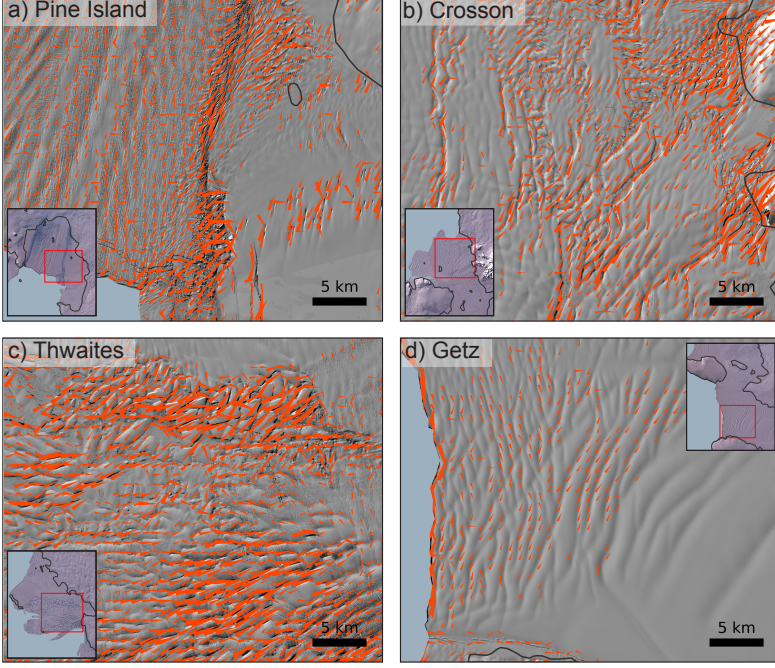


Figure 2.9: **Detected damage orientation** ($\alpha_{\hat{D}}$) for selected areas on **(a)** Pine Island, **(b)** Crosson, **(c)** Thwaites and **(d)** Getz ice shelves, as result of NeRD applied on Sentinel-2 median image composites for DJF 2020-2021, shown in gray-scale as background. The quivers are rotated with $\alpha_{\hat{D}}$ degree angles and scaled relatively to the damage signal value \hat{D} . For visual clarity the number of plotted quivers is reduced to one median value for every 3x3 pixel group.

accuracy of 0.95 across all ice shelves in the study area and a macro averaged f1-score of 0.80. The macro averaged f1-score on Pine Island, Crosson, Thwaites and Getz ice shelves are 0.79, 0.79, 0.77 and 0.69, respectively. For Pine Island, Crosson and Thwaites the macro averaged precision and recall are of similar value, all between 0.77 and 0.80. The relatively low f1-score for Getz ice shelf is the result of low recall (0.64) rather than precision (0.81).

These good performances are reflected in Figure 2.10, which shows a good representation of true positive detected damage pixels across the ice shelf tongues and in the shear zones. The limited number of false positive pixels (excluding grounded ice) explains the high precision, whereas the relatively sparse number of false negative pixels explains the high recall for most ice shelves. Only on Getz ice shelf the ratio of false negative pixels is relatively high, as a result of NeRD's difficulty to detect some of the wide upstream rifts. Moreover, the majority of false positive pixels on the ice shelves are located directly adjacent to true positive pixels. In many cases, this suggests a wider damage detection than that is labelled, rather than the detection of non-existing damage features.

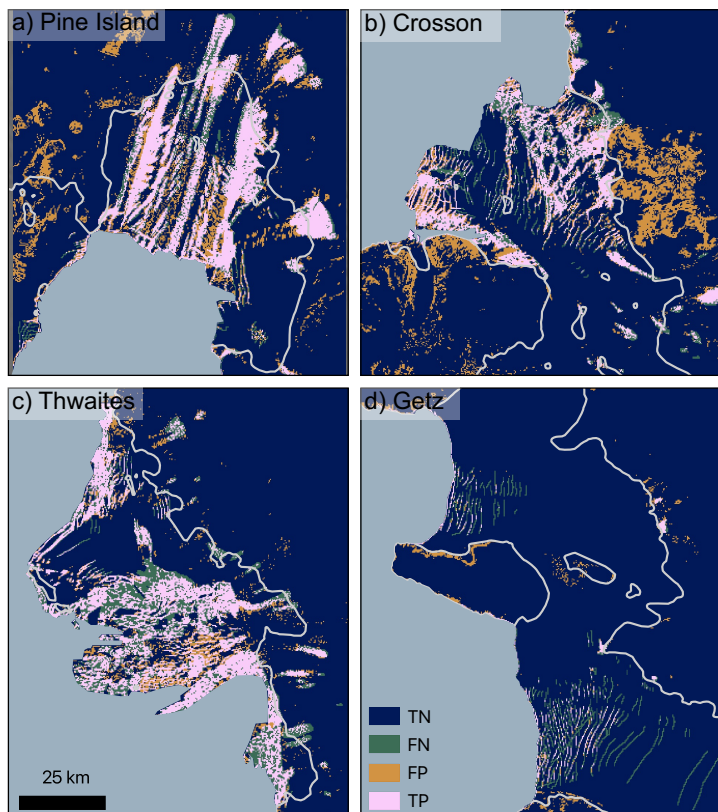


Figure 2.10: **Validation to labels.** Performance of detected damage by NeRD with respect to manually labelled damage features. Pixels are classified as True Positive (TP, pink), False Positive (FP, orange), False Negative (FN, green) and True Negative (TN, blue). Grounding lines (light grey line, Rignot et al. (2016)) and an ocean mask (light blue area, adjusted from Mouginot et al. (2017b)) are added to the plot.

In summary, the validation shows an overall good performance of the NeRD method to detect damage. The fact that the precision is consistent for the damage detected at all ice shelves in the Amundsen Sea Embayment indicates a robust damage detection method.

Comparison to Fracture Map

The comparison between the NeRD detected damage map and the fracture map of Lai et al. (2020) in Figure 2.11 shows different damage patterns for both methods on all four ice shelves. NeRD has been applied to Landsat 7 images on 150 m (5x5 pixels) and 3300 m (110x110 pixels) windows. For both, NeRD detects the same major damage areas, with some new areas showing up in the 3300 m results and some small scale features disappearing (e.g. on Thwaites ice tongue). The nuances due to resolution have been discussed

in Section 2.5.1, whereas this Section will focus on the difference between the damage detected by NeRD and Lai et al. (2020). Seeing the similarities between the 150 m and 3300 m damage maps, we continue the comparison to the fracture map with a focus on the 150 m resolution damage map.

Generally, the CNN fracture map of Lai et al. (2020) displays more linear features. This includes larger, more gradual, rifts and folds (Figure 2.11). This CNN method works well on the Getz ice shelf, where the CNN method detects most of the large rifts that are missed by the NeRD method. However, a down-side of the CNN's focus on large linear shapes is that the fracture map also includes flow lines that are morphological similar to these rifts (Ely and Clark, 2016). The benefit of NeRD is that, despite missing some of the large rifts, it correctly omits detection of flow lines.

We see a strong difference in performance between the CNN and NeRD method on the Pine Island and Crosson ice shelves. The CNN fracture map detects crevasse field areas on the ice tongues as a single fracture. These areas stand out with respect to the rest of the ice shelf tongue due to snow cover patterns. More importantly, the CNN method completely overlooks the erratically organised damage in the shear zones on both these ice shelves.

Also on Thwaites ice shelf NeRD detects high damage areas in the shear zone between the Eastern ice shelf and main tongue which are missed in the CNN fracture map. The CNN method, moreover, detects more linear patterns on the main ice tongue. This can be explained by the resolution of the used dataset: on the MOA2009 image with 125m pixel resolution, the ice fractures are indeed linearly oriented. On the higher resolution Landsat 7 image (30 m) the ice tongue displays a more block-like organisation of the ice.

To conclude: on the one hand, the NeRD method might overlook some wide and gradual rifts, as is characteristic on the Getz ice shelf and correctly detected by the CNN. On the other hand, the CNN fracture map of Lai et al. (2020) consistently overlooks heavy damage patterns that have an irregular shape, and also wrongly detect flow lines as fractures.

2.5.4 Damage Evolution

We analyse the evolution of damage over time by applying NeRD to satellite imagery of multiple years. Figure 2.12 shows an example time series of detected damage on Landsat 8 and Sentinel-2 median image composites of the Pine Island ice shelf during the austral summers of 2013-2014, 2015-2016, 2017-2018 and 2019-2020.

This time series show that the damage in the shear zones increased from 2013 to 2019. The ice tongue shows a more intra-annual variability: damage increases from 2013 to 2018 but then decreases in 2019 back to a similar pattern as 2015. This larger variability for the smaller surface crevasses on the ice tongue can be explained by two aspects. First, varying snow cover conditions can hide or reveal crevasses in the optical images of Landsat or Sentinel-2. On top of that, the number of images that are used for the median composite varies per season, depending on the number of images that pass the cloud filter, enhancing (many images) or reducing (few images) the blurring effect of

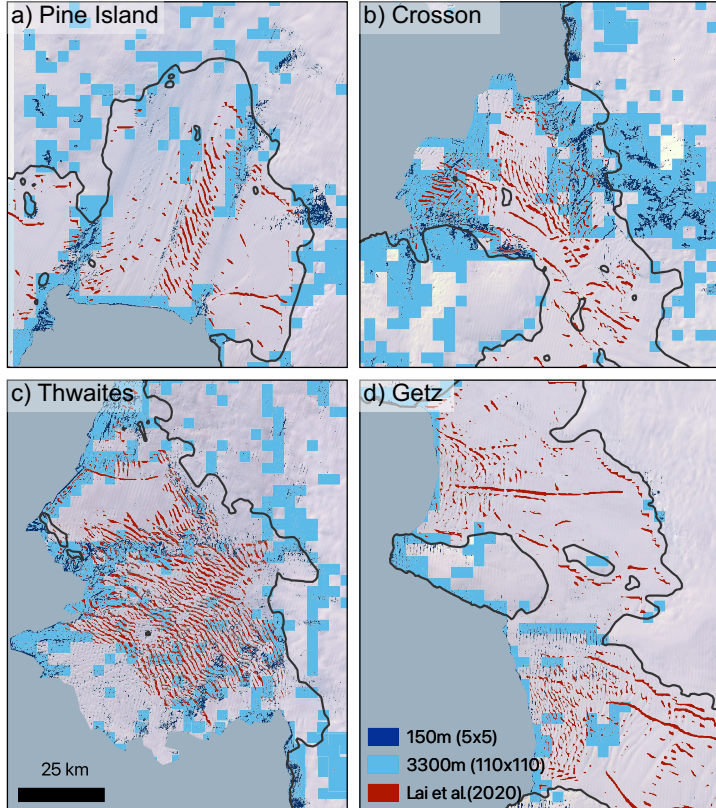


Figure 2.11: **Comparison to fracture map.** Detected damage (classified if $\hat{D} > 0$) on the Landsat 7 median image composite (background) for summer 2008-2009 on the selected ice shelves in the study area: **(a)** Pine Island, **(b)** Thwaites, **(c)** Crosson and **(d)** Getz ice shelves. Blue values indicate the detected damage by NeRD, applied to 110x110 pixel windows (3300 m, light blue, bottom layer) and 5x5 pixel windows (150 m, dark blue, top layer). Red values (middle layer) represent the detected fractures by Lai et al. (2020) using a machine learning approach, applied to the MODIS Mosaic of Antarctica 2008-2009 (MOA2009) on 125 m pixel resolution but based on a 3500 m receptive field. Grounding lines (dark grey line, Rignot et al. (2016)) and an ocean mask (light blue area, Mouginot et al., (2017)) are added to the plot.

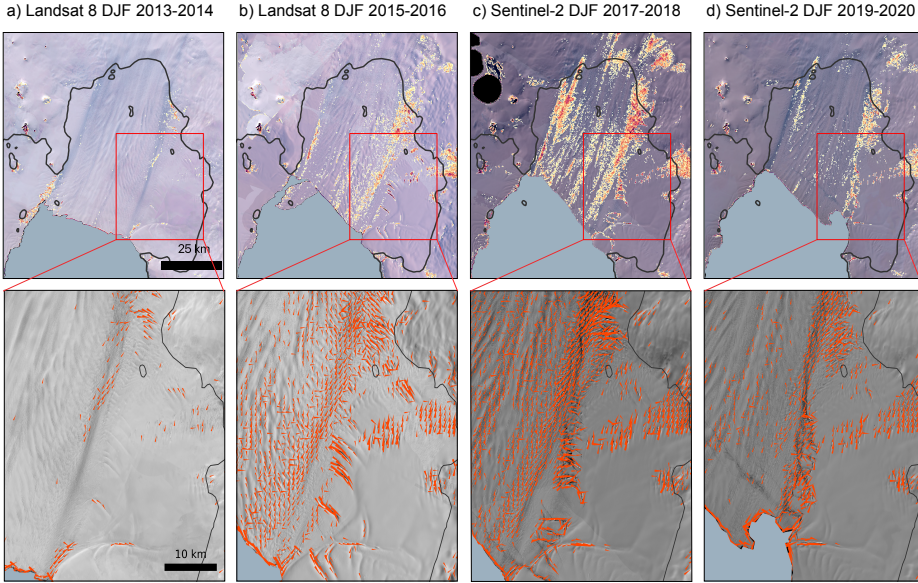


Figure 2.12: **Timeseries of detected damage.** Damage signal (top row) and orientation (bottom row) for damage detected on Landsat 8 and Sentinel-2 median image composites of the Pine Island Glacier during the summers (DJF) of **(a)** 2013-2014, **(b)** 2015-2016, **(c)** 2017-2018 and **(d)** 2019-2020. The zoom-boxes show the damage orientation in the western shear-zone close to the ice front, with the length of the quiver scaled to the strength of the damage signal. Grounding lines (dark grey line, Rignot et al. (2016)) and an ocean mask (light blue area, adjusted from Mouginot et al. (2017b)) are added to the plot.

the median image composite. This shows that a seasonal or annual variability related to surface crevasses can be imposed on the damage map.

The zoom-boxes in Figure 2.12 show initiation and evolution of damage in the western shear-zone of the Pine Island ice shelf. Large rifts first appeared in DJF 2013-2014 (panel a) and have opened and grown by DJF 2015-2016 (panel b). NeRD successfully tracks the rotation and opening of the rifts, aligning the detected damage orientation to the rift's edge. By DJF 2019-2020 (panel d), the individual rifts are no longer distinguishable and the area has become heavily damaged with little intact ice remaining. Hence, a more chaotic pattern of damage orientations is detected. All the while, the orientations of the crevasses on the ice tongue are quite consistently oriented throughout the years, and show a relatively aligned field of orientation. These crevasses are likely related to the vertical flexing of the ice shelf in response to the formation of basal melt channels, rather than changes in the local strain field (Vaughan et al., 2012), which can explain their consistent alignment.

The consistent tracking from developing rifts to disintegrated areas, both in terms of damage signal and orientation, indicates the qualitative performance of the method to detect damage.

2.6 Discussion

The different NeRD experiments have shown that the proposed NeRD method detects damage signal values primarily based on feature contrast rather than feature intensity. This removes false signals and dependencies on processing window size, both of which are prevalent in the classical Radon Transform. NeRD enables an automated application on different images and for different regions. This is in contrast to other damage detection methods, such as a CNN method that needs re-training for every data set, or manual mapping that is labour intensive and depends on expert judgement.

Sensitivity tests show that the detected damage product can change between -11 to +15% as a result of reducing the window or pixel resolution. The increase or decrease of detected damage pixels depends mainly on the type of damage features represented in the area. For heavily damaged ice shelves like Pine Island, Thwaites and Crosson, high resolution yields more detected damage. NeRD is most sensitive to a reduction of resolution in areas with wide features, as is seen on Getz ice shelf. In these areas, detection would improve by a reduced pixel/window resolution. As Cosgrove and Dotson ice shelves show similar sensitivity to window/pixel resolution as Getz ice shelf, we expect other lightly damaged ice shelves across the Antarctic to behave similarly. That aside, the sensitivity tests show a very robust and consistent detection of damage patterns.

With the NeRD method we are able to generate damage maps that can be analysed across space and time, because the quantified damage value is consistent for different spatial or temporal domains. This improves upon the previous crevasse map from Gong et al. (2018). Moreover, results consistently quantify damage patterns for all three tested data sources, paving the way for synergistic multi-source damage detection that overcomes remaining limitations from individual sources. The differences between damage detected from either optical or SAR data occur mainly for surface crevasses. Differences are caused primarily by the image pre-processing approach and by the image quality which is affected by clouds, shadows or illumination conditions, rather than by the NeRD method itself. The blurring effect that occurs in optical data due to compositing is a source for underestimated damage detection. Alternative to median composites one could construct spatial mosaics for optical data as well, which yields similar details of damage detection as shown on SAR data. Optical spatial mosaics, however, are much more susceptible to the mentioned image quality aspects than median composites (included in Supplementary Figure 5). This then would require more careful pre-processing, which did not fit the objective to develop an automated approach that can be applied out-of-the box to any data source.

With NeRD we are able to detect multiple types and scales of damage features. This is an improvement with respect to existing fracture maps. The fracture map of Lai et al. (2020) detects large-scale linear-like fractures on coarse data resolution, and the crevasse map of Bhardwaj et al. (2016) detects crevasses in a densely crevassed field on high-resolution data. The NeRD method is able to detect both densely crevassed fields and large scale rifts, and also includes the heavily damaged areas in the shear-zones. NeRD is a first-of-its kind method that detects continuous rather than binary damage features. It is this characteristic that allows NeRD to include the multiple types of damage features without losing comprehensible interpretation. Moreover, as high values of the detected

damage parameter \hat{D} seem to correlate to large (deep) damage features and low values to small (shallow) features, \hat{D} could potentially be linked to the scalar damage factor used in CDM modelling (Borstad et al., 2012, 2013, 2016; Sun et al., 2017) or to vertical crevasse information obtained from laser altimetry studies (Li et al., 2021; Wang et al., 2021). NeRD, however, is less suited to detect wide features with gradual slopes, especially compared to the CNN fracture map of Lai et al. (2020). This detection can be improved by down-sampling the image to enhance edge contrasts, but this is at the cost of spatial resolution of the final product. Furthermore, NeRD does not perform well in areas with changing terrain features, such as rock outcrops or hill shade. On ice shelves this is mostly a trivial issue, but future studies should take care to mask these features from the image.

The detection of damage orientation in addition to the damage signal adds to the potential uses of NeRD in future research. The robust tracking of rotating rifts can help improve our understanding of damage evolution. Furthermore, the detected damage orientation can be compared to the orientation of principal strain, using velocity data that is a close temporal match to the satellite imagery used for damage detection, which can provide insight in crevasse opening mode and can potentially be of help to initialise anisotropic creep damage models (Murakami et al., 1988; Pralong et al., 2006; Huth et al., 2021).

Lastly, an interesting by-product of NeRD is that it detects the ice front quite definitely. This has potential to help improve modelling of calving fronts (Enderlin and Bartholomaeus, 2020).

In summary, the NeRD method is robust and applicable for large scale assessments. The method is mainly limited by the quality of the input data. Therefore it is suggested that future studies focus on a robust pre-processing approach that consistently retrieves high quality data, which would combine well to the generalised application of the NeRD method. With such robust pre-processing the NeRD method can be applied to large spatiotemporal domains to allow Antarctic wide assessments, but also an application to year-round SAR data to analyse damage changes on a high temporal resolution.

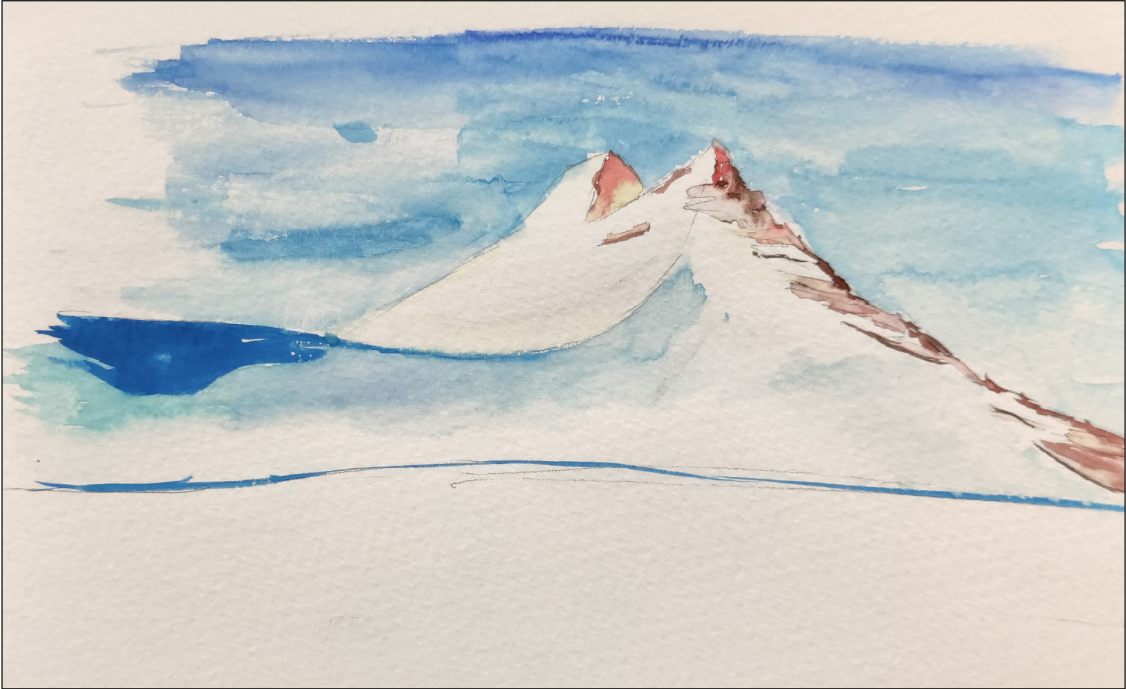
2.7 Conclusion

In this manuscript we have shown that the proposed NeRD method allows damage to be robustly detected across spatial and temporal domains. The method can be applied directly to different image sources, requiring no additional pre- or post-processing. This generalised application to multi-source imagery is a great advantage over previous fracture detection algorithms. With these characteristics the method is suitable for large scale damage assessments.

The ability of NeRD to detect continuous damage signal values allows detection of multiple damage feature scales. Furthermore, it enables the monitoring of damage development over time. We identified spatially varying damage patterns on the ice shelves in the Amundsen Sea Embayment, with most damage occurring on Pine Island, Thwaites and Crosson ice shelves. These ice shelves display heavy damage in their shear zones, indicating structural weakening of the ice. The consistent detection of damage orientation by NeRD provides insight in crevasse evolution. We analysed damage growth on

the Pine Island ice shelf, showing the initiation, advection and rotation of large crevasses that eventually develop into a disintegrated area.

With the NeRD method large scale damage assessments can be made. This in turn can help evaluate ice sheet models to their modelled damage pattern or possibly even calving front representation, or it can help initialise damage models. Large scale damage maps can also be used to train or evaluate machine learning approaches, or be combined with vertical properties of fractures from laser altimetry studies. Finally, temporal damage maps can potentially be used as an early-warning indication for ice shelves that are transitioning from an intact to a damaged state. In all cases, NeRD can be used as a tool to produce important insights regarding crevasse formation and ice shelf vulnerability.



Chapter 3

Assessment of Antarctic damage change over two decades

Together with Chapter 4, this chapter is based on: Izeboud, M., Lhermitte, S., de Roda Husman, S., Wouters, B. Antarctic ice shelves vulnerable to damage in future climate warming. *In review at Nature Climate Change*, NCLIM-24010280-T, 2024.

*With the development of the NeRD method, we are in the unique position to assess the state of damage and damage changes on Antarctic ice shelves for long time periods. In this chapter we first generate multiple damage maps of Antarctica, and quantify the changes. This addresses the research question: ‘**What is the current extent of damage across Antarctic ice shelves, and how has this damage evolved over the past decades?**’ We consecutively use those results in an analysis that investigates ‘**To what extent is detected damage correlated to ice shelf retreat?**’*

Section 3.2 describes the used satellite observations and Section 3.3 the steps to quantify damage change. Section 3.4 presents the detected damage change assessments and shows the implications of observed changes to ice shelf retreat.

3.1 Introduction

The potential instability of Antarctic ice shelves is a major uncertainty in current sea level rise projections, either due to short-term collapse or long-term weakening (Fox-Kemper et al., 2021; Robel et al., 2019). Understanding the processes that affect the weakening, retreat and instability of ice shelves is therefore essential (Bassis et al., 2023; Calvin et al., 2023). Damaged areas on an ice shelf, consisting of crevasses and/or rifts, are first indicators of its weakening (Borstad et al., 2012, 2017). Crevasses and rifts are a precursor to ice shelf calving and retreat (Rydt et al., 2019; Cheng et al., 2021), and heavily damaged ice shelves can be vulnerable to collapse when combined with other (environmental) factors, such as hydro-fracturing (Banwell et al., 2013; Lai et al., 2020; Robel and Banwell, 2019), unpinning or back-stress triggered failure (Miles et al., 2021; Benn et al., 2022), sea ice or mélange removal (Arthur et al., 2021; Banwell et al., 2019) and changes in sea surface slope (Christie et al., 2022; Massom et al., 2018).

Despite the critical role of damage in ice shelf instability and retreat, large-scale spatiotemporal assessments of the evolving distribution of fractures in the (recent) past are scarce (Lai et al., 2020; Pang et al., 2023; Surawy-Stepney et al., 2023b). How widespread ice shelf weakening occurs across the Antarctic therefore remains to be diagnosed.

The scarcity of damage observations and damage change assessments has, so far, primarily been due to a lack of available methods that can be applied on large spatial and temporal scales. This has recently been remedied by the advent of machine learning approaches (e.g., Lai et al., 2020; Pang et al., 2023; Surawy-Stepney et al., 2023b) as well as improved image processing techniques, such as the Normalised Radon transform Detection method (NeRD) method (Chapter 2: Izeboud and Lhermitte, 2023).

In this study, we use the NeRD method to identify and quantify damage on satellite imagery from both the RADARSAT RAMP mosaic of 1997 (100 m resolution) and Sentinel-1 Synthetic Aperture Radar (SAR, 40 m) between 2015 to 2021 (Section 3.2 and 3.3). We present the first multi-decadal (24-year) analysis of damage changes on ice shelves across Antarctica (Section 3.4.2), complementing recently produced short-term damage change products of (Surawy-Stepney et al., 2023b) and (Pang et al., 2023). These assessments are used to analyse the link between damage development and ice shelf calving or retreat (Section 3.4.3).

3.2 Data for damage detection

We employ data from two distinct sources to create damage maps on Antarctic ice shelves: the image mosaic of the Radarsat-1 Antarctic Mapping Project (RAMP) of 1997 (Jezek et al., 1998) and Sentinel-1 Synthetic Aperture Radar (SAR) images for the years 2015-2021. We masked all data outside of the ice shelf bounds: grounded ice as well as ocean areas.

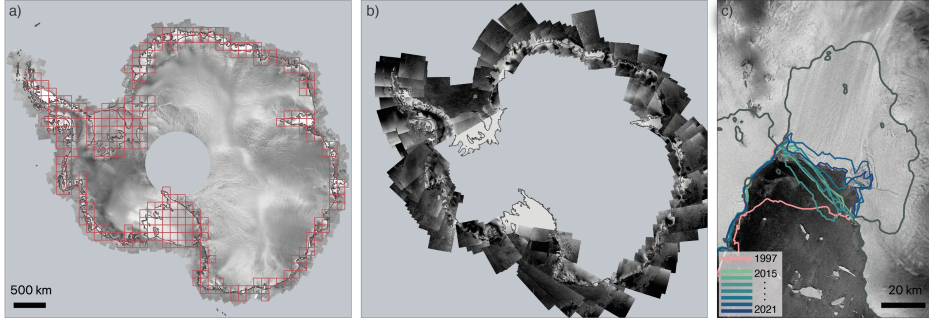


Figure 3.1: **Overview of used datasets to produce damage assessments.** **a)** RAMP mosaic from 1997 (Jezek et al., 1998), processed with NeRD only for data within the red tiles that cover all ice shelves. **b)** Data coverage of Sentinel-1 EW ascending orbit images in one assessment year (2021), showing data gaps on the Filchner-Ronne, Ross and Amery Ice Shelves. **c)** example of annual calving front positions at the Pine Island Glacier, adapted from Greene et al. (2022) with manual corrections to fit the used Sentinel-1 images. Grounding line from (Rignot et al., 2016) is added to each plot.

3.2.1 Satellite observations

RAMP Mosaic

The RAMP Mosaic is composed from SAR observations obtained by the Antarctic Mapping Mission 1 (AMM-1) acquired between September and November 1997, using HH polarisation with a C-band frequency of 5.3 GHz (Jezek et al., 1998). The mosaic was constructed with a spatial resolution of 100 meters and is publicly available (<https://asf.alaska.edu/data-sets/derived-data-sets/ramp/ramp-get-ramp-data/>). We only processed data covering Antarctic ice shelves, selected by tiles as shown in Figure 3.1.

Sentinel-1

For the period spanning 2015 to 2021, we obtained the Sentinel-1 SAR Ground Range Detected images, focusing on overpasses occurring in September through November of each year to mirror the RAMP acquisition season. We similarly use the HH polarisation band with a C-band frequency of 5.4 GHz. More specifically, we have selected images from ascending orbits with Extra Wide (EW) swath instrument mode, with a spatial resolution of 40 meters. The SAR images were not filtered to remove speckle noise, as a noise removal step is already included in the NeRD method. To reduce data volume and optimise processing efficiency, while keeping maximum spatial coverage, we have chosen the first acquisition from each unique relative Sentinel-1 orbit (property *'relativeOrbit-Number_start'*) each year. In total, our dataset comprises between 123 and 212 images per year, culminating in 1638 processed Sentinel-1 images overall. The images are open-source available and were acquired through the Google Earth Engine (GEE) (Gorelick et al., 2017), for which the code has been included in the repository accompanying this manuscript. A complete list of the processed image id's is made available as well.

Addressing Data Gaps

The Sentinel-1 EW data coverage over Antarctica is constrained to coastal areas (Husman et al., 2023). This limitation results in data gaps over the inland sections of the Amery, Filchner-Ronne, and Ross Ice Shelves (see Figure 3.1). To maintain temporal consistency in our assessments, we have masked these no-data areas from the RAMP dataset when computing spatially aggregated values (Figure C.2). Furthermore, some regions have inconsistent annual coverage (e.g., part of Getz Ice Shelf and a few ice shelves in Wilkes land). These data gaps are also masked for the computation of all annual spatially aggregated values, but not from the shown annual damage maps in Figure C.2.

3.2.2 Annual Ice Shelf Masks

We used the MEaSUREs (Rignot et al., 2016) grounding line to remove grounded areas, and kept this static over the study period. Annual ice front positions were obtained from Greene et al. (2022) and manually adjusted to match the ice fronts in our Sentinel-1 dataset, which was obtained roughly half a year later for each year than data used by Greene et al. (2022). An example of the ice front positions is included in Figure 3.1c.

3.3 Methods

3.3.1 Damage detection with NeRD algorithm

NeRD is a line detection algorithm that is capable of processing multi-source remote sensing imagery at varying spatial resolutions, making it an invaluable tool to process both RAMP and Sentinel-1 data sets. NeRD excels in detecting a wide range of morphological damage expressions, encompassing surface crevasses, large rifts, and heavily damaged areas with complex or chaotic fracture patterns. NeRD identifies a continuous damage signal based on the gray-scale contrast of linear features applied to small $N \times N$ pixel kernels of the (satellite) image. Each kernel yields a single damage signal value (\hat{D}) within the range of 0 to 0.5 (unit-less).

To ensure consistency in resolution for our long-term damage change assessment, the RAMP and Sentinel-1 images were processed with NeRD using a different kernel size. The RAMP mosaic, with an original resolution of 100 m, underwent processing with 10x10 pixel kernels (without overlap), yielding 1000 m for the produced damage maps. The Sentinel-1 data of 40 m resolution was processed with 25x25 pixel kernel size to attain the same 1000 m output resolution. Sentinel-1 data was also processed with 10x10 pixel kernel sizes to produce high resolution damage maps (400 m)¹.

NeRD accounts for detection differences between sensors using a sensor and resolution specific noise filtering step. For each sensor/resolution combination, we calculated a signal noise threshold following the methodology outlined by (Izeboud and Lhermitte, 2023). This threshold (τ) was determined as the 95th percentile signal value of the NeRD signal over an undamaged area (manually defined), yielding: $\tau_{\text{RAMP};100\text{m};10\text{px}} = 0.016$;

¹These damage maps are not used for the analyses in this chapter, but included as output of this thesis.

$\tau_{S1;40m:25px} = 0.041$; $\tau_{S1;40m:10px} = 0.053$; The noise threshold is subtracted from the NeRD signal, removing sensor and resolution induced biases and so ensuring the reliability and consistency of the damage assessment across different data sets.

While the NeRD method effectively minimizes disparities in detected damage signal values between different sensors through this noise threshold, some variations may persist due to two key factors: i) changes in surface conditions that influence the SAR backscatter signal and ii) differing levels of sensitivity to the spatial variability of surface conditions. This sensitivity was tested (see Supplementary Material, Appendix C) but its effect is an order of magnitude smaller than the standard deviation of the signal itself, and can be considered insignificant. This instills confidence in the comparability of RAMP and Sentinel-1 damage assessments.

3.3.2 Damage quantification

The damage assessments obtained from overlapping Sentinel-1 images were consolidated into a single damage assessment per year by determining the median damage signal from overlapping pixels. The number of overlapping images varied regionally, ranging from 1 to 12-25 images, depending on the year, with a median of four overlapping images used for each pixel.

Spatially integrated quantifications of damage and damage change were conducted based on the detected damage area. The damage signal was discretized into a binary classification, ‘damage’ ($\hat{D} > 0$) or ‘no damage’ ($\hat{D} = 0$), for each pixel. The sum of pixels (each measuring 1 by 1 km²) for both categories was then calculated per ice shelf. The damage values were integrated per ice shelf and sector using the annual updated ice shelf boundaries by Greene et al. (2022) and sectors defined by Fürst et al. (2016), respectively.

3.3.3 Damage observation uncertainty

The NeRD method, while effective, has inherent limitations. It operates by detecting linear features based on gray-scale contrast, making it unable to distinguish various sources of contrast in the image, such as rock outcrops, terrain shadow, or sea ice edges, from ice fractures. These features are filtered from our output by clipping the produced damage map to ice shelf areas, which effectively removes rock outcrops and steeply sloped terrains. We made an extensive effort to determine an ice front position aligned to the used satellite data to mask ocean areas, ensuring that sea ice features were removed completely. We consider these efforts sufficient to remove falsely detected damage features from the results.

Secondly, the algorithm returns a single value per processing kernel, rather than resolving the shapes of individual fractures. This limits how well crevasse opening is resolved. Instead, we have focused on changes in damage area extent by analysing how many kernels yield a positive damage signal $\hat{D} > 0$. As a result, the reported damage changes between 1997 and 2021 consider mainly new damage features or horizontally propagating rifts rather than the deepening or opening of existing fractures. Moreover, the reported damage areas (in km²) represent the number of output pixels that contain fractures (i.e. weakened areas), not the explicit extent of opened fractures (such as Pang et al., 2023)).

3.4 Results

3.4.1 Antarctic wide damage

Eight Antarctic-wide damage maps are produced, for 1997 and every year from 2015 to 2021. These maps can be explored in detail online at the Google Earth Engine (GEE), <https://code.earthengine.google.com/1861eb3fdf5ad2990bfb58aaf17eb475>. Figure 3.2 shows a few maps of damage for these years, Figure 3.3 presents annual assessments on Antarctic scale and Figure 3.4 shows the long-term differences between observed damage on selected ice shelves. In Appendix D, more damage maps are included of selected regions and ice shelves.

From the produced maps, multiple variations of damage patterns on ice shelves are detected. For some ice shelves, damage is concentrated in shear zones (e.g., Pine Island, Crosson and Fimbul ice shelves; Scott glacier next to Shackleton ice shelf), while others exhibit fractures mostly perpendicular to the ice flow near the ice front (e.g., Getz, Dotson, Cook and Jelbart ice shelves) or distributed across the entire ice tongue (e.g., Brunt, Larsen D, Ninnis, Drygalski and Shackleton ice shelves). Intact ice shelves with minimal damage are identified (e.g., Abbot, Cosgrove, Bach, and Rennick ice shelves), albeit rare.

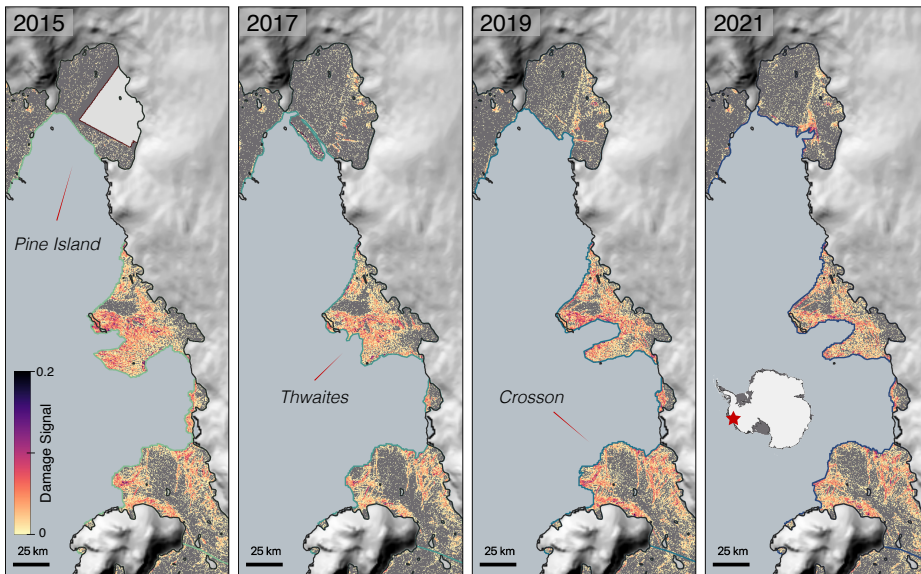


Figure 3.2: Damage maps of ice shelves in Amundsen Sea Embayment for select years. Detected damage by NeRD on Sentinel-1 SAR imagery obtained in September-October-November each year between 2015-2021. The damage maps have 400 m spatial resolution. Data is clipped to ice shelf area as obtained from adjusted ice front positions (Greene et al., 2022) and static grounding line (Rignot et al., 2016). Uniform gray areas indicate no-data coverage for that year. The grounded ice is visualised with a shaded DEM (Matsuoka et al., 2018).

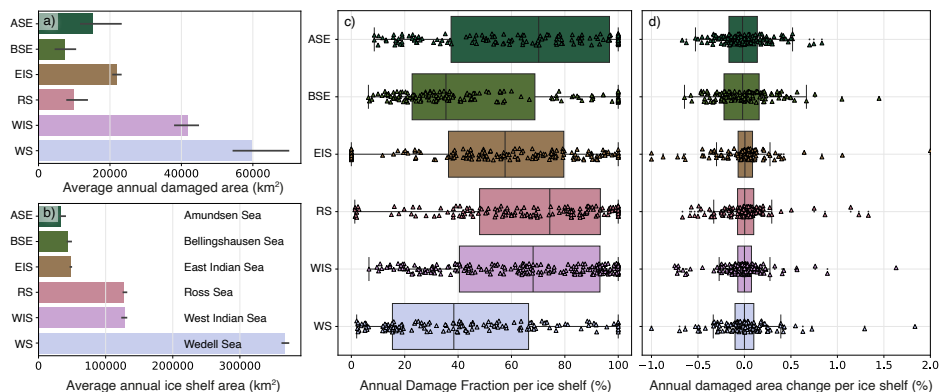


Figure 3.3: **Aggregated damage values per sector.** (a) Total damaged area extent and (b) total ice shelf area extent per sector, average of all years in the assessed period (1997; 2015-2021) with errorbars showing the min/max range between years. (c) Damaged area to ice shelf area fraction (%) calculated per ice shelf for each year, grouped per sector. (d) Percent change of damaged area per ice shelf each year, grouped per sector. See Figure 3.4 for sector bounds.

In 2021 the extent of damaged area as detected by NeRD is approximately 156600 km², roughly 20% of the total ice shelf area of Antarctica. Note that this value describes the frequency at which a 1x1 km² pixel contains a fracture feature, rather than the exact area of fractures. In the assessed time period, the damaged area ranges between 140500 to 169800 km² (respectively 19% and 22% of ice shelf area). Most damage is located in the Wedell and West Indian Sea Sectors (Figure 3.3a), which are also the sectors with the largest ice shelf area (Figure 3.3b). Vulnerable ice shelves with high ratios of damage area to ice shelf area (damage fraction) are most frequently located in the Amundsen, Ross, West Indian and East Indian Sea sectors (Figure 3.3c). The Ross and East Indian Sea sectors contain many small ice shelves, where a high damage fraction is easily obtained. The Amundsen and West Indian sectors host more moderate to large ice shelves and, consequently, a high damage fraction indicates vulnerable ice shelves as a result of large damaged areas. On the large ice shelves Filchner, Ronne and Ross, the ratio of damaged area to undamaged ice shelf area is much lower, explaining the overall small relative area of damage in the Wedell and Ross Sea Sectors (Figure 3.4i).

3.4.2 Observations of damage change

Our observations reveal a noteworthy 7.8% Antarctic-wide decline in damaged ice shelf area of 13200 km² from 1997 to 2021 (Figure 3.4), detected on 81 ice shelves. Concurrently, there is a decrease in the overall ice shelf area by 19200 km², accounting for a 2.5% reduction during the same period (detected on 69 ice shelves). The general decline in damaged area is evident in four out of six defined sectors, with the most significant reductions observed in the Amundsen and Bellingshausen Sea Embayment sectors experiencing decreases of 1440 km² (39.0%) and 500 km² (33.2%), with losses in ice shelf area

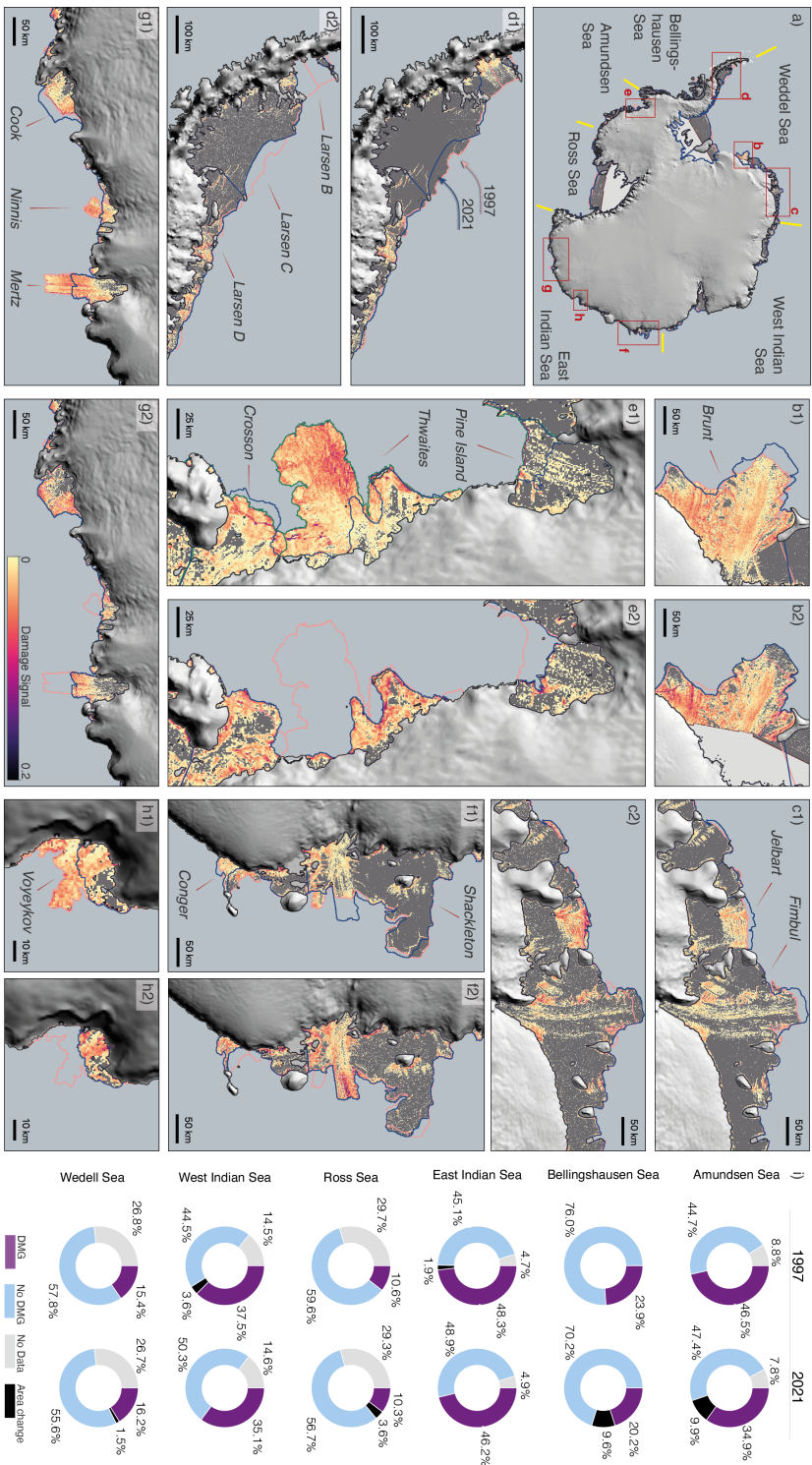


Figure 3.4: **Long-term damage change between 1997 and 2021.** (a) pan-Antarctic damage in 2021 and sectors bounds over which values are aggregated. Panels (b-h) show damage observations for selected ice shelves in 1997 (b1-h1; left panels) and 2021 (b2-h2; right panels). (i) Pie-charts quantifying damage and ice shelf area changes per sector: each pie-chart shows the partition of damaged area (purple) versus non-damaged area (light blue) and no-data (light gray). The black pie-wedge represents the area difference in either 1997 or 2021 (e.g., a smaller ice shelf in 2021 with respect to 1997 depicts the calved area in the 2021 pie-chart). Ice shelf fronts adapted from Greene et al. (2022) are displayed in pink (1997) and blue (2021). The grounded ice is visualised with a shaded Antarctic DEM (Matsuoka et al., 2018).

of 1200 km² (19.0%) and 830 km² (10.8%), respectively. In contrast, the Weddell Sea and East Indian Sea Sector display a respective 3.6% and 4.5% increase in damaged area, while the ice shelf area decreased by 1.8% and 2.3%, respectively.

These findings show that specifically highly damaged areas on ice shelves have calved, given that the relative reduction in damaged area surpasses the relative reduction in the overall ice shelf area. This confirms that damage acts as a precursor to calving (Benn et al., 2022; Arthur et al., 2021), in line with the findings of Pang et al. (2023): between 2004 and 2014, they reported a ~ 4% reduction of pan-Antarctic surface fracture extent, attributing it to surface fracture loss within 20 km of the ice front.

The panels in Figure 3.4 provide examples of heavily damaged areas in 1997 that have calved by 2021, such as the Thwaites Ice Tongue (panel e) and the Mertz, Ninnis, and Voyeykov Ice Shelves (panels g, h). In contrast, we also identify a few ice shelves, such as Jelbart, Shackleton and Cook (panels c, f, g), that exhibit area expansion alongside an increase in damaged area, indicating a potential for upcoming calving events. Lastly, we recognize a few ice shelves with limited changes in damage patterns despite ice shelf area increases, such as Brunt and Fimbul (Figure 3.4 panels b, c).

3.4.3 Damage development & ice shelf retreat

Since the long-term damage change analysis (Figure 3.4) suggests that highly damaged areas are removed during calving events, we incorporate annual damage change assessments from 2015 to 2021, based on Sentinel-1 data covering all ice shelves, to validate this relationship from short-term observations.

The annual satellite observations of damage change reveal a strong positive correlation ($r = 0.84$, $p < 0.01$) with annual changes in total ice shelf area (Figure 3.5a). This underscores the cyclic nature of damage development on ice shelves (illustrated in Figure 3.6a and b): damage accumulates and eventually leads to calving (area reduction), which removes the damaged areas. Subsequently, the remaining ice shelf gradually advances and accrues new damage. Figure 3.5a also displays a number of instances with area changes close to 0% while damage increases, indicating the weakening of these ice shelves.

While the long-term assessment reveals a total loss of damaged area between 1997 and 2021, the annual assessments unveil fluctuations through the years. The minimum damaged area extent occurred in 2017 (−17.3% w.r.t. 1997), rebounding by 2021 (+11.5% w.r.t. 2017, Figure 3.5b). The fraction of damaged area to ice shelf area signifies the relatively weakened state of the ice shelves, which fluctuates with the cyclic development and reduction of damaged areas (22.2% in 1997, minimum of 18.9% in 2017, and 21.0% in 2021). This fluctuation is widespread across all ice shelves, with 87 out of 124 (70%) exhibiting a decrease in damage fraction from 1997 to 2017, and 98 ice shelves (79%) displaying an increase from 2017 to 2021 (with 78 ice shelves belonging to the former group).

The damage cycle is exemplified for select ice shelves in Figure 3.5c-g. On Crosson, Larsen C, and Thwaites ice shelves, both the damaged area and damage fraction exhibit fluctuations through the years. Noteworthy calving events, such as the calving of iceberg A-68 (Larour et al., 2021) on Larsen C Ice Shelf in July 2017 are marked by an increase of damaged area and damage fraction (i.e., ice shelf weakening) before the event, followed by a

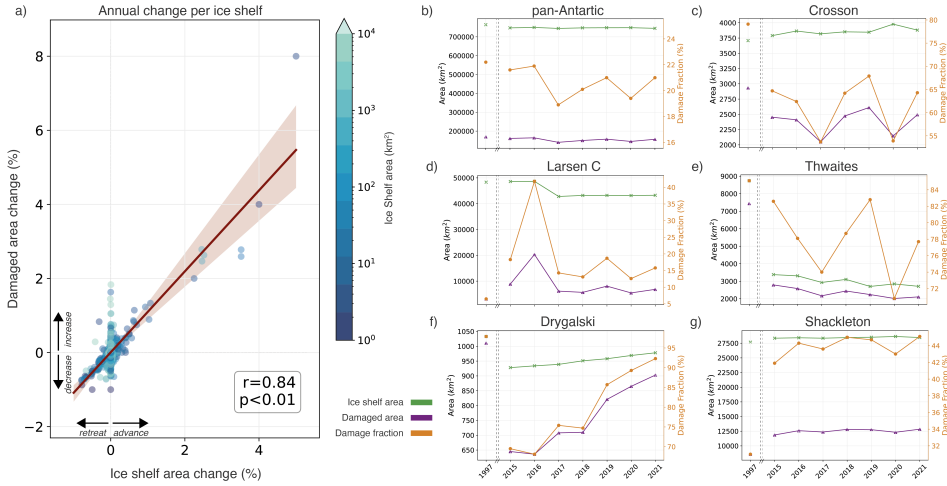


Figure 3.5: Correlation between damaged area changes and ice shelf area changes. (a) Correlation between area changes (%) for all ice shelves, assessments between 1997 and every year from 2015 to 2021. Colors indicate the size of the ice shelf. (b) Time series for pan-Antarctic and (c-g) selected ice shelves showing total annual damaged (purple) and ice shelf (green) area on the left y-axis and the fraction of damaged area (orange) on the right y-axis.

decrease in both after the event. Additionally, ice shelves like Drygalski and Shackleton exhibit a consistent expansion of ice shelf area and damaged area between 2015-2021, indicating an overall weakening over time and a heightened likelihood to future calving.

These examples that consider the damage fraction underscore that ice shelves are often in a weakened state prior to calving. Weakened ice shelf states have been connected to loss of buttressing and ice shelf speed-up (Rydt et al., 2021; Lhermitte et al., 2020; Miles et al., 2021; Surawy-Stepney et al., 2023a), further enhancing damage development and weakening the ice shelf over time (illustrated in Figure 3.6c and d). Our findings capture this weakening process for the first time.

3.5 Discussion

The annual damage maps presented in this chapter provide insight in the extent and variability of damage on pan-Antarctic ice shelves. We focus on the overall damaged area extent per ice shelf, rather than studying various detected patterns of damage, in order to make Antarctic wide aggregations. This approach disregards the different drivers of fracture opening and rift propagation (e.g., tidal forcing (Hui et al., 2016), mode I-III opening fractures (Colgan et al., 2016; Bassis et al., 2023), basal melt (McGrath et al., 2012a; Alley et al., 2019)) in favour of providing a general indication of ice shelf weakening through the

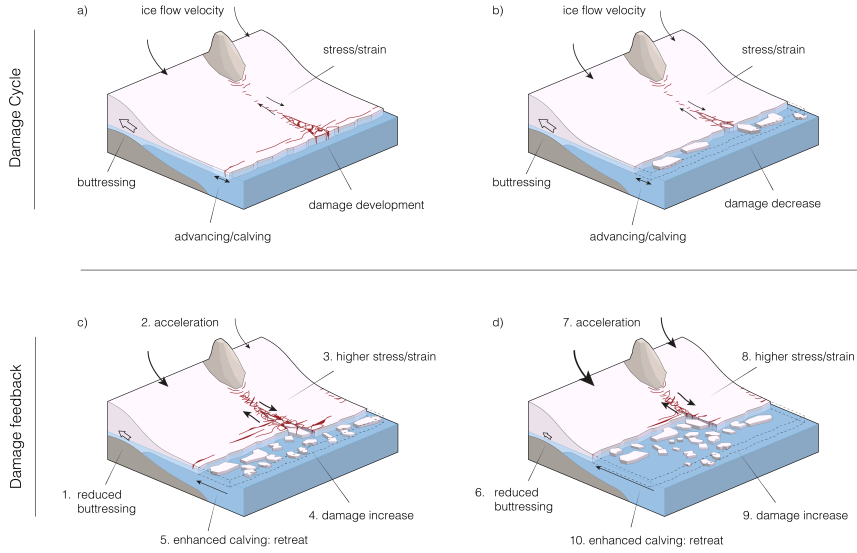


Figure 3.6: Damage impact on ice shelf weakening and retreat. Schematic figure showing the advance and retreat of an ice shelf during a damage cycle (**a** and **b**) versus enhanced retreat as result of the damage feedback (**c** and **d**). The depicted ice shelf states of panel (a) and (b) are recurring. Panel c and d describe that, once a loss of buttressing occurs (1), a positive feedback is activated that accelerates ice flow (2), enhances internal strain rates (3) which, in turn, enhances damage (4) and eventually enhances calving (5). This further reduces the buttressing effect, reaching panel (d, nr. 6 and onwards), with no (or very slow) recovery to the original ice shelf extent. Illustration by I. van der Heide.

years. We made binary classifications of the detected damage signal before aggregation to simplify large-scale interpretation of the results. Hence, the analysis of damage change focuses on newly damaged areas rather than the change of existing features. Using the continuous signal in future studies could provide more insight on the development of existing damaged areas. Furthermore, we neither study the advection of damaged areas downstream of their initiation area. Using a Lagrangian (displacing damage maps using velocity fields) would help gain insights in the location of active damage development areas. However, in our current damage product grounded areas were removed due to large uncertainties of the NeRD method on steeply sloped terrain. As fractures and rifts often originate near the grounding line or downstream of pinning points (Emet et al., 2018; Rydt et al., 2018; Bassis et al., 2023), the damage product does not provide enough information to properly assess damage initiation.

Our damage change assessment indicates a positive correlation between changes in damaged areas and ice shelf areas, and that calving removes compromised ice shelf regions, which is in line with previous studies of Emet et al. (2018); Pang et al. (2023). We also find that ice shelf weakening, represented by increased damage fraction, occurs before re-

treat. The damage fraction, however, is a relative measure and so its comparison between ice shelves is difficult. We therefore focused on the evolution of the damage fraction in time and show fluctuations of ice shelf weakening that are prevalent on the majority of ice shelves. Even though a long term ice shelf retreat and reduction in damaged area is detected between 1997 and 2021, our results suggest that the majority of ice shelves is in becoming more vulnerable in the past three years of the observed period. In accordance with Andreassen et al. (2023), our results underscore the importance of using time-variable observations of damage and calving to measure change.

These assessments of ice shelf weakening can provide insights in the vulnerability and likelihood of ice shelves for retreat, although the timing of ice shelf calving is more complex and depends on multiple environmental factors (Banwell et al., 2013; Lipovsky, 2018; Wille et al., 2022). Nevertheless, Bassis et al. (2023) conclude that ice shelves are sometimes vulnerable to short-term collapse, but that this vulnerability needs to be preconditioned. Our results help in identifying ice shelves that are vulnerable, effectively focusing future studies into the processes governing ice shelf stability. Lastly, ice shelf retreat has been associated with loss of buttressing and ice shelf speed-up (Rydt et al., 2021). More specifically, Davison et al. (2023) have shown a positive correlation between cumulative retreat and increased grounding line discharge at 48 ice shelves between 1997 and 2021. Although a difference in sensitivity of ice shelves remains, this means that damage, leading to ice shelf retreat, can eventually lead to enhanced ice sheet mass loss.

3.6 Conclusion

This study provides a novel perspective on continent-wide changes in damaged areas across Antarctic ice shelves over an extended 24-year period from 1997 to 2021, supplemented by annual observations from 2015-2021. Our observations reveal a long-term reduction of damage on Antarctic ice shelves attributed to the calving of compromised ice shelf regions. Notably, a strong correlation between damaged area changes and ice shelf area changes over the last seven years underscores the link between damage-induced weakening and subsequent calving and ice shelf retreat. Increases in damaged area and damage fraction prior to calving suggest that ice shelves are in a weakened state before calving occurs. The cyclic development and decrease of damage between 1997 and 2021, alongside the observed increase in damage fraction across the majority of ice shelves since 2017, indicate a present and growing vulnerability to calving.



Chapter 4

Antarctic ice shelves vulnerable to damage in future climate warming

Together with Chapter 3, this chapter is based on: Izeboud, M., Lhermitte, S., de Roda Husman, S., Wouters, B. Antarctic ice shelves vulnerable to damage in future climate warming. *In review at Nature Climate Change, NCLIM-24010280-T, 2024*

Although the feedback of damage on ice shelf buttressing, ice flow and further damage development has been considered key for future ice shelf stability, damage processes remain challenging to include in ice sheet models. And, due to a lack of large spatiotemporal observations, ice sheet models have had limited opportunity to be calibrated and evaluated to observations. This leaves the impacts of damage on ice shelf weakening and Antarctic mass loss, in current and future scenarios, poorly understood.

*In continuation of Chapter 3, here we use machine learning to combine our produced damage maps to other (satellite) observations (Section 4.2, 4.3) and analyse **‘How is detected damage linked with mechanical weakening of ice shelves?’** The constructed relationship is used with ice sheet model data of the ISMIP-6 project as input to project damage changes for future climate scenarios (Section 4.4). With these results we investigate **‘What is the importance of damage on future ice shelf weakening and retreat?’***

4.1 Introduction

The potential instability of Antarctic ice shelves is a major uncertainty in current sea level rise projections, either due to short-term collapse or long-term weakening (Fox-Kemper et al., 2021; Robel et al., 2019). Understanding the processes that affect the weakening, retreat and instability of ice shelves is therefore essential (Bassis et al., 2023; Calvin et al., 2023). Damaged areas on an ice shelf, consisting of crevasses and/or rifts, are first indicators of its weakening (Borstad et al., 2012, 2017). This weakening reduces the ice shelf's ability to buttress the grounded ice, which leads to speedup of the ice flow and increases internal stress and strain rates (Miles et al., 2021; Gudmundsson et al., 2019; Arndt et al., 2018; Tinto and Bell, 2011). Higher strain rates, in turn, promote additional damage development, creating a feedback loop that increasingly weakens the ice shelf and enhances ice mass loss through increased discharge (Lhermitte et al., 2020; Surawy-Stepney et al., 2023a).

Despite the critical role of damage in ice shelf instability and retreat, it remains a challenging process to capture in ice sheet models. While progress has been made, damage processes remain inadequately integrated into realistic ice-sheet models, and are currently limited to study idealised scenarios (Krug et al., 2014; Sun et al., 2017; Benn et al., 2022). This issue, in part, is a result of the scarcity of large-scale spatiotemporal observations to constrain, calibrate and evaluate the models (Gerli et al., 2023b). As a result of these model limitations, we cannot yet quantify the impact of damage on ice shelf stability and mass loss, and have so far been unable to provide projections of ice shelf weakening for future emission scenarios.

In order to advance our understanding of ice shelf dynamics and improve the projected contribution of Antarctica to sea-level rise, it is crucial that we assess the effect of climate change on damage-induced weakening and retreat of ice shelves, which can potentially lead to instability and collapse. In this study, we use multi-year observations of damage changes on Antarctic ice shelves (Chapter 3) and machine learning to analyse the relationship between damage and ice dynamics from an observational perspective. By using projected changes of the ice dynamical parameters from ice sheet models in the Ice Sheet Model Intercomparison for CMIP6 (ISMIP-6) project (Seroussi et al., 2020) as input for the constructed relationship, we create projections of damage change under future climate scenarios.

4.2 Data for damage predictor

4.2.1 Feature selection

To discern the intricate connection between our identified damage signal from Sentinel-1 data spanning 2015 to 2021 and the fundamental underlying ice dynamical parameters, we employed a non-linear, multi-variable Random Forest (RF) regression model. Multiple features were selected to train the RF model. The feature selection process was carefully guided by the parameters' relevance (Emet et al., 2018) and their consistent availability across observational datasets (for training of the RF model) and model outputs in the

ISMIP-6 experiments (for application of the RF model). The selected key features for the regression are: ice thickness, ice velocity, multiple ice strain rate components, and temporal changes in both ice velocity and strain rates.

4.2.2 Observational data

For ice thickness, we employed REMA surface elevation mosaic at 8 m spatial resolution (Howat et al., 2019) as constant proxy for ice thickness for the period 2015-2021. As a rule of thumb, ice thickness is estimated to be approximately eight times the height above flotation. The REMA mosaic is available in the Google Earth engine (GEE) as asset 'UMN/PGC/REMA/V1_1/8m'. Velocity and strain rate features were calculated from horizontal velocity components. Observational velocity data were obtained from the ITS_LIVE campaign at 240 meter spatial resolution available for the years 2015-2018 (Gardner et al., 2019) and at 120 meter resolution for 2019-2021 (currently working using beta version, courtesy of Alex Gardner, pending update of final v2 mosaics). Both the velocity data sets and the REMA mosaic were re-sampled to the same grid as the damage maps (1 km) using spatial averaging. Temporal velocity and strain changes were calculated as annual differences and subjected to smoothing using a three-year trailing maximum window. The strain components, encompassing maximum and minimum principal strain rates, effective strain rate, longitudinal-, transverse-, and shear strain rates, were calculated as nominal strains. To accommodate both large-scale averages and small-scale patterns, these calculations were performed considering different length scales (1, 5, and 15 pixels) (Alley et al., 2018). For the relevant equations we refer to Equation 1-4 and 7 in Alley et al. (2018).

4.2.3 ISMIP-6 ice sheet model data

To generate future projections of damage, we applied the trained RF model to model outputs of the ISMIP-6 experiments. Correspondingly to the observational data used for training the RF model, we utilized modelled surface velocity and surface elevation data (Seroussi et al., 2020).

Many ice sheet models that participated in the ISMIP-6 project have model grid resolutions exceeding 10 km, a relatively low spatial variability compared to the observational data sets. Recognising that damage is often localised in specific regions of the ice shelves (e.g., near the ice front, after a pinning point, or in the shear zone (Banwell et al., 2017; Borstad et al., 2017; Miles et al., 2021, Chapter 3,)), the RF regression model was developed at the highest possible spatial resolution. We therefore selectively chose ice sheet models from the ISMIP-6 project with a spatial resolution of 8 kilometers or finer close to the grounding line. This resulted in five selected ice sheet models: the Potsdam Parallel Ice Sheet Model (PISM) (Winkelmann et al., 2011), the SIMulation COde for POLythermal Ice Sheets (SICOPOLIS) (Greve et al., 2020), MPAS-Albany Land Ice (MALI) model (Hoffman et al., 2018), the Ice Sheet System Model (ISSM) (Schlegel et al., 2018) and the Community Ice Sheet Model (CISM) (Lipscomb et al., 2021).

4.2.4 Spatial resolution

All ISMIP-6 model datasets were re-sampled to a regular 8 km grid to ensure standardised inputs for the RF model, using nearest neighbour interpolation. Concurrently, observational datasets were down-sampled to the same grid through averaging. During the down-sampling process of the damage observations, all pixels without observed damage (i.e., $D = 0$) were treated as NaN data. These re-sampling and down-sampling steps were executed prior to strain rate calculations.

4.3 Random Forest model development

We used Random Forest regression to establish a connection between our (continuous) damage signal observations and key features of ice dynamics. The choice of Random Forest regression was driven by its capabilities in handling multi-dimensional, non-linear regression challenges (Nawar and Mouazen, 2017). Random Forest regression offers advantages over neural networks, particularly in its resilience to feature scaling discrepancies (Ahmad et al., 2017; Han et al., 2018; Roßbach, 2018), a vital feature for our work given the varied data distribution characteristics across our input data sources. To ensure robust and reliable model development, we maintained the independence of our training, validation, and testing datasets, both in spatial and temporal terms.

4.3.1 Training, testing and validation datasets

To ensure temporal independence, we designated the years 2015 to 2018 as the training dataset and 2021 as the temporal test dataset. We excluded 2019 and 2020 from the test set due to the lack of complete independence, given that two of our features involved temporal averages calculated over three-year trailing windows.

Spatial independence was a critical consideration in the development of the RF model, due to the spatial correlation between neighbouring pixels (Ploton et al., 2020; Roberts et al., 2017). Although the model was constructed to predict values at the pixel level, pixels within the same ice shelf can show interdependence. To address this, we organized pixels from the same ice shelf into “spatial groups”, treating them as independent entities with respect to pixels from other ice shelves. We leveraged the group-k-Fold cross-validation technique to partition the data into training, validation, and testing subsets, while ensuring that these subsets maintained similar distributions of target data. Initially, the grouped data was randomly split into a train+validation and test set comprising 103/18 ice shelves (86/14% or 36858/6143 pixel samples). The ice shelves designated for the test set were kept separately and included Abbot_3, Amery, Bach, Deakin, Dibble, Mendelssohn, Moubray, Pine Island, Publications, Rennick, Ross_East, Sandford, Shackleton, Stange, Withrow, Whittle, and Wordie (names from (Mouginot et al., 2017b)). Subsequently, the training + validation set was further partitioned randomly into training and validation folds, repeated five times. Each fold consisted between 82/21 and 84/19 ice shelves for train/validation purposes, respectively (80/20% or 29486/7372 samples)

4.3.2 Hyperparameter tuning

We optimized the RF model through a two-step hyperparameter tuning process. In the initial step, we trained the RF model on all features and multiple strain rate length scales, using a broad hyperparameter grid. Of this grid, twenty candidate models were evaluated to each of the five data folds using random search cross-validation. The best hyperparameter combination was chosen based on the lowest mean absolute error, and a RF model was re-fitted with this combination to use for feature importance analysis. This led to the choice of most relevant strain length-scale (1-pixel), excluding the other scales (5 and 15-pixel) as well as excluding the minimal principal strain (ϵ_2).

In the second step, we trained the RF model with the 9 selected features. Another round of random search cross-validation step was performed first to narrow down the search grid of hyperparameter values to a subset of promising values. Then, all hyperparameter combinations in this refined search grid were trained using `gridSearchCV` (fitting five folds for 96 candidates, totalling 480 fits) to obtain the best estimator, selected based on the lowest mean absolute error, which was 0.00979. This final estimator was re-fitted with all the training and validation data. The determined final hyperparameters were:

- bootstrap = False (rejected: True)
- max tree depth = 10 (rejected: 20, 30, 40, None)
- max features per node = 2 (rejected: 1, 4)
- minimum samples per leaf = 2 (rejected: 1, 4)
- minimum samples per split = 5 (rejected: 2, 10)
- number of estimators = 10 (rejected: 20, 30, 40, 50, 60, 70, 80).

This rigorous hyperparameter tuning strategy ensured the model's optimal performance for predicting damage changes.

4.3.3 Projected damage change ensembles

The trained RF model was applied to output of the five selected ice sheet models to generate damage projections. Model output obtained from five ISMIP-6 forcing experiments were used to get insights in the sensitivity of projected damage to different climate scenarios. Experiments 05 to 08 and the control experiment were selected due to their availability across all selected ice sheet models. The control experiment maintained constant climatic forcing from 2015 onward, while the other experiments introduced variations in atmospheric and oceanic forcing. More detailed descriptions about these experiments are available in Seroussi et al. (2020).

The RF model was applied to each ice sheet model's data for each experiment, and we calculated the predicted damage changes relative to each model's control experiment. This approach facilitated the analysis of relative changes within each model, thereby minimising biases resulting from different input feature data distributions among models.

The timeseries of projected damage changes was smoothed with a 5-year running mean. Model ensembles were created by averaging simulations from each experiment, providing an overview of the range of potential responses. Spatial maps and integrated assessments of damage change at the end of the century were generated by grouping the

ensembles (at $t=2100$) according to the Representative Concentration Pathway (RCP) scenarios, RCP2.6 and RCP8.5 (Nowicki et al., 2020). One experiment (exp.07) was part of the RCP2.6 group and the three others (exp.05, 06, and 08) were part of the RCP8.5 group. Integrated values per sector were calculated after masking all grounded ice.

It is crucial to note that the ISMIP-6 simulation experiments were designed to explore the diverse responses of ice sheet models to the RCP scenarios rather than representing a mean pathway. Consequently, the projected damage changes should be considered as indicative of the potential range (sensitivity and sign) of responses, rather than as a single predicted trajectory.

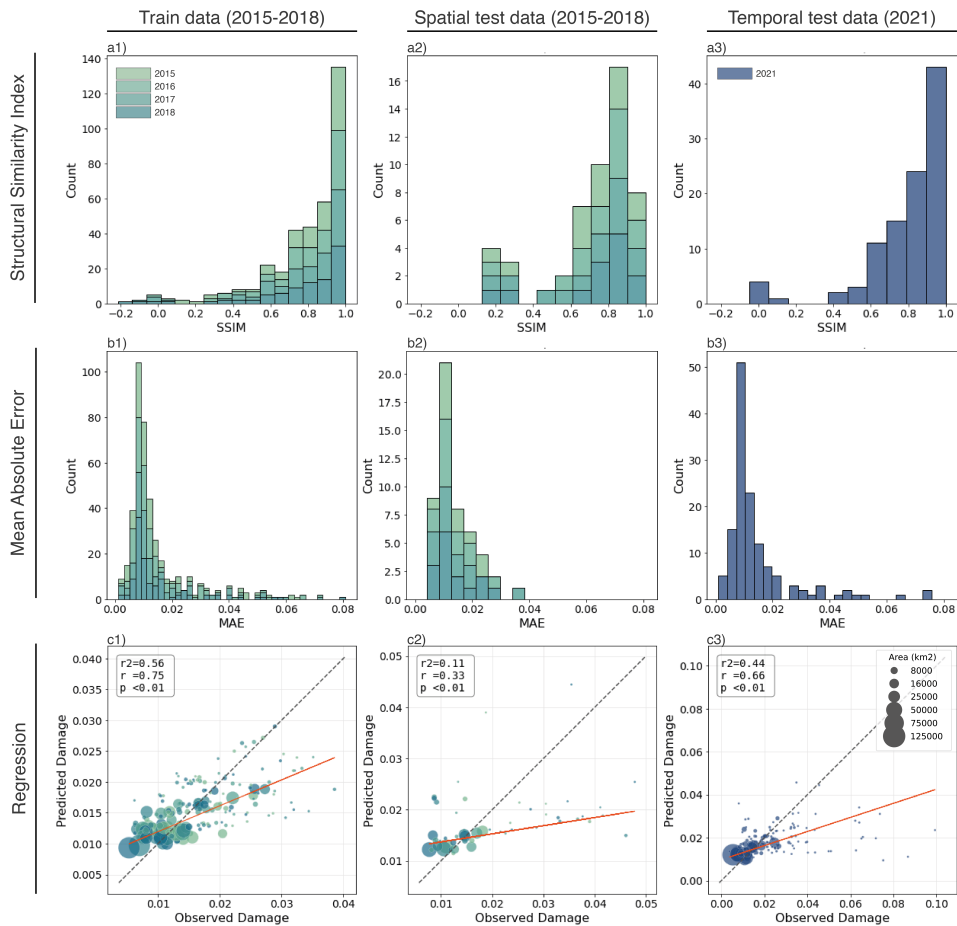


Figure 4.1: Evaluation of the Random Forest regression model for training (a1-c1) and testing dataset, split in the spatial test set (a2-c2) and temporal test set (a3-c3). a1-a3 show the Structural Similarity Index calculated for each ice shelf, b1-b3 the Mean Absolute Error calculated for each ice shelf, and c1-c3 the regression of observed versus predicted values, weighted for the area of each ice shelf.

4.4 Results

Random Forest model evaluation

For the RF model evaluation, we employ three key metrics: weighted coefficient of determination (R^2 , weighted to ice shelf area), Mean Absolute Error (MAE), and Structural Similarity Index (SSIM). Results are shown in 4.1. The weighted R^2 allows us to quantify the goodness of fit while accounting for ice shelf areas' size, providing more weight to larger ice shelves where the error variance is lower. This approach was appropriate as our training features did not perfectly align (per pixel) in space and time. The average MAE and SSIM per ice shelf allows for assessing the RF model's ability to predict damage patterns across the entire ice shelf, with SSIM particularly informative for evaluating the RF model's performance in capturing spatial variability.

The RF model demonstrates strong performance in the spatial and temporal evaluations, as indicated by high SSIM values (0.77 average on training dataset, 0.70 and 0.78 for spatial and temporal test sets, respectively) showing an aptitude for identifying regions with high damage. The average MAE was 0.017 (training), 0.015 (spatial test), and 0.017 (temporal test), aligning closely to the standard deviation of the damage signal itself (average $\hat{D} = 0.028 \pm 0.011$). The consistent performance across training and testing instills confidence in the RF model. Nevertheless, the model exhibits limitations in predicting high damage signal values, evident in the R^2 score evaluation where errors increase with higher damage values (4.1c; $R^2 = 0.56$ for training; $R^2 = 0.11$ for spatial test; $R^2 = 0.44$ for temporal test). Efforts were made to address this limitation through under-sampling and over-sampling techniques during the training process, but these approaches resulted in decreased RF model performance. From this, we conclude that the input features lack significant differences for the model to distinguish the (minority) 'high' damage signal values from 'medium' signal values. This seems reasonable, considering that the observed damage signal provides a 'strength of contrast' in the satellite image and is not directly related to physical ice parameters. Therefore, the difference between 'medium' to 'high' damage values might not be evident in the input features.

It should be emphasised that the primary goal of the RF model is not to provide absolute values of damage predictions. Therefore, the model's limited capability in predicting the largest damage values is deemed acceptable. The model's strength lies in assessing relative changes in observed damage due to ice dynamics, reliably capturing nuances and identifying spatial and temporal variations in damage intensity. This aligns with the overarching goal of evaluating the impact of ice dynamics on ice shelf stability.

4.4.1 Damage link to ice dynamics

The feature importance from the trained RF model shows that ice thickness and longitudinal strain rates have the most weight from all input features, of 20% and 15% respectively; but all features are meaningful, with lowest importance for the shear strain rate at 6%. Figure 4.2 provides insights into how these features are correlated, exemplified for the Amundsen and Bellingshausen Sea Sectors. These figures show how observed high damage signal values are positively correlated to high values of ice flow, ice flow change (i.e. acceleration) and high strain rate (for all components), while inversely correlated to ice

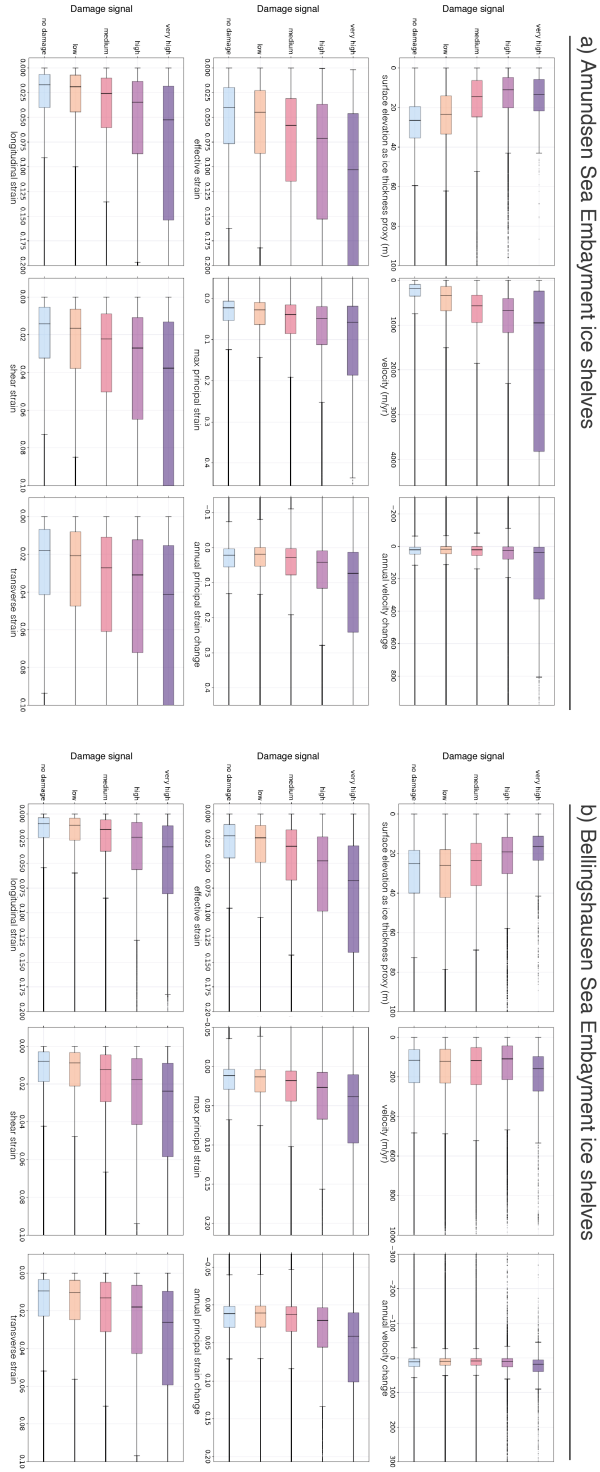


Figure 4.2: **Correlation of input features for RF model.** Pixel values are aggregated per sector, and shown here for ice shelves in the (a) Amundsen Sea and (b) Bellingshausen Sea Embayment. Damage signal values are binned by low to high signal values, to favor visualisation of the minority (high damage signal) class (low: $\hat{D} \in (0, 0.0125]$, medium: $\hat{D} \in (0.0125, 0.0625]$, high: $\hat{D} \in (0.0625, 0.5]$). See also Appendix Figure C.3.

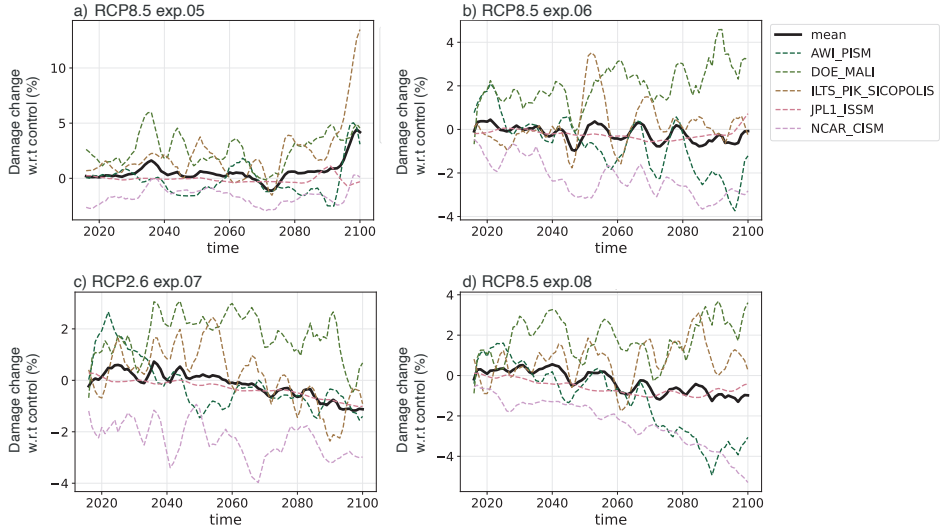


Figure 4.3: **Model ensembles of predicted damage values between 2015-2100**, shown for each climate forcing experiment, experiment 05 (a), 06 (b), 07 (c) and experiment 08 (d). Each panel shows predicted values of damage change (%) with respect to the control simulation of each model, with the ensemble mean in red, smoothed with a 5-year running mean.

thickness – indicating that (high) damage is more likely to be found at thinner parts of the ice shelf. These correlations are found on pan-Antarctic scale (Appendix Figure C.3) albeit not as strongly in all sectors.

The obtained RF model confirms that a feedback of damage-induced mechanical weakening to ice dynamics (as discussed by, for example, Lhermitte et al., 2020; Surawy-Stepney et al., 2023a) can be found based on observations, on pan-Antarctic scale.

4.4.2 Damage projected in future climate scenarios

We project the observations of damage changes to the future by providing the trained RF model with projected values of the ice dynamical parameters, obtained from the five selected ice sheet models for four climate forcing experiments and a control experiment. Figure 4.3 displays the timeseries of Antarctic average damage change relative to the control experiment for each model-experiment combination, including the ensemble mean. The figure shows a large range of responses between the ice sheet models. A relatively small ensemble mean trend is observed, but this intensifies near the end of the century, when climate forcing scenarios start to deviate more from the control conditions and differences between experiments get more pronounced (Calvin et al., 2023). For example, near 2100, differences between exp.05 (high emission scenario RCP8.5) and exp.07 (low emission scenario RCP2.6) are evident across the model range. In the control simulations, damage is projected to be relatively stable for all models (Appendix Figure C.4).

The ensemble mean projections at the end of the century, depicted in Figure 4.4, highlight the sensitivity of damage to future emission scenarios. Figure 4.4a indicates a slight decrease in damage for low emission scenarios associated with RCP2.6 of -0.8% (-2.9 to 0.7% model range) across the Antarctic domain by 2100, compared to the control simulations. Conversely, for the high emission pathway RCP8.5, we project an increase in damage by 3.2% (-5 to 14% model range, Figure 4.4b and c). The expected increase of damage under RCP8.5 coincides with increased ice shelf velocity (3%), thinning (8%), and increased strain rates (120 – 770% depending on the strain component; Figure 4.4d-i), reinforcing the notion of a general weakening of the ice shelves.

Distinct regional variations are observed (Figure 4.4c). The Amundsen Sea, West Indian, East Indian, and Ross Sea Sectors exhibit escalating damage levels. These increases result from a combination of ice flow acceleration, ice shelf thinning, and increased strain rates (Figure 4.4d-i). For example, strong increases of damage are predicted at the center of the Ross Ice Shelf in the RCP8.5 scenario primarily due to thinning and increased shear strain resulting from localised ice shelf acceleration and deceleration near the ice front. In contrast, the Weddell Sea and Bellingshausen Sea sectors display lower sensitivity, demonstrating fewer differences between a low or high climate forcing scenario.

4.5 Discussion

This chapter establishes a link between detected damage and key ice shelf parameters using a RF regression model and multiple observational datasets. While the RF effectively captures the spatial variability (high SSIM) and overall damaged state of ice shelves (low MAE), it struggles with predicting high damage signal values (low R2). Although its performance is sufficient for this study's purposes in capturing the qualitative response and sensitivity of damage development to future scenarios, the RF model can not accurately quantify the magnitude of impact of damage-induced weakening on ice shelf dynamics and mass loss. Presumably, the RF model could be improved by enhancements such as using a higher spatial resolution, adding more parameters like basal melt and thickness change or distances to ice front or grounding line, or by developing multiple RF models for distinct ice shelf groups to better capture various dynamic behaviour (similar to Emert et al., 2018). Although, rather than improving the RF model, we advocate to improve and calibrate the representation of damage processes in ice sheet models, which have the ability to isolate and quantify damage processes and calculate its contribution on Antarctic mass loss in past and future climate forcing scenarios.

By applying the RF model and projecting damage development to 2100, we discover that damage is expected to be enhanced for high emission scenarios relative to control conditions, while there is limited difference between the low emission scenario and control conditions. However, there is a wide range of projected damage changes across models, with a model range of 20% damage change relative to control for RCP8.5 scenarios and model range of < 5% for RCP2.6 scenario. The largest sources of uncertainty within the ISMIP6 project comes from the climate forcing, the ocean-induced melt rates, how these rates are calibrated on oceanic conditions outside of the ice shelf cavities, and the ice sheet dynamic response to these oceanic changes (Seroussi et al., 2020). In the selected

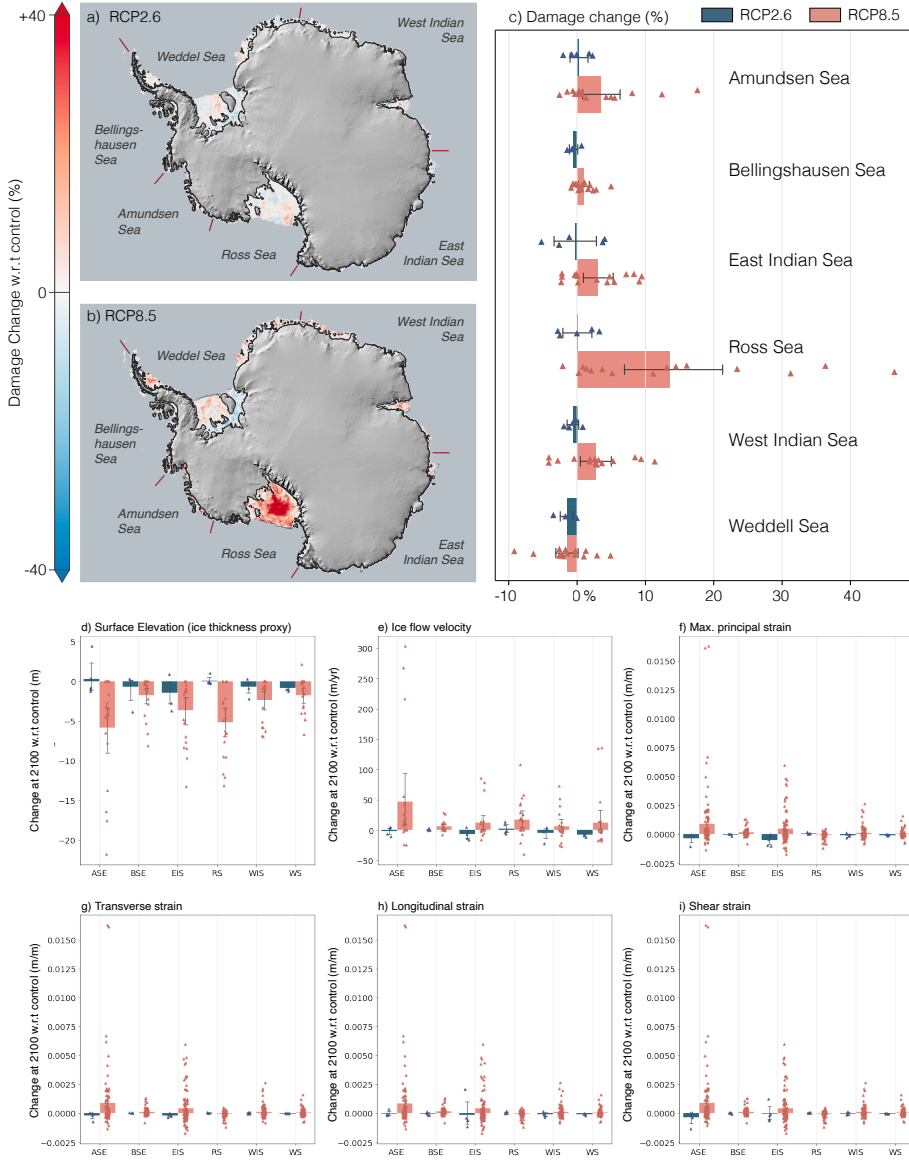


Figure 4.4: **Projections of damage change (%) by 2100.** Predicted damage values were obtained from the RF model using input data from five ice sheet models (PISM (Winkelmann et al., 2011), SICOPOLIS (Greve et al., 2020), MALI (Hoffman et al., 2018), ISSM (Schlegel et al., 2018) and CISM (Lipscomb et al., 2021)), and are calculated relative (%) to the control simulation of each model. Panel (a) and (b) show maps of the ensemble mean grouped for two climate forcing pathways, RCP2.6 and RCP8.5. Panel (c) shows the integrated values per sector, including data points for each model/experiment combination. Panels (d-i) show the projected changes of the input features by 2100 the same way.

experiments the melt parameterisation is the same (as described in Jourdain et al., 2020). Therefore, uncertainties in predicted damage values are mainly governed by uncertainties in the dynamic response of the ice shelves to this melting.

Lastly, significant regional variations in damage response are shown. In particular, the Ross ice shelf is expected to experience substantial damage increase under RCP8.5 scenarios. The potential intrusion of warm ocean waters into the Ross ice shelf cavity, leading to enhanced thinning, can explain this strong response (Figure 4.4d, Arzeno et al., 2014; Silvano et al., 2018; Siahaan et al., 2022; Seroussi et al., 2023). A similar concern of intruding warm ocean waters has been raised for the Filchner-Ronne Ice Shelf, but its occurrence before the end of this century is debated (Bull et al., 2021; Naughten et al., 2021; Siahaan et al., 2022). Our results do not suggest enhanced ice shelf weakening for Filchner-Ronne Ice Shelf under the used climatic and oceanic forcing, but this could change for new insights regarding the warm water intrusion. In the Amundsen Sea Embayment, ocean-driven melt has been controlling mass loss in the past and is expected to continue in the future (Dutrieux et al., 2014; Jourdain et al., 2020; Lipscomb et al., 2021; Naughten et al., 2023). The noted increase of damage development in a warmer climate (high emission scenario, RCP8.5) is therefore in line with expectations. More surprisingly, the West and East Indian Sea Sectors display similar sensitivities of damage development to the choice of emission scenario as the Amundsen Sea Embayment. East Antarctica (covering both sectors) is generally more stable in projections of future mass loss, largely because losses due to calving flux are offset by increased surface mass balance (Seroussi et al., 2020; Fox-Kemper et al., 2021). Past ice discharge in East Antarctica remained remarkably stable (between 2008 and 2015, Gardner et al., 2018), but, for example, Totten and Moscow University glaciers are thought to have similar sensitivity to additional basal melt and dynamic mass loss as Thwaites and Pine Island glaciers (Seroussi et al., 2023). So, the balance in East Antarctica might become more precarious if damage-induced weakening is taken into account, especially considering that both East and West Indian Sectors contain many ice shelves that are currently already highly damaged (Chapter 3, Figure 3.3).

4.6 Conclusion

For the first time, this study introduces projections of future damage changes by linking observed damage to key ice shelf parameters. Our projections highlight the sensitivity of future damage development (thus ice shelf weakening) to emission pathways. Under high emission scenarios, we anticipate intensified damage development, particularly in regions where ice shelves thin and accelerate (driven by increased ocean melt (Naughten et al., 2023)), coupled with substantial increases in strain rates. This underscores the intricate interplay between weakened ice shelves, accelerated flow, and damage development with notable vulnerabilities predicted in the Amundsen, East and West Indian and Ross Sea Sectors. While this is in line with observed modes of weakening at the Amundsen Sea Sector (Chapter 3, Surawy-Stepney et al., 2023a; Miles et al., 2021), the Ross Sea Sector currently displays relatively low amounts of weakening, and these projections indicate a potential shift to a more vulnerable regime.

The implications of observed and predicted damage development on ice shelves with respect to Antarctic mass loss are twofold. Firstly, we establish that weakened ice shelves coincide with acceleration and thinning, indicating a loss of buttressing, and express the expected weakening of ice shelves under (extremely) high climate warming scenarios. Not only does this future weakening then enhance the acceleration and damage development process which leads to more mass loss, the weakened ice shelves are also increasingly susceptible to retreat and/or collapse due to external forcing (Lai et al., 2020; Robel and Banwell, 2019; Benn et al., 2022; Banwell et al., 2019; Arthur et al., 2021; Massom et al., 2018; Donat-Magnin et al., 2021; Christie et al., 2022) - in which case their buttressing ability is diminished even further.

In conclusion, our study underscores the critical importance of including damage impacts in ice sheet models and future mass loss assessments. Damage leads to ice shelf loss as damage precedes calving events. Our projections indicate an increase in damage for future ice flow acceleration and thinning, suggesting that we may currently underestimate (the timing of) ice shelf retreat and Antarctic mass loss, contingent on the trajectory of future climate scenarios. Addressing this underestimation is vital for improving the representation of ice shelf stability and refining our understanding of Antarctica's contribution to sea level rise.



Chapter 5

Conclusions and perspectives

You can never know everything, and part of what you know is always wrong. Perhaps even the most important part. A portion of wisdom lies in knowing that. A portion of courage lies in going on anyways.

Robert Jordan, *The Wheel of Time*

We investigated the role of damage on ice shelf stability from an observational perspective. The focus has been on the spatial distribution and development of damage, as detected in satellite imagery, and considers both observations of the past and projections to future scenarios. The work can be split into three themes: (i) developing a method to make large spatiotemporal assessments of damage on Antarctic ice shelves, (ii) analysis of damage abundance and development as detected by the developed method on satellite data, and studying the link of damage to ice shelf weakening and retreat, (iii) providing estimates of future damage states, in order to gain more insights into the potential impact of damage on ice shelf stability.

This chapter summarizes the key finding of each theme, provides discussion and answers the research questions as formulated in Chapter 1. After that, the main findings are summarised and future research directions are discussed.

5.1 Automated damage detection method

In Chapter 2, a new method to detect damage features from satellite imagery is introduced: the NeRD detection method. The line-detection algorithm was successfully developed to generate robust crevasse signals and crevasse orientation across large spatial domains, and is uniquely suited to be applied to satellite imagery from different sources at varying spatial resolution. Another quality of NeRD is the detection of a continuous damage signal, enabling a differentiation between surface crevasses and rifts based on signal strength.

With respect to the research question, ***“How can an effective and robust method be devised to detect damage on Antarctic ice shelves from multi-source satellite imagery?”***, NeRD is considered a successful method to achieve the desired results. Nevertheless, it is recognized that alternative methods may be, and have been, devised that reach the same goal. Especially the efficacy of machine learning approaches, particularly Convolutional Neural Networks (CNN) for pattern detection, should be acknowledged.

Below, key characteristics of NeRD are highlighted in comparison to CNNs, to help future studies in choosing the best approach for their research objective.

NeRD excels in detecting damage features across various scales, moving beyond historical focuses on large rift features (e.g. Lai et al., 2020). This ability can, in principle, also be achieved by CNNs if they are developed to do so (e.g., Zhao et al., 2022), but this is not always straightforward (e.g., Surawy-Stepney et al., 2023b) and depends heavily on the detail and quality of training labels. Similarly, it should theoretically be possible to develop CNNs that can be applied on multi-source remote sensing data; but at present NeRD is the only available method that achieves this.

Despite its strengths, NeRD does not delineate individual fractures themselves. This impedes studying the life cycle of individual fractures. In this regard, CNNs are a more suitable approach. Vice versa, CNN-based approaches can mimic the spatial damage extent assessments of NeRD by constructing fracture density maps from their binary delineated fractures (such as Zhao et al., 2022; Surawy-Stepney et al., 2023b), and therefore cover more use cases than NeRD. Lastly, NeRD is a less computationally efficient method compared to trained machine learning models, which is a potential hindrance depending on the available computing power and scale of research. Then again, NeRD has the advance of being a transparent and understandable algorithm. This allows other researcher to more easily to pick up the method and further improve the algorithm to their needs.

5.2 Assessment of damage and damage change related to ice shelf retreat

In this section the inquiries of **“What is the current extent of damage across Antarctic ice shelves, and how has this damage evolved over the past decades?”** and **“To what extent is detected damage correlated to ice shelf retreat?”** are discussed.

In Chapter 3, newly produced, extensive, annual damage maps of Antarctic ice shelves are presented. The abundance of damage is evident on many ice shelves, including both fast flowing and accelerating ice shelves such as Pine Island, Thwaites and Crosson ice shelves in the Amundsen Sea Embayment, as well as other ice shelves across the perimeter of Antarctica. Vulnerable ice shelves with high ratios of damage to ice shelf area (damage fraction) are most frequently located in the Amundsen, Ross and West Indian sea. For some ice shelves, damage is concentrated in shear zones (e.g., Pine Island and Fimbul ice shelves and Scott ice shelves), while others exhibit fractures mostly perpendicular to the ice flow near the ice front (e.g., Getz, Dotson, Cook and Jelbart ice shelves) or distributed across the entire ice tongue (e.g., Brunt, Larsen D, Ninnis, Drygalski and Denman ice shelves). Intact ice shelves with minimal damage are identified (e.g., Abbot, Cosgrove, Bach, and Rennick ice shelves), albeit rare. In total, about 20% of the ice shelf area is, to some degree, damaged.

Long-term assessment of damage change unveil a widespread, long-term reduction of damage on Antarctic ice shelves (of 13200 km²; 7.8%), attributed to the calving of compromised regions. This chapter also sheds light on annual fluctuations in damage extent.

Ice shelves display an damage increase during phases of ice shelf advance and damage decrease with ice shelf area loss. Examples show the increase of damage prior to large calving events, signifying ice shelf weakening prior to retreat.

The chapter concludes that changes in damage extent are strongly and positively correlated to changes in ice shelf area, thereby confirming the link between damage-induced weakening, calving, and subsequent ice shelf retreat, based on these assessments. This correlation is observed on pan-Antarctic scale. By becoming increasingly damaged, ice shelves can become vulnerable for short-term collapse (Bassis et al., 2023). However, given the substantial variation among ice shelves in their damage extent and rates of damage development, further research is needed to translate detected damage and damage changes into predictions of ice shelf retreat or collapse. This will need to include other environmental factors that could trigger disintegration.

5.3 Impact of damage on ice shelf stability

Here the research questions **“How is detected damage linked with mechanical weakening of ice shelves?”** and **“What is the importance of damage on future ice shelf weakening and retreat?”** are considered.

Even though the effect of damage on ice rheology is simulated in continuum damage models, which can provide a connection between damage evolution and environmental forcing on ice shelves, the large scale evaluation and calibration of these models to observations has been limited thus far. Therefore, in Chapter 4, the relationship between damage and ice flow parameters is estimated based on Antarctic wide observational data. The used RF model was carefully trained and tested on independent spatial and temporal datasets, and was able to reproduce damage patterns reliably. The RF model reveals the link between damage, ice shelf thinning, ice shelf acceleration and high strain rates – in particular high effective strain and high longitudinal strain rates. The regression confirms that a feedback of damage-induced mechanical weakening to ice dynamics (as discussed by Lhermitte et al., 2020; Surawy-Stepney et al., 2023a) can be found on pan-Antarctic scale, based on observations. However, while accelerated ice flow by extension leads to enhanced mass loss of the Antarctic Ice Sheet, this study does not provide a quantitative assessments of how much mass loss can be attributed to damage. To better quantify the impact of damage on Antarctic mass loss, modelling approaches that include observationally constrained damage processes are required. This is further discussed in the next section.

Future damage development, indicative of ice shelf weakening, proves to be sensitive to future emission pathways, i.e. climate warming. For low emission pathways (RCP2.6) damage is predicted to be relatively stable or even decrease slightly (-0.8% w.r.t control simulation) across all sectors. For the high emission pathway (RCP8.5), an increase in damage (3.2% w.r.t. control simulation) is predicted, with strong regional differences (-5 to 14% model range). This indicates the benefit of climate mitigation policies with respect to Antarctic mass loss. The highest vulnerability to future damage changes is predicted in the Amundsen, East Indian, and Ross Sea Sectors, providing a focus for future ice shelf instability studies. The projected sensitivity of future damage development is

ultimately driven by ocean warming induced by climate change, that controls the amount of thinning and acceleration of the ice shelves.

Chapter 4 concludes that the implications of observed and predicted damage on ice shelves with respect to Antarctic mass loss are two-fold. On the one hand, weakened ice shelves are shown to be associated with thinning and accelerating ice shelves, enhancing dynamic mass loss through loss of buttressing and increased ice flux over the grounding line. Secondly, weak ice shelves are more prone to calving, increasing susceptibility to significant retreat or collapse due to external forcing – potentially even preconditioning otherwise-stable ice shelves for collapse.

5.4 Perspectives and recommendations

The combined results of all chapters underscore the critical importance of better quantifying the impacts of damage on ice shelf stability, in order to improve estimates of future Antarctic mass loss. Without accounting for damage processes in ensemble projections of the Antarctic Ice Sheet, we are currently likely underestimating the magnitude and/or the timing of ice shelf retreat and Antarctic mass loss, contingent on future climate scenarios. Addressing this underestimation is pivotal for refining our estimation of Antarctica's contribution to sea level rise. In order to do better quantify damage impacts on Antarctic mass loss, improved representation of damage processes in ice sheet models is required. A few considerations are detailed below, as well as suggestions on how to focus and refine observations of damage for this goal.

5.4.1 Model evaluation with damage detected from observations

The evaluation of calving laws, fracture mechanics models and continuum damage models (CDM) is an essential step in improving our understanding of key processes that govern ice shelf weakening and retreat, and constraining estimates of future ice mass loss. Ice sheet models have, so far, rarely successfully predicted major ice shelf calving events before they occurred. Rather, they have been used as forensic tools to hunt for clues about the causes and drivers of ice shelf change (Bassis et al., 2023).

The produced damage maps presumably offer a way to evaluate large ice sheet models in their ability to simulate patterns of ice shelf weakening. The spatiotemporal maps produced by NeRD are expected to be useful to assess CDM models, where effects on the bulk properties of the ice are considered and the need for resolving individual fractures can be avoided. For one, the produced damage maps can potentially be used as a proxy for the often used scalar 'damage' parameter (D) in CDM models, which represents the reduction in effective ice viscosity caused by the presence of fractures (Lemaitre, 2012; Borstad et al., 2012). This would require a translation of the (continuous) damage signal detected by NeRD to the scalar parameter D used in these models. The strength of the damage signal already provides some indication of fracture size (with larger, deeper fractures returning stronger signals), which could be further explored and optimised. For example, information about crevasse depth obtained from altimetry data can be used to enrich the spatial distribution of NeRD-detected damage and so construct a parameteri-

sation of the scalar damage parameter D . However, the scalar parameter D also includes effects of micro cracks and pre-existing flaws on the load-bearing capacity of the ice, aside from effects induced by open crevasses (Benn and Åström, 2018). Such small, internal features can never be observed from remote sensing observations. The translation of observable and detected damage to the scalar damage parameter, therefore, requires appropriate tuning and testing before a parameterisation can be constructed.

Alternatively, the damage maps can potentially be assimilated into fracture or continuum mechanics models to better constrain initial parameters of ice rheology, such as the effective ice viscosity. However, the few studies so far that have compared observed to modelled crevasses have found limited agreement in crevasse patterns and ice rheological parameters (Enderlin and Bartholomaus, 2020; Gerli et al., 2023b). It is likely that not all observed crevasses or fractures are of importance to the dynamics of the ice shelf (as suggested by Gerli et al., 2023a). Therefore, before observed damage maps can be used effectively to constrain ice rheological parameters, a better distinction could be made to filter ‘relevant’ damage from the bulk of observations. Potentially such a feat could be achieved by incorporating information of additional datasets to filter the damage dataset, e.g. stress or strain rates (Lv et al., 2022) or spatial information such as the distance to the ice front. For damage maps produced by NeRD, a simple first filtering step would be to discretise different damage signal classes and focus only on areas with high damage signals. Another possibility is to focus on capturing damage changes rather than the reproduction of static crevasse maps. This approach would put emphasis on active, weakening areas – assuming these areas are of higher importance to overall ice dynamic behaviour than passive (surface) crevasses (Rydt et al., 2019; Lhermitte et al., 2020; Gerli et al., 2023a). This could yield to an assessment similar to Lai et al. (2020), and provide nuance as to when and where fractures have (strong) impact on ice rheology.

5.4.2 Towards monitoring fracture initiation and calving

Apart from capturing large weakening patterns of ice shelves with ice sheet models, it is also imperative that ice shelf calving and retreat is better resolved and predicted.

To calibrate, validate and test existing theories of fracture and calving processes at a fundamental scale, observations of very high spatial and temporal resolution are required (Bassis et al., 2023). Although the produced damage maps are using high spatial resolution satellite imagery (30 m spatial resolution), a higher resolution would be desirable to study the initiation and development of individual fractures. And, whereas the overall evolution of large rifts often takes place over multiple years or decades, propagation often occurs in burst over short periods of time until calving occurs (Borstad et al., 2017; Rydt et al., 2019). Studying these events in detail would require weekly to monthly monitoring; an endeavour not easily automated on the large Antarctic domain.

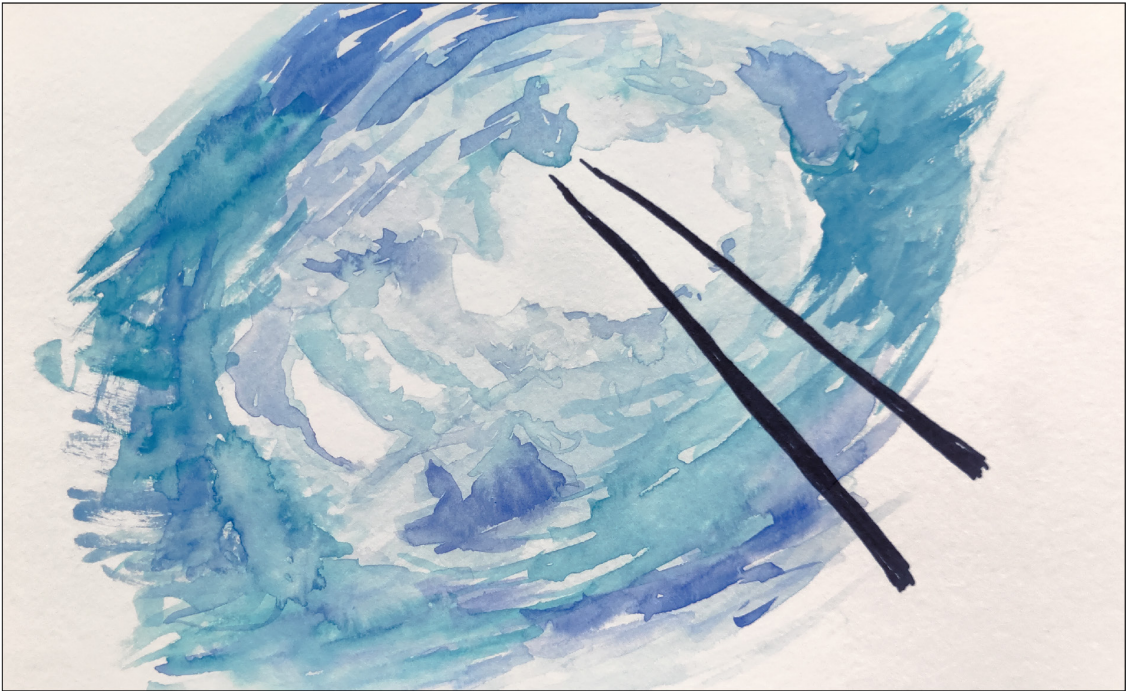
The current development in fracture detection methods already has the potential to be used to track and monitor fracture opening. Especially machine learning approaches would be suitable for this task due to their capability in individual fracture segmentation and fast and efficient data processing. A potential workflow could be to first infer ‘important’ fractures from large scale damage maps – where ‘important’ can be in terms of its impact on ice shelf weakening, its likelihood to result in calving or its susceptibility to

hydrofracture. Then, as a second step, to make use of targeted super high resolution data for detailed monitoring. Daily or even sub-daily acquisitions at meter-scale resolution are becoming available (for example, ICEYE's constellation of agile satellites).

Lastly, in order to accurately quantify future calving rates and ice shelf retreat of Antarctic ice shelves, it is crucial that the influence of environmental forcing on rift propagation is captured accurately as well. Rift propagation and calving can be stabilised by land fast or sea ice (Cheng et al., 2021), destabilised by ice mélange (Poinelli et al., 2023), altered by basal melt or refreezing (Dow et al., 2018; Bassis and Ma, 2015) or triggered by hydrofracturing when surface crevasses are inundated with meltwater (ultimately depending on atmospheric conditions) (Lai et al., 2020).

5.5 Final note

In conclusion, there is still a way to go before accurate, long-term predictions of ice shelf weakening, calving and retreat can be made, and how much Antarctic mass loss can be expected as a result. Here, we have provided valuable insights in the spatial distribution of damage and damage change across Antarctic ice shelves. The developed NeRD method as well as the produced Antarctic damage maps are open-source available, providing a valuable resource to the community for future research. By leveraging large spatiotemporal remote sensing observations the link of observed damage to ice shelf retreat and ice shelf weakening is shown, and a sensitivity of ice shelf weakening to future climate scenarios is revealed. Overall, these findings contribute to our understanding of the impact of damage on ice shelf stability.



Appendix A

Code and Data Availability

Code

The code of the developed NeRD method is available on github,
<https://github.com/mizeboud/NormalisedRadonTransform>.

The code to pre-process satellite data, to post-process pan-Antarctic damage assessments, and to develop and apply the Random Forest model to provide future damage projections, is available at:

<https://github.com/mizeboud/antarctic-damage-change>

Data produced in this thesis

Annual Antarctic Damage Maps

The developed annual damage maps can be viewed or accessed in the Google Earth Engine, <https://code.earthengine.google.com/e091fa357d068a23be6722c37ef66590>. The maps are furthermore published and available as tiled geotiff and netcdf files at the 4TU data repository with DOI: 10.4121/911e8799-f0dc-42e3-82b4-766ad680a71e.



SCAN ME

Other Supporting data

The adjusted annual ice shelf polygons of Greene et al. (2022), created for Chapter 3 & 4, as well as other supplementary data, such as a list of all processed orbits of Sentinel-1, supporting shape-files, and NetCDF files of projected damage values, are made available at the 4TU research data repository with DOI: 10.4121/911e8799-f0dc-42e3-82b4-766ad680a71e.

Used satellite data

The satellite imagery data used in this thesis is open-source available. Most datasets have been accessed via the Google Earth Engine (GEE), for which code is made available.

- **Sentinel & Landsat images for Chapter 2.** Accessed through GEE. Code: <https://code.earthengine.google.com/63b4cf06dffc7c6b5695dbd256e844fd>
- **Sentinel-1 images for Chapter 3** accessed through GEE. Code is included in the code repository (see above), and a list of processed images is included with the published supplementary material of this chapter at the 4TU data repository, doi:10.4121/911e8799-f0dc-42e3-82b4-766ad680a71e
- **RAMP Radarsat mosaic.** The RAMP AMM-1 SAR Image Mosaic of Antarctica (Jezek et al., 1998), Version 2, is available at Alaska Satellite Facility - Distributed Active Archive Center. <https://asf.alaska.edu/data-sets/derived-data-sets/ramp/ramp-get-ramp-data/>
- **MODIS MOA2009 mosaic.** The MODIS MOA2009 mosaic (Haran et al., 2014) is available at the National Snow & Ice Data Center (NSIDC): <https://nsidc.org/data/nsidc-0593/>.
- **ITS_LIVE ice flow velocity.** Available through the data portal at <https://nsidc.org/apps/itslive/> (Gardner et al., 2019).
- **Reference Elevation Model of Antarctica (REMA).** Accessed through GEE, asset with ID 'UMN/PGC/REMA/V1_1/8m' (Howat et al., 2019).

Other data

- **MEaSURES grounding line and ice boundaries.** This thesis uses the MEaSURES grounding line (Rignot et al., 2016) and ice shelf boundaries (Mouginot et al., 2017b), available at the National Snow and Ice Data Center (NSIDC): <https://nsidc.org/data/nsidc-0709/versions/2>.
- **ISMIP-6 project model data.** Output data of ice sheet models participating in the ISMIP-6 project is available through a Globus endpoint (Nowicki et al., 2021), instructions and information are available at GitHub: <https://thegithub.org/resources/4748>.
- **Quantarctica.** To produce visually pleasing maps, the Quantarctica dataset for QGIS (Matsuoka et al., 2018) was used to provide map layers with additional relevant information.
- **Scientific Colormaps.** The scientific colour maps *batlow* and *roma* from Crameri (2018) were used in this thesis to prevent visual distortion of the data and exclusion of readers with colour vision deficiencies. doi:10.5281/zenodo.8409685

Appendix B

Supplementary Figures for Chapter 2

This appendix contains supplementary figures for Chapter 2, as published alongside the main article, Izeboud, M. and Lhermitte, S., 2023, Damage detection on Antarctic ice shelves using the normalised radon transform. *Remote Sensing of Environment*, 284, 113359, <https://doi.org/10.1016/j.rse.2022.113359>

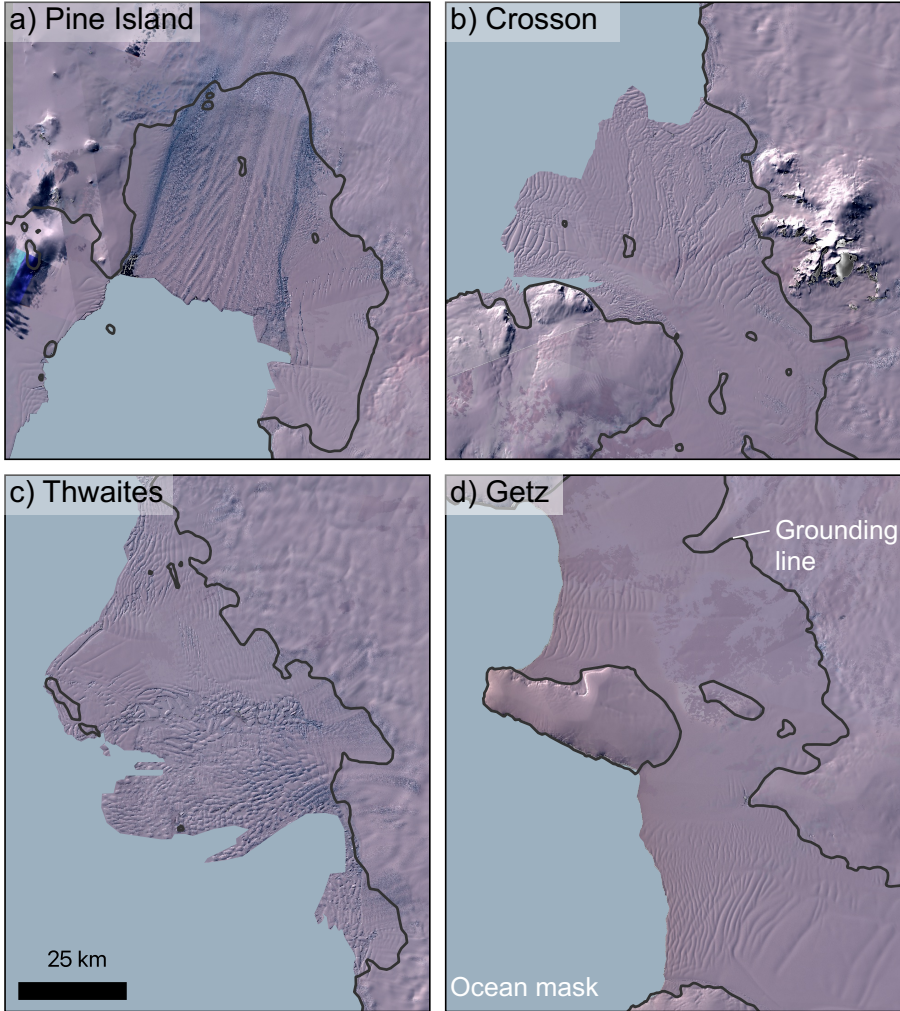


Figure B.1: **Median image composites of Sentinel-2 optical images.** Data acquired during austral summer (December, January, February) 2020-2021. Images displayed are R-G-B spectral bands on (a) Pine Island, (b) Thwaites, (c) Crosson and (d) Getz ice shelves. Grounding lines (dark grey line, Rignot et al. (2016)) and an ocean mask (light blue area, adjusted from Mouginot et al. (2017)) are added to the plot.

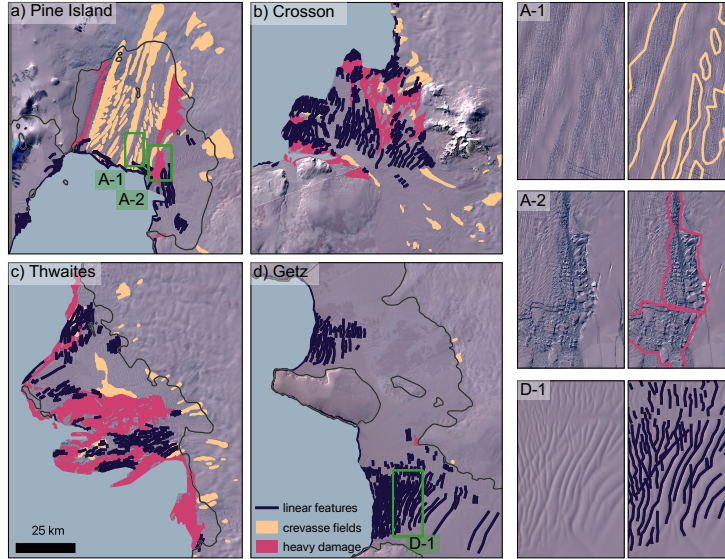


Figure B.2: **Manually labelled damage features.** Labelled (a) Pine Island, (b) Crosson, (c) Thwaites and (d) Getz ice shelf, on the Sentinel-2 median image RGB composite of DJF 2020-2021. Labels were grouped in three classes: linear features, densely crevassed fields and areas with heavy damage including open rifts and ice melange. Three zoom areas are selected to show the original image and the respective labels for surface crevasse fields (A-1), heavy damage areas (A-2) and linear features (D-1). Grounding lines (dark grey line, Rignot et al. (2016)) and an ocean mask (light blue area, adjusted from Mouginot et al. (2017)) are added to the plot.

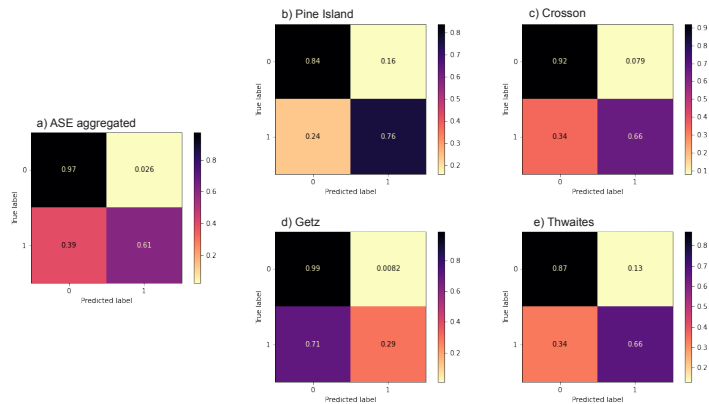


Figure B.3: **Confusion matrices.** Validating the NeRD damage detection to damage labels on (a) the full ASE area, (b) Pine Island, (c) Crosson, (d) Thwaites and (e) Getz ice shelf. The confusion matrix is normalised with respect to the number of true labels. All grounded ice has been removed before calculating these values.

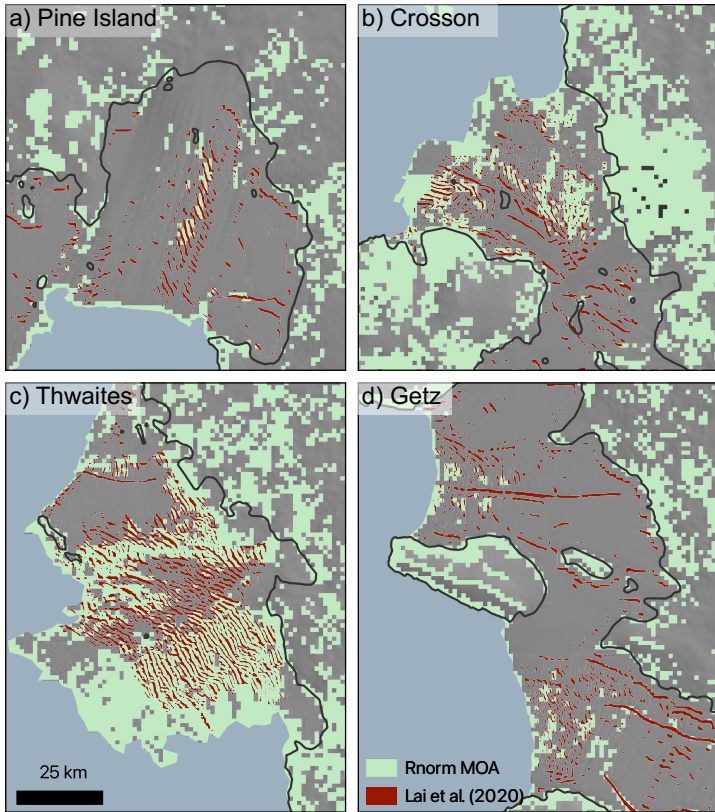


Figure B.4: **Detected damage on the MODIS Mosaic of Antarctica 2008-2009 (MOA2009).** Damage pixels classified if $\hat{D} > 0$. MOA2009 shown as background image on the selected ice shelves: (a) Pine Island, (b) Thwaites, (c) Crosson and (d) Getz ice shelves. Detected damage pixels as result from the Normalised Radon transform, applied to 10x10 pixel windows (1250m) with pixels of 125m resolution, are shown in light green. Red values represent the detected fractures by Lai et al. (2020) using a machine learning approach. Grounding lines (dark grey line, Rignot et al. (2016)) and an ocean mask (light blue area, adjusted from Mouginot et al. (2017)) are added to the plot.

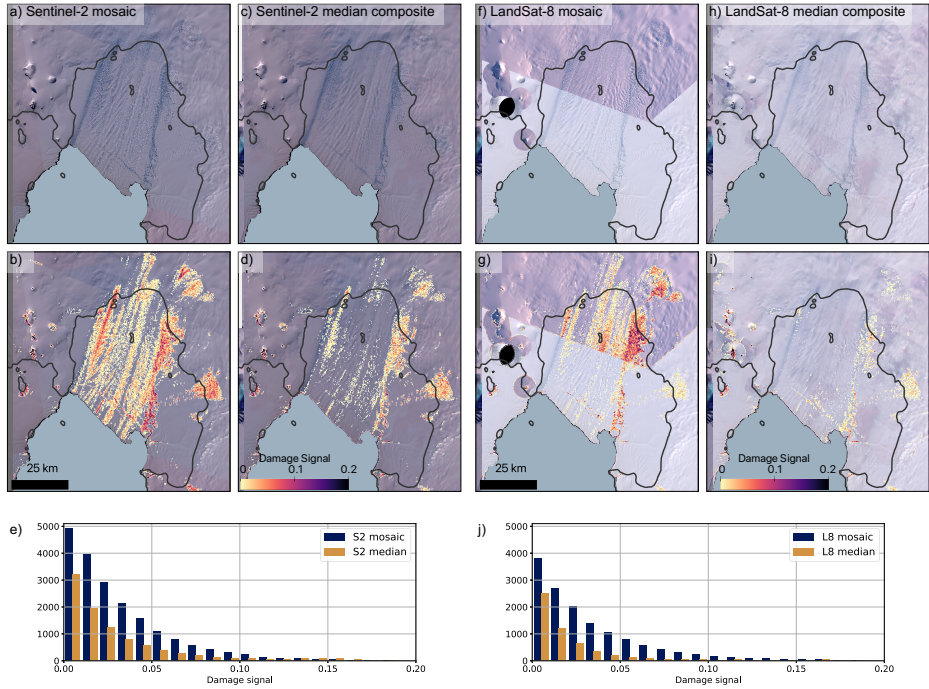


Figure B.5: Damage detection for different image pre-processing procedures. Example of applying the NeRD method to data from the same source but using different image selection procedures, applied for both Sentinel-2 and LandSat-8 during austral summer 2019-2020. Panel (a) and (f) show a mosaic of individual images with the least-cloudy image on top; panel (c) and (h) show a median image composite. Panels (b,d,g,i) show the respective detected damage and (e) and (j) show a histogram of the different damage signal values. Grounding lines (dark grey line, Rignot et al. (2016)) and an ocean mask (light blue area, adjusted from Mouginot et al. (2017)) are added to the plot.

Table B.1: Overview of created image composites or mosaics for different austral summers (December, January, February), their respective data sources and the Figure number that they are displayed in. The images were retrieved using Google Earth Engine, for which the code is made available.

Austral summer	Source	Image type	Used for	Figure
2008-2009	Landsat 7	median composite	Validation to Lai et al. (2020)	Fig.11
2013-2014	Landsat 8	median composite	Temporal analysis	Fig.12
2015-2016	Landsat 8	median composite	Temporal analysis	Fig.12
2017-2018	Sentinel-2	median composite	Temporal analysis	Fig.12
2019-2020	Sentinel-2	spatial mosaic	Spectral bands sensitivity test, pre-processing choice	Fig.12, Sup.Fig.5
	Sentinel-1	spatial mosaic	Sensor sensitivity test	Fig.7
	Landsat 8	median composite	Sensor sensitivity test	Fig.7
	Sentinel-2	median composite	Sensor sensitivity test, resolution sensitivity test and temporal analysis	Fig.7, Fig.4, Fig.12
2020-2021	Sentinel-2	median composite	Application to study area	Fig.8

Appendix C

Supplementary Material for Chapter 3

Sensor Sensitivity of NeRD algorithm

In this supplementary section we provide a more detailed assessment of the sensitivity of the utilised NeRD algorithm to the variations between satellite imagery obtained by different sensors. This appends to method section ‘*Damage detection with NeRD algorithm*’ of the main manuscript.

While the NeRD method effectively minimizes disparities in detected damage signal values between different sensors through the sensor- and resolution-specific noise thresholds, some variations may persist due to two key factors: i) changes in surface conditions that influence the SAR backscatter signal and ii) differing levels of sensitivity to the spatial variability of surface conditions.

(i) Changes in surface conditions

Images acquired at different dates contain changes in surface conditions that influence the SAR back-scatter signal. Alterations in surface features like snow cover, surface roughness, and liquid water content can affect the visibility of identical fracture features in radar images. In our efforts to minimise the influence of changing surface conditions between the yearly Sentinel-1 and RAMP assessments, we consistently acquired imagery during the same austral fall period (September–October–November).

(ii) Sensitivity to spatial variability

Sensors may exhibit differing levels of sensitivity to the spatial variability of surface conditions, resulting in varying damage signal values for the same feature. Factors contributing to this variation include differences in look-angle, wavelength, and image pixel resolution. Contrasts of features can shift based on the sensor’s pixel resolution, as well as the chosen processing kernel size of the NeRD algorithm, further amplifying this effect (Izeboud and Lhermitte, 2023).

To estimate the sensitivity of NeRD to contrast variability between the RAMP and Sentinel-1 sensors, we tested (a) the difference between processing kernel size for Sentinel-1 imagery and (b) the difference between processed RAMP and Sentinel-1 imagery. We selected a specific area on grounded ice with pronounced terrain shadows (i.e. image contrast) for these tests. While the signals detected by NeRD in such regions are not true damage signals, they serve as a means to gain insights into the sensor bias. This area

was chosen based on the assumption that surface characteristics are similar enough in 1997 and 2021 for such a comparison – an assumption that would not be valid for actual damaged areas that are typically very variable in time.

Two distinct approaches were employed to attain the same 1000 m output resolution for Sentinel-1 data as the RAMP data (processed with 10-pixel kernels), and so test the sensitivity of NeRD to this choice: (a) processing 40 m resolution images with a 25-pixel kernel size and (b) initially down-scaling the 40 m resolution images to a 100 m grid (using nearest neighbour approach, applied in the image export command of Google Earth Engine), followed by processing with 10-pixel kernel size. The used NeRD signal noise threshold (τ , refer to (Izeboud and Lhermitte, 2023) or main manuscript) were $\tau_{S1;40m:25px} = 0.041$; $\tau_{S1;100m:10px} = 0.038$.

The average damage signal and standard deviation in the selected grounded area was assessed as follows:

$$\begin{aligned}\overline{\hat{D}(\text{RAMP})}_{100m:10px} &= 0.008 \pm 0.015, \\ \overline{\hat{D}(S1)}_{100m:10px} &= 0.010 \pm 0.023, \\ \overline{\hat{D}(S1)}_{40m:25px} &= 0.009 \pm 0.022.\end{aligned}$$

The bias between the two radar sensors is therefore 0.002 or 0.001, depending on the processing resolution choice for Sentinel-1. Notably, this difference is an order of magnitude smaller than the standard deviation of the signal itself, and can be considered insignificant. This instills confidence in the comparability of RAMP and Sentinel-1 damage assessments. We continued our damage change assessments by comparing the $RAMP_{100m:10px}$ damage maps to $S1_{40m:25px}$ maps.

Supplementary Figures

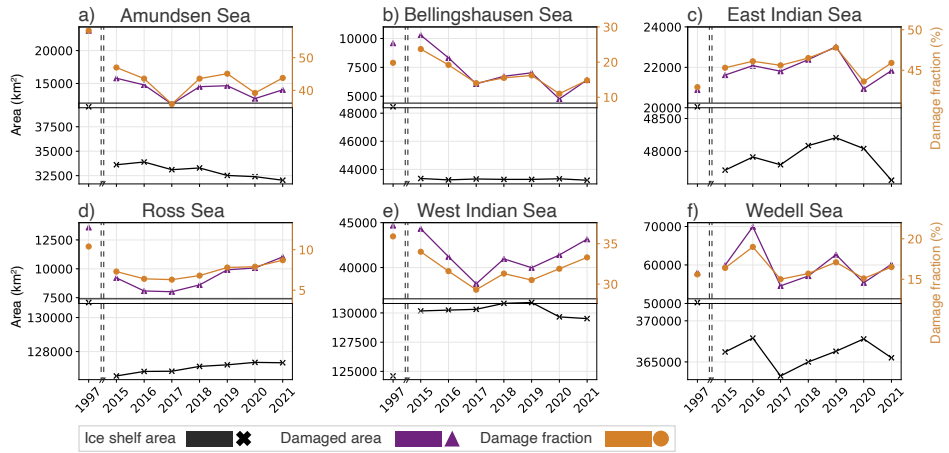


Figure C.1: **Time series of damage per sector.** Each panel shows annual damaged (purple) and ice shelf (black) area on the left y-axis and the fraction of damage to ice shelf area (orange) on the right y-axis.



Figure C.2: **Annual damage assessments obtained from NeRD algorithm.** No-data areas are shown in gray; for the 1997 assessment (from the RAMIP mosaic (Jezek et al., 1998)) the shown red tiles were excluded from the assessments to achieve similar data coverage as Sentinel-1 (2015-2021). The pie charts represent the aggregated values for all ice shelves in the defined sectors by counting pixels of no-data (light gray), no-damage (light blue, $\hat{D} = 0$) or damaged class (purple, $\hat{D} > 0$). Percentages are displayed for the no-damage/damage class. The total ice shelf area varies per year using the annual calving front positions adapted from Greene et al. (2022).

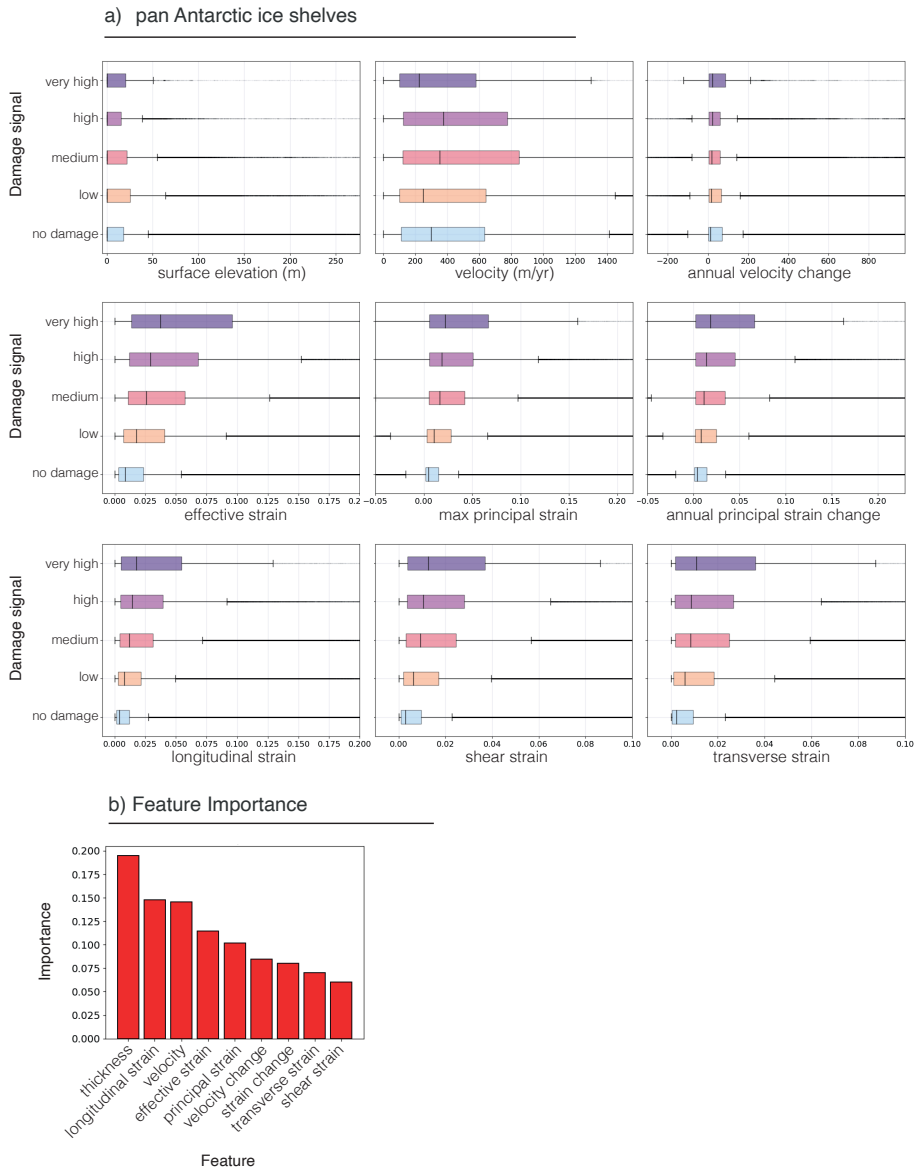


Figure C.3: **Random Forest input feature information.** (a) Correlation of input features used for training the RF model on pan-Antarctic scale. Damage signal values are binned by low to high signal values, to favor visualisation of the minority (high damage signal) class (low: $\hat{D} \in (0, 0.0125]$, medium: $\hat{D} \in (0.0125, 0.0625]$, high: $\hat{D} \in (0.0625, 0.5]$). (b) feature importance as result of the RF model training.



Figure C.4: **Predicted damage values between 2015-2100.** Values were obtained from the RF model using input data from five ice sheet models. **(a)** PISM (Winkelmann et al., 2011), **(b)** SICOPOLIS (Greve et al., 2020), **(c)** MALI (Hoffman et al., 2018), **(d)** ISSM (Schlegel et al., 2018), **(e)** CISM (Lipscomb et al., 2021), limited to ice shelf area and averaged over the whole domain. Each panel shows predicted values for the control experiment and four climate forcing experiments, exp 05, 06, 07 and 08, smoothed with a 5-year running mean.

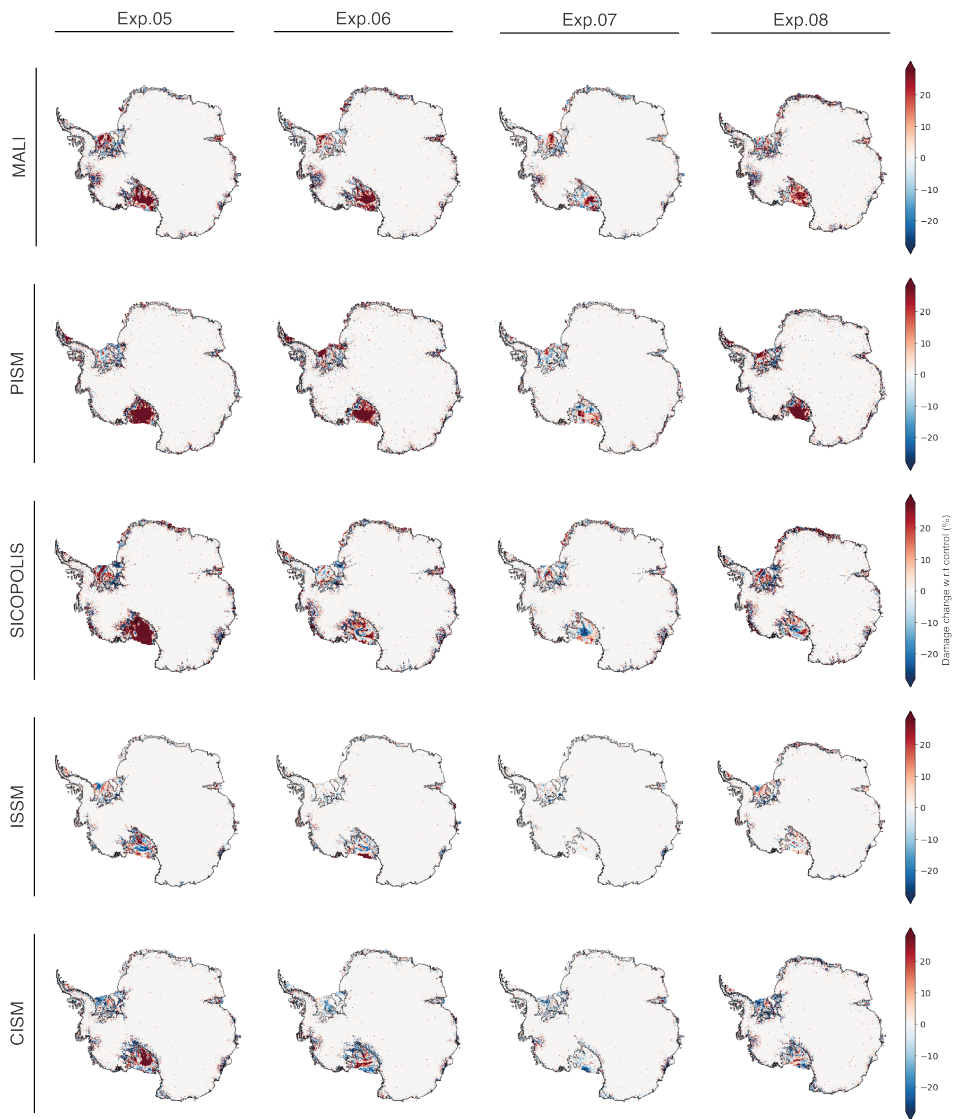


Figure C.5: **Spatial plots of predicted damage change (%) at year 2100**, shown for each climate forcing experiment and ice sheet model.

Appendix D

Some more damage maps

This appendix contains multiple figures displaying damage maps of selected areas along the periphery of Antarctica. All maps show detected damage by NeRD on the RAMP mosaic (1997) and Sentinel-1 (2015-2021) SAR imagery. The damage map of 1997 is 1000 m resolution, the others 400 m spatial resolution. Data is clipped to ice shelf areas as obtained from adjusted ice front positions (Greene et al., 2022) and a static grounding line (Rignot et al., 2016). The figures show a shaded DEM on grounded ice areas (Matsuoka et al., 2018).

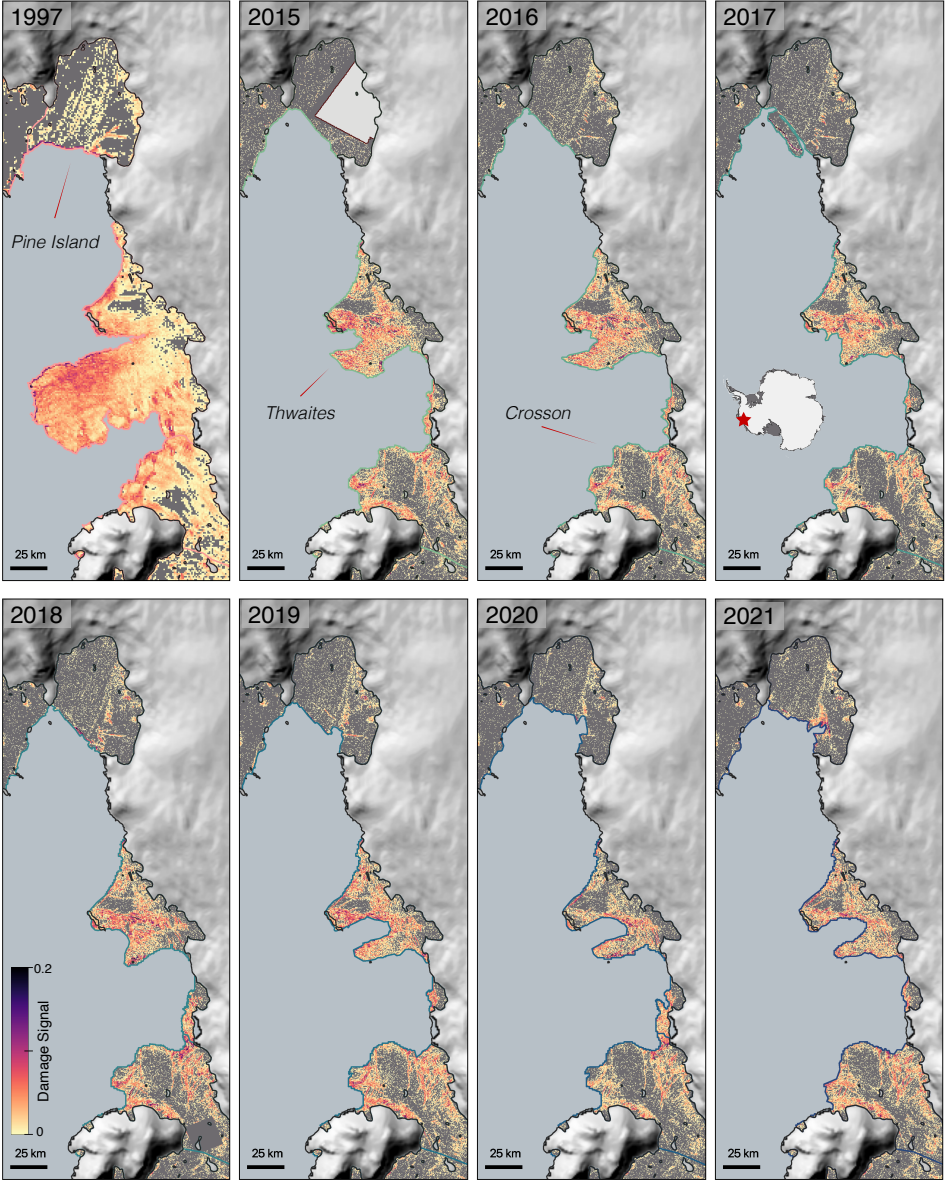


Figure D.1: Damage map of ice shelves in Amundsen Sea Embayment

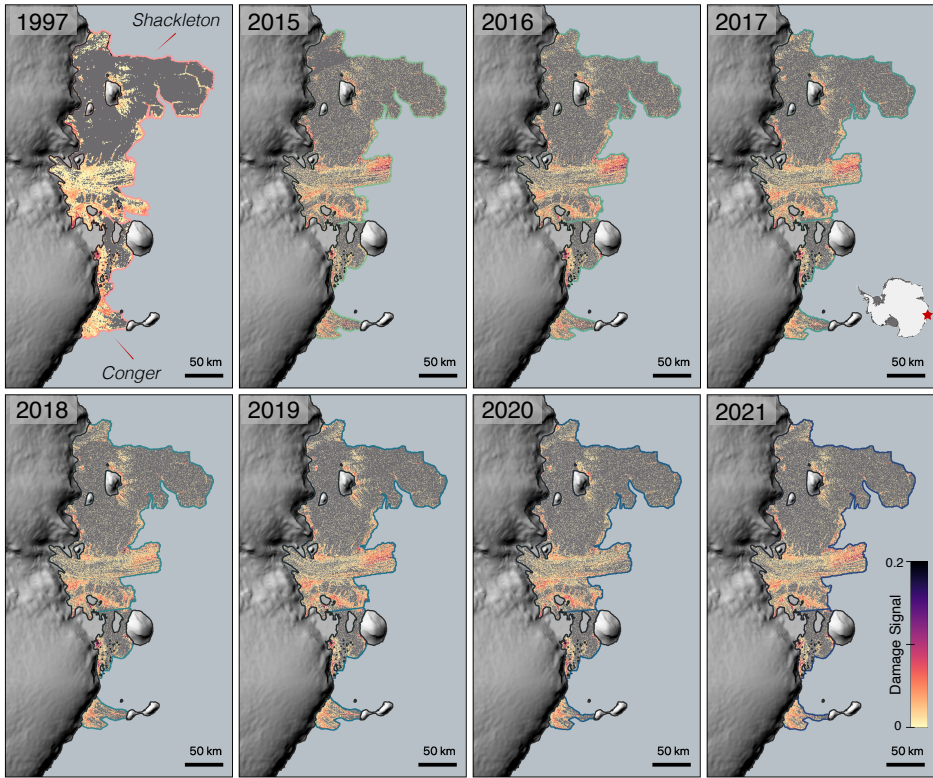


Figure D.2: Damage map of Shackleton and Conger ice shelves

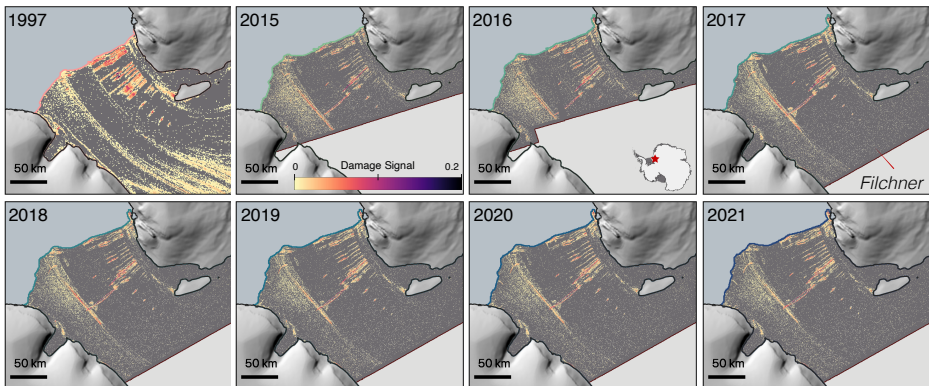


Figure D.3: Damage map of Filchner ice shelf

Bibliography

- Adusumilli, S., Fricker, H. A., Medley, B., Padman, L., and Siegfried, M. R. (2020). Interannual variations in meltwater input to the southern ocean from antarctic ice shelves. *Nature Geoscience*.
- Ahmad, M. W., Mourshed, M., and Rezgui, Y. (2017). Trees vs neurons: Comparison between random forest and ann for high-resolution prediction of building energy consumption. *Energy and Buildings*, 147:77–89.
- Albrecht, T. and Levermann, A. (2012). Fracture field for large-scale ice dynamics. *Journal of Glaciology*, 58:165–176.
- Albrecht, T. and Levermann, A. (2014). Fracture-induced softening for large-scale ice dynamics. *The Cryosphere*, 8:587–605.
- Alley, K. E., Scambos, T. A., Alley, R. B., and Holschuh, N. (2019). Troughs developed in ice-stream shear margins precondition ice shelves for ocean-driven breakup. *Science Advances*, 5.
- Alley, K. E., Scambos, T. A., Anderson, R. S., Rajaram, H., Pope, A., and Haran, T. M. (2018). Continent-wide estimates of antarctic strain rates from landsat 8-derived velocity grids. *Journal of Glaciology*, 54. - Useful paper for comparing nominal to logarithmic strain-rate calculations

- look into referencing of this paper for other strain rate articles.
- Alley, K. E., Wild, C. T., Luckman, A., Scambos, T. A., Truffer, M., Pettit, E. C., Muto, A., Wallin, B., Klinger, M., Sutterley, T., Child, S. F., Hulen, C., Lenaerts, J. T. M., MacLennan, M., Keenan, E., and Dunmire, D. (2021). Two decades of dynamic change and progressive destabilization on the thwaites eastern ice shelf. *The Cryosphere*, 15:5187–5203.
- Alley, R. B., Cuffey, K. M., Bassis, J. N., Alley, K. E., Wang, S., Parizek, B. R., Anandakrishnan, S., Christianson, K., and Deconto, R. M. (2023). Iceberg calving: Regimes and transitions. *Annual Review of Earth and Planetary Sciences*, 51:189–215.
- Alley, R. B., Horgan, H. J., Joughin, I., Cuffey, K. M., Dupont, T. K., Parizek, B. R., Anandakrishnan, S., and Bassis, J. (2008). A simple law for ice-shelf calving. *Science*, 322:1344.
- Altena, B. (2018). Observing change in glacier flow by using optical satellites. Doctoral Dissertation, University of Oslo.
- Andreasen, J. R., Hogg, A. E., and Selley, H. L. (2023). Change in antarctic ice shelf area from 2009 to 2019. *Cryosphere*, 17:2059–2072.
- Araujo, A., Norris, W., and Sim, J. (2019). Computing receptive fields of convolutional neural networks. *Distill*, 4.
- Arndt, J. E., Larter, R. D., Friedl, P., Gohl, K., and Höppner, K. (2018). Bathymetric controls on calving processes at pine island glacier. *The Cryosphere*, 12:2039–2050.
- Arthur, J. F., Stokes, C. R., Jamieson, S. S. R., Miles, B. W. J., Carr, J. R., and Leeson, A. A. (2021). The triggers of the disaggregation of voyeykov ice shelf (2007), wilkes land, east antarctica, and its subsequent evolution. *Journal of Glaciology*, pages 1–19.
- Arzeno, I. B., Beardsley, R. C., Limeburner, R., Owens, B., Padman, L., Springer, S. R., Stewart, C. L., and Williams, M. J. (2014). Ocean variability contributing to basal melt rate near the ice front of ross ice shelf, antarctica. *Journal of Geophysical Research: Oceans*, 119:4214–4233.
- Bamber, J. L., Riva, R. E. M., Vermeersen, B. L. A., and LeBrocq, A. M. (2009). Reassessment of the potential sea-level rise from a collapse of the west antarctic ice sheet. *Science*, 324:901–903.
- Banwell, A. F., MacAyeal, D. R., and Sergienko, O. V. (2013). Breakup of the larsen b ice shelf triggered by chain reaction drainage of supraglacial lakes. *Geophysical Research Letters*, 40:5872–5876.
- Banwell, A. F., Willis, I. C., Macdonald, G. J., Goodsell, B., and MacAyeal, D. R. (2019). Direct measurements of ice-shelf flexure caused by surface meltwater ponding and drainage. *Nature Communications*, 10.
- Banwell, A. F., Willis, I. C., MacDonald, G. J., Goodsell, B., Mayer, D. P., Powell, A., and MacAyeal, D. R. (2017). Calving and riftng on the mcmurdo ice shelf, antarctica. *Annals of Glaciology*, 58:78–87.
- Bassis, J. N., Crawford, A., Kachuck, S. B., Benn, D. I., Walker, C., Millstein, J., Duddu, R., Janåström, J. J., Fricker, H., and Luckman, A. (2023). Stability of ice shelves and ice cliffs in a changing climate. *Annual Review of Earth and Planetary Sciences*.
- Bassis, J. N. and Ma, Y. (2015). Evolution of basal crevasses links ice shelf stability to ocean forcing. *Earth and Planetary Science Letters*, 409:203–211.

- Bassis, J. N. and Walker, C. C. (2012). Upper and lower limits on the stability of calving glaciers from the yield strength envelope of ice. *Proceedings of the Royal Society A: Mathematical, Physical and Engineering Sciences*, 468:913–931.
- Benn, D. I., Luckman, A., Åström, J. A., Crawford, A. J., Cornford, S. L., Bevan, S. L., Zwinger, T., Gladstone, R., Alley, K., Pettit, E., and Bassis, J. (2022). Rapid fragmentation of thwaites eastern ice shelf. *Cryosphere*, 16:2545–2564.
- Benn, D. I. and Åström, J. A. (2018). Calving glaciers and ice shelves. *Advances in Physics*, 3:1513819.
- Berger, S., Favier, L., Drews, R., Derwael, J. J., and Pattyn, F. (2016). The control of an uncharted pinning point on the flow of an antarctic ice shelf. *Journal of Glaciology*, 62.
- Bhardwaj, A., Sam, L., Singh, S., and Kumar, R. (2016). Automated detection and temporal monitoring of crevasses using remote sensing and their implications for glacier dynamics. *Annals of Glaciology*, 57:81–91.
- Borstad, C., Khazendar, A., Scheuchl, B., Morlighem, M., Larour, E., and Rignot, E. (2016). A constitutive framework for predicting weakening and reduced buttressing of ice shelves based on observations of the progressive deterioration of the remnant larsen b ice shelf. *Geophysical Research Letters*, 43:2027–2035.
- Borstad, C., McGrath, D., and Pope, A. (2017). Fracture propagation and stability of ice shelves governed by ice shelf heterogeneity. *Geophysical Research Letters*, 44:4186–4194.
- Borstad, C. P., Khazendar, A., Larour, E., Morlighem, M., Rignot, E., Schodlok, M. P., and Seroussi, H. (2012). A damage mechanics assessment of the larsen b ice shelf prior to collapse: Toward a physically-based calving law. *Geophysical Research Letters*, 39.
- Borstad, C. P., Rignot, E., Mouginot, J., and Schodlok, M. P. (2013). Creep deformation and buttressing capacity of damaged ice shelves: theory and application to larsen c ice shelf. *The Cryosphere*, 7:1931–1947.
- Bull, C. Y., Jenkins, A., Jourdain, N. C., Vaňková, I., Holland, P. R., Mathiot, P., Hausmann, U., and Sallée, J. B. (2021). Remote control of filchner-ronne ice shelf melt rates by the antarctic slope current. *Journal of Geophysical Research: Oceans*, 126.
- Bulthuis, K., Arnst, M., Sun, S., and Pattyn, F. (2019). Uncertainty quantification of the multi-centennial response of the antarctic ice sheet to climate change. *Cryosphere*, 13:1349–1380.
- Calvin, K., Dasgupta, D., Krinner, G., Mukherji, A., Thorne, P. W., Trisos, C., Romero, J., Aldunce, P., Barrett, K., Blanco, G., Cheung, W. W., Connors, S., Denton, F., Diongue-Niang, A., Dodman, D., Garschagen, M., Geden, O., Hayward, B., Jones, C., Jotzo, F., Krug, T., Lasco, R., Lee, Y.-Y., Masson-Delmotte, V., Meinshausen, M., Mintenbeck, K., Mokssit, A., Otto, F. E., Pathak, M., Pirani, A., Poloczanska, E., Pörtner, H.-O., Revi, A., Roberts, D. C., Roy, J., Ruane, A. C., Skea, J., Shukla, P. R., Slade, R., Slangen, A., Sokona, Y., Sörensson, A. A., Tignor, M., van Vuuren, D., Wei, Y.-M., Winkler, H., Zhai, P., Zommers, Z., Hourcade, J.-C., Johnson, F. X., Pachauri, S., Simpson, N. P., Singh, C., Thomas, A., Totin, E., Alegria, A., Armour, K., Bednar-Friedl, B., Blok, K., Cissé, G., Dentener, F., Eriksen, E., Fischer, E., Garner, G., Guivarch, C., Haasnoot, M., Hansen, G., Hauser, M., Hawkins, E., Hermans, T., Kopp, R., Leprince-Ringuet, N., Lewis, J., Ley, D., Ludden, C., Niamir, L., Nicholls, Z., Some, S., Szopa, S., Trewin, B., van der Wijst, K.-I., Winter, G., Witting, M., Birt, A., and Ha, M. (2023). *IPCC, 2023: Climate Change 2023: Synthesis Report. Contribution of Working Groups I, II and III to the Sixth Assessment Report of the Intergovernmental Panel on Climate Change [Core Writing Team, H. Lee and J. Romero (eds.)]. IPCC, Geneva, Switzerland.*
- Cheng, Y., Xia, M., Qiao, G., Li, Y., Hai, G., and Lv, D. (2021). Calving cycle of ninnis glacier over the last 60 years. *International Journal of Applied Earth Observations and Geoinformation*, 105:102612.
- Christie, F. D. W., Benham, T. J., Batchelor, C. L., Rack, W., Montelli, A., and Dowdeswell, J. A. (2022). Antarctic ice-shelf advance driven by anomalous atmospheric and sea-ice circulation. *nature geoscience*, 15:356–362.
- Chudley, T. R., Christoffersen, P., Doyle, S. H., Dowling, T. P., Law, R., Schoonman, C. M., Bougamont, M., and Hubbard, B. (2021). Controls on water storage and drainage in crevasses on the greenland ice sheet. *Journal of Geophysical Research: Earth Surface*, 126.
- Chuter, S. J., Martín-Español, A., Wouters, B., and Bamber, J. L. (2017). Mass balance reassessment of glaciers draining into the abbot and getz ice shelves of west antarctica. *Geophysical Research Letters*.
- Clayton, T., Duddu, R., Siegert, M., and Martínez-Pañeda, E. (2022). A stress-based poro-damage phase field model for hydrofracturing of creeping glaciers and ice shelves a r t i c l e i n f o. *Engineering Fracture Mechanics*, 272:108693.
- Colgan, W., Rajaram, H., Abdalati, W., McCutchan, C., Mottram, R., Moussavi, M. S., and Grigsby, S. (2016). Glacier crevasses: Observations, models, and mass balance implications.
- Colgan, W., Steffen, K., McLamb, W. S., Abdalati, W., Rajaram, H., Motyka, R., Phillips, T., and Anderson, R. (2011). An increase in crevasse extent, west greenland: Hydrologic implications. *Geophysical Research Letters*, 38.
- Crameri, F. (2018). Scientific colour maps.

-
- Crawford, A. J., Benn, D. I., Todd, J., Åström, J. A., Bassis, J. N., and Zwinger, T. (2021). Marine ice-cliff instability modeling shows mixed-mode ice-cliff failure and yields calving rate parameterization. *Nature Communications*, 12.
- Cuffey, K. M. and Paterson, W. S. B. (2010). *The Physics of Glaciers - 4th Edition*. Academic Press, 4 edition.
- Davison, B. J., Hogg, A. E., Gourmelen, N., Jakob, L., Wuite, J., Nagler, T., Greene, C. A., Andreasen, J., and Engdahl, M. E. (2023). Annual mass budget of antarctic ice shelves from 1997 to 2021. *Science Advances*, 9.
- Donat-Magnin, M., Jourdain, N. C., Kittel, C., Agosta, C., Amory, C., Gallée, H., Krinner, G., and Chekki, M. (2021). Future surface mass balance and surface melt in the amundsen sector of the west antarctic ice sheet. *The Cryosphere*, 15:571–593.
- Dow, C. F., Lee, W. S., Greenbaum, J. S., Greene, C. A., Blankenship, D. D., Poinar, K., Forrest, A. L., Young, D. A., and Zappa, C. J. (2018). Basal channels drive active surface hydrology and transverse ice shelf fracture. *Science Advances*, 4.
- Duddu, R., Jiménez, S., and Bassis, J. (2020). A non-local continuum poro-damage mechanics model for hydrofracturing of surface crevasses in grounded glaciers. *Journal of Glaciology*, 66:415–429.
- Dupont, T. K. and Alley, R. B. (2005). Assessment of the importance of ice-shelf buttressing to ice-sheet flow. *Geophysical Research Letters*, 32.
- Dutrieux, P., Rydt, J. D., Jenkins, A., Holland, P. R., Ha, H. K., Lee, S. H., Steig, E. J., Ding, Q., Abrahamsen, E. P., and Schröder, M. (2014). Strong sensitivity of pine island ice-shelf melting to climatic variability. *Science*, 343:174–178.
- Edwards, T. L., Nowicki, S., Marzeion, B., Hock, R., Goelzer, H., Seroussi, H., Jourdain, N. C., Slater, D. A., Turner, F. E., Smith, C. J., McKenna, C. M., Simon, E., Abe-Ouchi, A., Gregory, J. M., Larour, E., Lipscomb, W. H., Payne, A. J., Shepherd, A., Agosta, C., Alexander, P., Albrecht, T., Anderson, B., Asay-Davis, X., Aschwanden, A., Barthel, A., Bliss, A., Calov, R., Chambers, C., Champollion, N., Choi, Y., Cullather, R., Cuzzone, J., Dumas, C., Felikson, D., Fettweis, X., Fujita, K., Galton-Fenzi, B. K., Gladstone, R., Golledge, N. R., Greve, R., Hattermann, T., Hoffman, M. J., Humbert, A., Huss, M., Huybrechts, P., Immerzeel, W., Kleiner, T., Kraaijenbrink, P., Léc'h, S. L., Lee, V., Leguy, G. R., Little, C. M., Lowry, D. P., Malles, J. H., Martin, D. F., Maussion, F., Morlighem, M., O'Neill, J. F., Nias, I., Pattyn, F., Pelle, T., Price, S. F., Quiquet, A., Radić, V., Reese, R., Rounce, D. R., Rückamp, M., Sakai, A., Shafer, C., Schlegel, N. J., Shannon, S., Smith, R. S., Straneo, F., Sun, S., Tarasov, L., Trusel, L. D., Breedam, J. V., van de Wal, R., van den Broeke, M., Winkelmann, R., Zekollari, H., Zhao, C., Zhang, T., and Zwinger, T. (2021). Projected land ice contributions to twenty-first-century sea level rise. *Nature*, 593:74–82.
- Ely, J. C. and Clark, C. D. (2016). Flow-stripes and foliations of the antarctic ice sheet. *Journal of Maps*, 12:249–259.
- Emet, V., Tregoning, P., Morlighem, M., Borstad, C., and Sambridge, M. (2018). A statistical fracture model for antarctic ice shelves and glaciers. *Cryosphere*, 12:3187–3213.
- Enderlin, E. M. and Bartholomäus, T. C. (2020). Sharp contrasts in observed and modeled crevasse patterns at greenland's marine terminating glaciers. *The Cryosphere*, 14:4121–4133.
- Fox-Kemper, B., Hewitt, H. T., Xiao, C., Aðalgeirsdóttir, G., Drijfhout, S. S., Edwards, T. L., Golledge, N. R., Hemer, M., Kopp, R. E., Krinner, G., Mix, A., Notz, D., Nowicki, S., Nurhati, I. S., Ruiz, J., Sallée, J.-B., Slangen, A. B. A., and Yu, Y. (2021). Ocean, cryosphere and sea level change. *Climate Change 2021: The Physical Science Basis. Contribution of Working Group I to the Sixth Assessment Report of the Intergovernmental Panel on Climate Change*, pages 1–257.
- Fretwell, P., Pritchard, H. D., Vaughan, D. G., Bamber, J. L., Barrand, N. E., Bell, R., Bianchi, C., Bingham, R. G., Blankenship, D. D., Casassa, G., Catania, G., Callens, D., Conway, H., Cook, A. J., Corr, H. F. J., Damaske, D., Damm, V., Ferraccioli, F., Forsberg, R., Fujita, S., Gim, Y., Gogineni, P., Griggs, J. A., Hindmarsh, R. C. A., Holmlund, P., Holt, J. W., Jacobel, R. W., Jenkins, A., Jokar, W., Jordan, T., King, E. C., Kohler, J., Krabill, W., Riger-Kusk, M., Langle, K. A., Leitchenkov, G., Leuschen, C., Luyendyk, B. P., Matsuoka, K., Mouginot, J., Nitsche, F. O., Nogi, Y., Nost, O. A., Popov, S. V., Rignot, E., Rippin, D. M., Rivera, A., Roberts, J., Ross, N., Siegert, M. J., Smith, A. M., Steinhage, D., Studinger, M., Sun, B., Tinto, B. K., Welch, B. C., Wilson, D., Young, D. A., Xiangbin, C., and Zirizzotti, A. (2013). Bedmap2: improved ice bed, surface and thickness datasets for antarctica. *The Cryosphere*, 7:375–393.
- Fricker, H. A., Bassis, J. N., Minster, B., and MacAyeal, D. R. (2005). Icesat's new perspective on ice shelf rifts: The vertical dimension. *Geophysical Research Letters*, 32.
- Fricker, H. A., Young, N. W., Allison, I., and Coleman, R. (2002). Iceberg calving from the amery ice shelf, east antarctica. *Annals of Glaciology*, 34:241–246.
- Fürst, J. J., Durand, G., Gillet-Chaulet, F., Tavard, L., Rankl, M., Braun, M., and Gagliardini, O. (2016). The safety band of antarctic ice shelves. *Nature Climate Change*, 6.
- Gardner, A. S., Fahnestock, M. A., and Scambos, T. A. (2019). Measures its_live landsat image-pair glacier and ice sheet surface velocities: Version 1.

- Gardner, A. S., Moholdt, G., Scambos, T., Fahnestock, M., Ligtenberg, S., Broeke, M. V. D., and Nilsson, J. (2018). Increased west antarctic and unchanged east antarctic ice discharge over the last 7 years. *Cryosphere*, 12.
- Gerli, C., Rosier, S., and Gudmundsson, G. H. (2023a). Activation of existing surface crevasses has limited impact on grounding line flux of antarctic ice streams. *Geophysical Research Letters*, 50.
- Gerli, C., Rosier, S., Gudmundsson, H., and Sun, S. (2023b). Weak relationship between remotely detected crevasses and inferred ice rheological parameters on antarctic ice shelves. *EGU sphere*, 2023:1–20.
- Glasser, N. and Scambos, T. (2008). A structural glaciological analysis of the 2002 larsen b ice-shelf collapse. *Journal of Glaciology*, 54:3–16.
- Gong, Y., Zwinger, T., Åström, J., Altena, B., Schellenberger, T., Gladstone, R., and Moore, J. C. (2018). Simulating the roles of crevasse routing of surface water and basal friction on the surge evolution of basin 3, austfonna ice cap. *Cryosphere*, 12:1563–1577.
- Gorelick, N., Hancher, M., Dixon, M., Ilyushchenko, S., Thau, D., and Moore, R. (2017). Google earth engine: Planetary-scale geospatial analysis for everyone. *Remote Sensing of Environment*.
- Greene, C. A., Gardner, A. S., Schlegel, N. J., and Fraser, A. D. (2022). Antarctic calving loss rivals ice-shelf thinning. *Nature*, 609:948–953.
- Greve, R., Calov, R., Obase, T., Saito, F., Tsutaki, S., and Abe-Ouchi, A. (2020). Ismp6 future projections for the antarctic ice sheet with the model sicopolis.
- Gudmundsson, G. H., Paolo, F. S., Adusumilli, S., and Fricker, H. A. (2019). Instantaneous antarctic ice sheet mass loss driven by thinning ice shelves. *Geophysical Research Letters*, 46:13903–13909.
- Han, T., Jiang, D., Zhao, Q., Wang, L., and Yin, K. (2018). Comparison of random forest, artificial neural networks and support vector machine for intelligent diagnosis of rotating machinery. *Transactions of the Institute of Measurement and Control*, 40:2681–2693.
- Haran, T., Bohlander, J., Scambos, T., Painter, T., and Fahnestock, M. (2014). *MODIS Mosaic of Antarctica 2008–2009 (MOA2009) Image Map, Version 2*. NASA National Snow and Ice Data Center Distributed Active Archive Center.
- Haran, T., Klinger, M., Bohlander, J., Fahnestock, M., Painter, T., and Scambos, T. (2018). *MEASUREs MODIS Mosaic of Antarctica 2013–2014 (MOA2014) Image Map, Version 1*. NASA National Snow and Ice Data Center Distributed Active Archive Center.
- Herzfeld, U. C., Trantow, T., Lawson, M., Hans, J., and Medley, G. (2021). Surface heights and crevasse morphologies of surging and fast-moving glaciers from icesat-2 laser altimeter data - application of the density-dimension algorithm (dda-ice) and evaluation using airborne altimeter and planet skysat data. *Science of Remote Sensing*, 3:100013.
- Hindmarsh, R. C. A. (2012). An observationally validated theory of viscous flow dynamics at the ice-shelf calving front. *Journal of Glaciology*, 58.
- Hoffman, M. J., Perego, M., Price, S. F., Lipscomb, W. H., Zhang, T., Jacobsen, D., Tezaur, I., Salinger, A. G., Tuminaro, R., and Bertagna, L. (2018). Mpas-albany land ice (mali): a variable-resolution ice sheet model for earth system modeling using voronoi grids. *Geoscientific Model Development*, 11:3747–3780.
- Hogg, A. E. and Gudmundsson, G. H. (2017). Impacts of the larsen-c ice shelf calving event. *Nature Climate Change* 2017 7:8, 7:540–542.
- Holland, P. R., Bracegirdle, T. J., Dutrieux, P., Jenkins, A., and Steig, E. J. (2019). West antarctic ice loss influenced by internal climate variability and anthropogenic forcing. *Nature Geoscience*, 12.
- Howat, I. M., Porter, C., Smith, B. E., Noh, M. J., and Morin, P. (2019). The reference elevation model of antarctica. *Cryosphere*, 13.
- Hu, Z., Munneke, P. K., Lhermitte, S., Izeboud, M., and Broeke, M. V. D. (2021). Improving surface melt estimation over the antarctic ice sheet using deep learning: A proof of concept over the larsen ice shelf. *Cryosphere*, 15:5639–5658.
- Hui, F., Li, X., Zhao, T., Shokr, M., Heil, P., Zhao, J., Liu, Y., Liang, S., and Cheng, X. (2016). Semi-automatic mapping of tidal cracks in the fast ice region near zhongshan station in east antarctica using landsat-8 oli imagery. *Remote Sensing*, 8:242.
- Hulbe, C. L., Ledoux, C., and Cruikshank, K. (2010). Propagation of long fractures in the ronne ice shelf, antarctica, investigated using a numerical model of fracture propagation. *Journal of Glaciology*.
- Husman, S. D. R., Hu, Z., Wouters, B., Munneke, P. K., Veldhuijsen, S., and Lhermitte, S. (2023). Remote sensing of surface melt on antarctica: Opportunities and challenges. *IEEE Journal of Selected Topics in Applied Earth Observations and Remote Sensing*, 16:2462–2480.
- Husman, S. D. R., Lhermitte, S., Bolibar, J., Izeboud, M., Hu, Z., Shukla, S., Meer, M. V. D., Long, D., and Wouters, B. (2024). A high-resolution record of surface melt on antarctic ice shelves using multi-source remote sensing data and deep learning. *Remote Sensing of Environment*, 301:113950.

-
- Huth, A., Duddu, R., and Smith, B. (2021). A generalized interpolation material point method for shallow ice shelves. 2: Anisotropic nonlocal damage mechanics and rift propagation. *Journal of Advances in Modeling Earth Systems*, 13:e2020MS002292.
- Huth, A., Duddu, R., Smith, B., and Sergienko, O. (2023). Simulating the processes controlling ice-shelf rift paths using damage mechanics. *Journal of Glaciology*.
- Izeboud, M. and Lhermitte, S. (2023). Damage detection on antarctic ice shelves using the normalised radon transform. *Remote Sensing of Environment*, 284.
- Izeboud, M., Lhermitte, S., Tricht, K. V., Lenaerts, J. T. M., Lipzig, N. P. M. V., and Wever, N. (2020). The spatiotemporal variability of cloud radiative effects on the greenland ice sheet surface mass balance. *Geophysical Research Letters*, 47.
- Jenkins, A., Shoosmith, D., Dutrieux, P., Jacobs, S., Kim, T. W., Lee, S. H., Ha, H. K., and Stammerjohn, S. (2018). West antarctic ice sheet retreat in the amundsen sea driven by decadal oceanic variability. *Nature Geoscience*, 11.
- Jezek, K. C. (1984). Recent changes in the dynamic condition of the ross ice shelf, antarctica. *JOURNAL OF GEOPHYSICAL RESEARCH*, 89:409–416.
- Jezek, K. C., Sohn, H. G., and Noltimier, K. F. (1998). Radarsat antarctic mapping project. *International Geoscience and Remote Sensing Symposium (IGARSS)*, 5:2462–2464.
- Joughin, I. and MacAyeal, D. R. (2005). Calving of large tabular icebergs from ice shelf rift systems. *Geophysical Research Letters*, 32:1–4.
- Joughin, I., Smith, B. E., and Medley, B. (2014). Marine ice sheet collapse potentially under way for the thwaites glacier basin, west antarctica. *Science*, 344:735–738.
- Jourdain, N. C., Asay-Davis, X., Hattermann, T., Straneo, F., Seroussi, H., Little, C. M., and Nowicki, S. (2020). A protocol for calculating basal melt rates in the ismip6 antarctic ice sheet projections. *The Cryosphere*, 14:3111–3134.
- Kachuck, S. B., Whitcomb, M., Bassis, J. N., Martin, D. F., and Price, S. F. (2022). Simulating ice-shelf extent using damage mechanics. *Journal of Glaciology*, 68.
- Kaluzienski, L., Koons, P., Enderlin, E., Hamilton, G., Courville, Z., and Arcone, S. (2019). Crevasse initiation and history within the mcmurdo shear zone, antarctica. *Journal of Glaciology*, 65:989–999.
- Krug, J., Weiss, J., Gagliardini, O., and Durand, G. (2014). Combining damage and fracture mechanics to model calving. *The Cryosphere*, 8:2101–2117.
- Lai, C. Y., Kingslake, J., Wearing, M. G., Chen, P. H. C., Gentine, P., Li, H., Spergel, J. J., and van Wessem, J. M. (2020). Vulnerability of antarctica's ice shelves to meltwater-driven fracture. *Nature*, 584:574–578.
- Larour, E., Rignot, E., Poinelli, M., and Scheuchl, B. (2021). Physical processes controlling the rifting of larsen c ice shelf, antarctica, prior to the calving of iceberg a68. *Proceedings of the National Academy of Sciences of the United States of America*, 118.
- Lazzara, M. A., Jezek, K. C., Scambos, T. A., Macayeal, D. R., and Veen, C. J. V. D. (2008). On the recent calving of icebergs from the ross ice shelf on the recent calving of icebergs from the ross ice shelf. *Polar Geography*.
- Lemaitre, J. (2012). *A Course on Damage Mechanics*. Springer Berlin, 2 edition.
- Levermann, A., Albrecht, T., Winkelmann, R., Martin, M. A., Haseloff, M., and Joughin, I. (2012). Kinematic first-order calving law implies potential for abrupt ice-shelf retreat. *Cryosphere*, 6:273–286.
- Levermann, A. and Feldmann, J. (2019). Scaling of instability timescales of antarctic outlet glaciers based on one-dimensional similitude analysis. *The Cryosphere*, 13:1621–1633.
- Lhermitte, S., Sun, S., Shuman, C., Wouters, B., Pattyn, F., Wuite, J., Berthier, E., and Nagler, T. (2020). Damage accelerates ice shelf instability and mass loss in amundsen sea embayment. *Proceedings of the National Academy of Sciences*, page 201912890.
- Li, G., Guo, J., Pei, L., Zhang, S., Tang, X., and Yao, J. (2021). Extraction and analysis of the three-dimensional features of crevasses in the amery ice shelf based on icesat-2 atl06 data. *IEEE Sensors Journal*, 14.
- Libert, L., Wuite, J., and Nagler, T. (2022). Automatic delineation of cracks with sentinel-1 interferometry for monitoring ice shelf damage and calving. *The Cryosphere*, 16:1523–1542.
- Lilien, D. A., Joughin, I., Smith, B., and Shean, D. E. (2018). Changes in flow of crosson and dotson ice shelves, west antarctica, in response to elevated melt. *The Cryosphere*, 12:1415–1431.
- Lipovsky, B. P. (2018). Ice shelf rift propagation and the mechanics of wave-induced fracture. *Journal of Geophysical Research: Oceans*, 123:4014–4033.
- Lipscomb, W. H., Leguy, G. R., Jourdain, N. C., Asay-Davis, X., Seroussi, H., and Nowicki, S. (2021). Ismip6-based projections of ocean-forced antarctic ice sheet evolution using the community ice sheet model. *The Cryosphere*, 15:633–661.
- Liu, Y., Cheng, X., Hui, F. M., Wang, X. W., Wang, F., and Cheng, C. (2014). Detection of crevasses over polar ice shelves using satellite laser altimeter. *Science China Earth Sciences*, 57:1267–1277.

- Liu, Y., Moore, J. C., Cheng, X., Gladstone, R. M., Bassis, J. N., Liu, H., Wen, J., and Hui, F. (2015). Ocean-driven thinning enhances iceberg calving and retreat of antarctic ice shelves. *Proceedings of the National Academy of Sciences of the United States of America*, 112:3263–3268.
- Luckman, A., Jansen, D., Kulesa, B., King, E. C., Sammonds, P., and Benn, D. I. (2012). Basal crevasses in larsen c ice shelf and implications for their global abundance. *Cryosphere*, 6:113–123.
- Iv, D., Cheng, Y., Xiao, H., and Hai, G. (2022). A framework for fracture extraction under glaciological property-based constraints: Scientific application on the filchner–ronne ice shelf of antarctica. *Earth and Space Science*, 9.
- Massom, R. A., Scambos, T. A., Bennetts, L. G., Reid, P., Squire, V. A., and Stammerjohn, S. E. (2018). Antarctic ice shelf disintegration triggered by sea ice loss and ocean swell. *Nature*, 558:383–389.
- Matsuoka, K., Skoglund, A., Roth, G., de Pomereu, J., Griffiths, H., Headland, R., Herried, B., Katsumata, K., Brocq, A. L., Licht, K., Morgan, F., Neff, P., Ritz, C., Scheinert, M., Tamura, T., de Putte, A. V., van den Broeke, M., von Deschanden, A., Deschamps-Berger, C., Liefveringe, B. V., Tronstad, S., and Melvær, Y. (2018). Quantarctica [dataset].
- McGrath, D., Steffen, K., Rajaram, H., Scambos, T., Abdalati, W., and Rignot, E. (2012a). Basal crevasses on the larsen c ice shelf, antarctica: Implications for meltwater ponding and hydrofracture. *Geophysical Research Letters*, 39:n/a–n/a.
- McGrath, D., Steffen, K., Scambos, T., Rajaram, H., Casassa, G., and Lagos, J. L. R. (2012b). Basal crevasses and associated surface crevassing on the larsen c ice shelf, antarctica, and their role in ice-shelf instability. *Annals of Glaciology*, 53:1–18.
- Meredith, M., Sommerkorn, M., Cassotta, S., Derksen, C., Ekaykin, A., Hollowed, A., Kofinas, G., Mackintosh, A., Melbourne-Thomas, J., Muelbert, M., Ottersen, G., Pritchard, H. D., and Schuur, E. (2019). *Polar regions*, pages 203–320. In Press.
- Miles, B. W. J., Stokes, C. R., Jenkins, A., Jordan, J. R., Jamieson, S. S. R., and Gudmundsson, G. H. (2021). Intermittent structural weakening and acceleration of the thwaites glacier tongue between 2000 and 2018. *Journal of Glaciology*, 66:485–495.
- Millan, R., Jager, E., Mouginot, J., Wood, M. H., Larsen, S. H., Mathiot, P., Jourdain, N. C., and Bjørk, A. (2023). Rapid disintegration and weakening of ice shelves in north greenland. *Nature Communications*, 14.
- Mobasher, M. E., Duddu, R., Bassis, J. N., and Waisman, H. (2016). Modeling hydraulic fracture of glaciers using continuum damage mechanics. *Journal of Glaciology*, 62:794–804.
- Morlighem, M., Bondzio, J., Seroussi, H., Rignot, E., Larour, E., Humbert, A., and Rebuffi, S. (2016). Modeling of store gletscher’s calving dynamics, west greenland, in response to ocean thermal forcing. *Geophysical Research Letters*, 43:2659–2666.
- Mouginot, J., Rignot, E., Scheuchl, B., and Millan, R. (2017a). Comprehensive annual ice sheet velocity mapping using landsat-8, sentinel-1, and radarsat-2 data. *Remote Sensing*, 9.
- Mouginot, J., Scheuchl, B., and Rignot, E. (2017b). Measures antarctic boundaries for ipy 2007–2009 from satellite radar, version 2. *NASA National Snow and Ice Data Center Distributed Active Archive Center*.
- Murakami, S., Kawai, M., and Rong, H. (1988). Finite element analysis of creep crack growth by a local approach. *International Journal of Mechanical Sciences*, 30:491–502.
- Naughten, K. A., Holland, P. R., and Rydt, J. D. (2023). Unavoidable future increase in west antarctic ice-shelf melting over the twenty-first century. *Nature Climate Change*, 13:1222–1228.
- Naughten, K. A., Rydt, J. D., Rosier, S. H., Jenkins, A., Holland, P. R., and Ridley, J. K. (2021). Two-timescale response of a large antarctic ice shelf to climate change. *Nature Communications*, 12.
- Nawar, S. and Mouazen, A. (2017). Comparison between random forests, artificial neural networks and gradient boosted machines methods of on-line vis-nir spectroscopy measurements of soil total nitrogen and total carbon. *Sensors*, 17:2428.
- Nowicki, S., Goelzer, H., Seroussi, H., Payne, A. J., Lipscomb, W. H., Abe-Ouchi, A., Agosta, C., Alexander, P., Asay-Davis, X. S., Barthel, A., Bracegirdle, T. J., Cullather, R., Felikson, D., Fettweis, X., Gregory, J. M., Jourdain, N. C., Munneke, P. K., Larour, E., Little, C. M., Morlighem, M., Nias, I., Shepherd, A., Simon, E., Slater, D., Smith, R. S., Straneo, F., Trusel, L. D., Broeke, M. R. V. D., and Wal, R. V. D. (2020). Experimental protocol for sea level projections from ismip6 stand-alone ice sheet models. *Tore Hattermann*, 14.
- Nowicki, S., Simon, E., and ISMIP6, T. (2021). Ismip6 21st century antarctic projections.
- Nye, J. F. and Wills, H. H. (1957). The distribution of stress and velocity in glaciers and ice-sheets. *Proceedings of the Royal Society of London. Series A. Mathematical and Physical Sciences*, 239:113–133.
- Ochwat, N. E., Scambos, T. A., Banwell, A. F., Anderson, R. S., MacLennan, M. L., Picard, G., Shates, J. A., Marinsek, S., Margonari, L., Truffer, M., and Pettit, E. C. (2023). Triggers of the 2022 larsen b multi-year landfast sea ice break-out and initial glacier response. *The Cryosphere Discussions*, 2023:1–34.
- Oppenheim, A. V. and Willsky, A. S. (1996). *Signal Systems*. Prentice Hall Signal Processing Series, 2 edition.

-
- Pang, A., Liang, Q., Li, W., Zheng, L., Li, T., and Cheng, X. (2023). The distribution and evolution of surface fractures on pan-antarctic ice shelves. *International Journal of Digital Earth*, 16:3295–3320.
- Paolo, F. S., Fricker, H. A., and Padman, L. (2015). Volume loss from antarctic ice shelves is accelerating. *Science*, 348.
- Pattyn, F., Favier, L., Sun, S., and Durand, G. (2017). Progress in numerical modeling of antarctic ice-sheet dynamics. *Curr Clim Change Rep*, 3:174–184.
- Pattyn, F. and Morlighem, M. (2020). The uncertain future of the antarctic ice sheet. *Science*, 367:1331–1335.
- Ploton, P., Mortier, F., Réjou-Méchain, M., Barbier, N., Picard, N., Rossi, V., Dormann, C., Cornu, G., Viennois, G., Bayol, N., Lyapustin, A., Gourlet-Fleury, S., and Pélissier, R. (2020). Spatial validation reveals poor predictive performance of large-scale ecological mapping models. *Nature Communications*, 11.
- Poinelli, M., Schodlok, M., Larour, E., Vizcaino, M., and Riva, R. (2023). Can rifts alter ocean dynamics beneath ice shelves? *Cryosphere*, 17:2261–2283.
- Pollard, D. and DeConto, R. M. (2016). Contribution of antarctica to past and future sea-level rise. *Nature*, 531:591–597.
- Porter, C., Morin, P., Howat, I., Noh, M.-J., Bates, B., Peterman, K., Keesey, S., Schlenk, M., Gardiner, J., Tomko, K., Willis, M., Kelleher, C., Cloutier, M., Husby, E., Foga, S., Nakamura, H., Platson, M., Michael, J. W., Williamson, C., Bauer, G., Enos, J., Arnold, G., Kramer, W., Becker, P., Doshi, A., D'Souza, C., Cummins, P., Laurier, F., and Bojesen, M. (2018). Arcticdem, version 3.
- Pralong, A. and Funk, M. (2005). Dynamic damage model of crevasse opening and application to glacier calving. *Journal of Geophysical Research*, 110:B01309.
- Pralong, A., Funk, M., and Luthi, M. P. (2003). A description of crevasse formation using continuum damage mechanics. *Annals of Glaciology*.
- Pralong, A., Hutter, K., and Funk, M. (2006). Anisotropic damage mechanics for viscoelastic ice. *Continuum Mech. Thermodyn*, 17:387–408.
- Rack, W. and Rott, H. (2004). Pattern of retreat and disintegration of the larsen b ice shelf, antarctic peninsula. *Annals of Glaciology*.
- Reese, R., Gudmundsson, G. H., Levermann, A., and Winkelmann, R. (2017). The far reach of ice-shelf thinning in antarctica. *Nature Climate Change*.
- Rignot, E. (1998). Fast recession of a west antarctic glacier. *Science*, 281.
- Rignot, E., Jacobs, S., Mouginot, J., and Scheuchl, B. (2013). Ice-shelf melting around antarctica. *Science*, 341:266–270.
- Rignot, E., Mouginot, J., and Scheuchl, B. (2016). Measures antarctic grounding line from differential satellite radar interferometry, version 2. *NASA National Snow and Ice Data Center Distributed Active Archive Center*.
- Ritz, C., Edwards, T. L., Durand, G., Payne, A. J., Peyaud, V., and Hindmarsh, R. C. (2015). Potential sea-level rise from antarctic ice-sheet instability constrained by observations. *Nature*, 528.
- Robel, A. A. and Banwell, A. F. (2019). A speed limit on ice shelf collapse through hydrofracture. *Geophysical Research Letters*, 46.
- Robel, A. A., Seroussi, H., and Roe, G. H. (2019). Marine ice sheet instability amplifies and skews uncertainty in projections of future sea-level rise. *Proceedings of the National Academy of Sciences of the United States of America*, 116.
- Roberts, D. R., Bahn, V., Ciuti, S., Boyce, M. S., Elith, J., Guillera-Arroita, G., Hauenstein, S., Lahoz-Monfort, J. J., Schröder, B., Thuiller, W., Warton, D. I., Wintle, B. A., Hartig, F., and Dormann, C. F. (2017). Cross-validation strategies for data with temporal, spatial, hierarchical, or phylogenetic structure. *Ecography*, 40:913–929.
- Roberts, J. L., Warner, R. C., and Treverrow, A. (2013). Instruments and methods inferring ice-flow directions from single ice-sheet surface images using the radon transform. *Journal of Glaciology*, 59:129–136.
- Rott, H., Jaber, W. A., Wuite, J., Scheiblauer, S., Floricioiu, D., van Wessem, J. M., Nagler, T., Miranda, N., and van den Broeke, M. R. (2018). Changing pattern of ice flow and mass balance for glaciers discharging into the larsen a and b embayments, antarctic peninsula, 2011 to 2016. *The Cryosphere*, 12:1273–1291.
- Roßbach, P. (2018). Neural networks vs. random forests-does it always have to be deep learning?
- Rydt, J. D., Gudmundsson, G. H., Nagler, T., and Wuite, J. (2019). Calving cycle of the brunt ice shelf, antarctica, driven by changes in ice shelf geometry. *Cryosphere*, 13:2771–2787.
- Rydt, J. D., Gudmundsson, G. H., Nagler, T., Wuite, J., and King, E. C. (2018). Recent rift formation and impact on the structural integrity of the brunt ice shelf, east antarctica. *Cryosphere*, 12:505–520.
- Rydt, J. D., Reese, R., Paolo, F. S., and Gudmundsson, G. H. (2021). Drivers of pine island glacier speed-up between 1996 and 2016. *Cryosphere*, 15:113–132.
- Scambos, T., Fricker, H. A., Liu, C.-C. C., Bohlander, J., Fastook, J., Sargent, A., Massom, R., and Wu, A.-M. M. (2009). Ice shelf disintegration by plate bending and hydro-fracture: Satellite observations and model results of the 2008 wilkins ice shelf break-ups. *Earth and Planetary Science Letters*, 280:51–60.

- Scambos, T. A., Bell, R. E., Alley, R. B., Anandakrishnan, S., Bromwich, D. H., Brunt, K., Christianson, K., Creyts, T., Das, S. B., DeConto, R., Dutrieux, P., Fricker, H. A., Holland, D., MacGregor, J., Medley, B., Nicolas, J. P., Pollard, D., Siegfried, M. R., Smith, A. M., Steig, E. J., Trusel, L. D., Vaughan, D. G., and Yager, P. L. (2017). How much, how fast?: A science review and outlook for research on the instability of antarctica's thwaites glacier in the 21st century.
- Schlegel, N.-J., Seroussi, H., Schodlok, M. P., Larour, E. Y., Boening, C., Limonadi, D., Watkins, M. M., Morlighem, M., and van den Broeke, M. R. (2018). Exploration of antarctic ice sheet 100-year contribution to sea level rise and associated model uncertainties using the issm framework. *The Cryosphere*, 12:3511–3534.
- Seroussi, H., Nowicki, S., Payne, A. J., Goelzer, H., Lipscomb, W. H., Abe-Ouchi, A., Agosta, C., Albrecht, T., Asay-Davis, X., Barthel, A., Calov, R., Cullather, R., Dumas, C., Galton-Fenzi, B. K., Gladstone, R., Gollledge, N. R., Gregory, J. M., Greve, R., Hattermann, T., Hoffman, M. J., Humbert, A., Huybrechts, P., Jourdain, N. C., Kleiner, T., Larour, E., Leguy, G. R., Lowry, D. P., Little, C. M., Morlighem, M., Pattyn, F., Pelle, T., Price, S. F., Quiquet, A., Reese, R., Schlegel, N.-J., Shepherd, A., Simon, E., Smith, R. S., Straneo, F., Sun, S., Trusel, L. D., Breedam, J. V., van de Wal, R. S. W., Winkelmann, R., Zhao, C., Zhang, T., and Zwinger, T. (2020). Ismip6 antarctica: a multi-model ensemble of the antarctic ice sheet evolution over the 21st century. *The Cryosphere*, 14:3033–3070.
- Seroussi, H., Verjans, V., Nowicki, S., Payne, A. J., Goelzer, H., Lipscomb, W. H., Abe-Ouchi, A., Agosta, C., Albrecht, T., Asay-Davis, X., Barthel, A., Calov, R., Cullather, R., Dumas, C., Galton-Fenzi, B. K., Gladstone, R., Gollledge, N. R., Gregory, J. M., Greve, R., Hattermann, T., Hoffman, M. J., Humbert, A., Huybrechts, P., Jourdain, N. C., Kleiner, T., Larour, E., Leguy, G. R., Lowry, D. P., Little, C. M., Morlighem, M., Pattyn, F., Pelle, T., Price, S. F., Quiquet, A., Reese, R., Schlegel, N. J., Shepherd, A., Simon, E., Smith, R. S., Straneo, F., Sun, S., Trusel, L. D., Breedam, J. V., Katwyk, P. V., van de Wal, R. S., Winkelmann, R., Zhao, C., Zhang, T., and Zwinger, T. (2023). Insights into the vulnerability of antarctic glaciers from the ismip6 ice sheet model ensemble and associated uncertainty. *Cryosphere*, 17:5197–5217.
- Shalom, S. R. and Mandeville, G. (1982). Calculating minimum and maximum possible variances from n-tile grouped data. *Quality and Quantity*, 16:19–27.
- Shepherd, A., Ivins, E., Rignot, E., Smith, B., Broeke, M. V. D., Velicogna, I., Whitehouse, P., Briggs, K., Joughin, I., Krinner, G., Nowicki, S., Payne, T., Scambos, T., Schlegel, N., Geruo, A., Agosta, C., Ahlstrøm, A., Babonis, G., Barletta, V., Blazquez, A., Bonin, J., Csatho, B., Cullather, R., Felikson, D., Fettweis, X., Forsberg, R., Gallee, H., Gardner, A., Gilbert, L., Groh, A., Gunter, B., Hanna, E., Harig, C., Helm, V., Horvath, A., Horwath, M., Khan, S., Kjeldsen, K. K., Konrad, H., Langen, P., Lecavalier, B., Loomis, B., Luthcke, S., McMillan, M., Melini, D., Mernild, S., Mohajerani, Y., Moore, P., Mouginot, J., Moyano, G., Muir, A., Nagler, T., Nield, G., Nilsson, J., Noel, B., Otsuka, I., Pattle, M. E., Peltier, W. R., Pie, N., Rietbroek, R., Rott, H., Sandberg-Sørensen, L., Sasgen, I., Save, H., Scheuchl, B., Schrama, E., Schröder, L., Seo, K. W., Simonsen, S., Slater, T., Spada, G., Sutterley, T., Talpe, M., Tarasov, L., Berg, W. J. V. D., Wal, W. V. D., Wessem, M. V., Vishwakarma, B. D., Wiese, D., and Wouters, B. (2018). Mass balance of the antarctic ice sheet from 1992 to 2017. *Nature*, 558.
- Siahaan, A., Smith, R. S., Holland, P. R., Jenkins, A., Gregory, J. M., Lee, V., Mathiot, P., Payne, A. J., Ridley, J. K., and Jones, C. G. (2022). The antarctic contribution to 21st-century sea-level rise predicted by the uk earth system model with an interactive ice sheet. *The Cryosphere*, 16:4053–4086.
- Silvano, A., Rintoul, S. R., Peña-Molino, B., Hobbs, W. R., van Wijk, E., Aoki, S., Tamura, T., and Williams, G. D. (2018). Freshening by glacial meltwater enhances melting of ice shelves and reduces formation of antarctic bottom water. *Science Advances*, 4:eap9467.
- Smith, R. A. (1976). The application of problem of fracture mechanics crevasse penetration. *Journal of Glaciology*, 17.
- Stehman, S. V. (1997). Selecting and interpreting measures of thematic classification accuracy. *Remote Sensing of Environment*, 62:77–89.
- Sun, S., Cornford, S. L., Moore, J. C., Gladstone, R., and Zhao, L. (2017). Ice shelf fracture parameterization in an ice sheet model. *The Cryosphere*, 11:2543–2554.
- Sun, S., Pattyn, F., Simon, E. G., Albrecht, T., Cornford, S., Calov, R., Dumas, C., Gillet-Chaulet, F., Goelzer, H., Gollledge, N. R., Greve, R., Hoffman, M. J., Humbert, A., Kazmierczak, E., Kleiner, T., Leguy, G. R., Lipscomb, W. H., Martin, D., Morlighem, M., Nowicki, S., Pollard, D., Price, S., Quiquet, A., Seroussi, H., Schlemm, T., Sutter, J., Wal, R. S. W. V. D., Winkelmann, R., and Zhang, T. (2020). Antarctic ice sheet response to sudden and sustained ice-shelf collapse (abumip). *Journal of Glaciology*, 66:891–904.
- Surawy-Stepney, T., Hogg, A. E., Cornford, S. L., and Davison, B. J. (2023a). Episodic dynamic change linked to damage on the thwaites glacier ice tongue. *Nature Geoscience*, 16:37–43.
- Surawy-Stepney, T., Hogg, A. E., Cornford, S. L., and Hogg, D. C. (2023b). Mapping antarctic crevasses and their evolution with deep learning applied to satellite radar imagery. *The Cryosphere*, 17:4421–4445.
- Taha, A. A. and Hanbury, A. (2015). Software open access metrics for evaluating 3d medical image segmentation: analysis, selection, and tool. *BMC Medical Imaging*, 15:29.

- Team, Q. D. (2009). Qgis geographic information system.
- Tinto, K. J. and Bell, R. E. (2011). Progressive unpinning of thwaites glacier from newly identified offshore ridge: Constraints from aerogravity. *Geophysical Research Letters*, 38.
- Tollenaar, V., Zekollari, H., Pattyn, F., Rußwurm, M., Kellenberger, B., Lhermitte, S., Izeboud, M., and Tuia, D. (2024). Where the white continent is blue: Deep learning locates bare ice in antarctica. *Geophysical Research Letters*, 51.
- van de Wal, R. S., Nicholls, R. J., Behar, D., McInnes, K., Stammer, D., Lowe, J. A., Church, J. A., DeConto, R., Fettweis, X., Goelzer, H., Haasnoot, M., Haigh, I. D., Hinkel, J., Horton, B. P., James, T. S., Jenkins, A., LeCozannet, G., Levermann, A., Lipscomb, W. H., Marzeion, B., Pattyn, F., Payne, A. J., Pfeffer, W. T., Price, S. F., Seroussi, H., Sun, S., Veatch, W., and White, K. (2022). A high-end estimate of sea level rise for practitioners. *Earth's Future*, 10.
- Vaughan, D. G. (1993). Relating the occurrence of crevasses to surface strain rates. *Journal of Glaciology*, 39.
- Vaughan, D. G., Corr, H. F. J., Bindshadler, R. A., Dutrieux, P., Gudmundsson, G. H., Jenkins, A., Newman, T., Vornberger, P., Wingham, D. J., Vaughan, D. G., Corr, H. F. J., Bindshadler, R. A., Dutrieux, P., Gudmundsson, G. H., Jenkins, A., Newman, T., Vornberger, P., and Wingham, D. J. (2012). Subglacial melt channels and fracture in the floating part of pine island glacier. *Journal of Geophysical Research: Earth Surface*, 117:3012.
- Veen, C. J. V. D. (1998a). Fracture mechanics approach to penetration of bottom crevasses on glaciers. *Cold Regions Science and Technology*, 27:213–223.
- Veen, C. J. V. D. (1998b). Fracture mechanics approach to penetration of surface crevasses on glaciers. *Cold Regions Science and Technology*, 27:31–47.
- Veldhuijsen, S. B. M., van de Berg, W. J., Munneke, P. K., and van den Broeke, M. R. (2023). Evolution of antarctic firn air content under three future warming scenarios. *EGU Sphere*, 2023:1–27.
- Vieli, A., Payne, A. J., Shepherd, A., and Du, Z. (2007). Causes of pre-collapse changes of the larsen b ice shelf: Numerical modelling and assimilation of satellite observations. *Earth and Planetary Science Letters*, 259:297–306.
- Vries, M. V. W. D., Lea, J. M., and Ashmore, D. W. (2023). Crevasse density, orientation and temporal variability at narsap sermia, greenland. *Journal of Glaciology*, 64.
- Wang, S., Alexander, P., Wu, Q., Tedesco, M., and Shu, S. (2021). Characterization of ice shelf fracture features using icesat-2 – a case study over the amery ice shelf. *Remote Sensing of Environment*, 255:112266.
- Weertman, J. (1974). Stability of the junction of an ice sheet and an ice shelf. *Journal of GlacioJoD*, 13.
- Weertman, J. (1980). Bottom crevasses. *Journal of Glaciology*, 25.
- Wild, C. T., Alley, K. E., Muto, A., Truffer, M., Scambos, T. A., and Pettit, E. C. (2022). Weakening of the pinning point buttressing thwaites glacier, west antarctica. *Cryosphere*, 16:397–417.
- Wille, J. D., Favier, V., Jourdain, N. C., Kittel, C., Turton, J. V., Agosta, C., Gorodetskaya, I. V., Picard, G., Codron, F., Santos, C. L. D., Amory, C., Fettweis, X., Blanchet, J., Jomelli, V., and Berchet, A. (2022). Intense atmospheric rivers can weaken ice shelf stability at the antarctic peninsula. *Communications Earth and Environment*, 3.
- Wilner, J. A., Morlighem, M., and Cheng, G. (2023). Evaluation of four calving laws for antarctic ice shelves. *The Cryosphere*, 17:4889–4901.
- Winkelmann, R., Martin, M. A., Haseloff, M., Albrecht, T., Bueler, E., Khroulev, C., and Levermann, A. (2011). The potsdam parallel ice sheet model (pism-pik) – part 1: Model description. *The Cryosphere*, 5:715–726.
- Zhao, J., Liang, S., Li, X., Duan, Y., and Liang, L. (2022). Detection of surface crevasses over antarctic ice shelves using sar imagery and deep learning method. *Remote Sensing 2022*, Vol. 14, Page 487, 14:487.
- Zinck, A.-S. P., Wouters, B., Lambert, E., and Lhermitte, S. (2023). Unveiling spatial variability within the dotson melt channel through high-resolution basal melt rates from the reference elevation model of antarctica. *The Cryosphere*, 17:3785–3801.
- Öznergiz, E., Kiyak, Y. E., Kamasak, M. E., and Yildirim, I. (2014). Automated nanofiber diameter measurement in sem images using a robust image analysis method. *Journal of Nanomaterials*, 2014.



Acknowledgements

*“What do you think success is?” asked the boy.
“To love,” said the mole.*

Charlie Mackesy,
The Boy, the Mole, the Fox and the Horse

As I reflect on the journey that led to this dissertation, I am reminded of a comment made by my teacher when I was around eight years old. After submitting my first, handwritten report (on Leopards, my favourite animal), I was told *“it’s obvious that you’ve had quite some help”*. Back then, I felt indignant – I had done the work all by myself! But now, as I complete this work, I hope it’s evident how much help I’ve had in order to get to this point. What once felt like a slight, would now be a compliment I would cherish, as it reflects the incredible support I’ve received. I am extremely grateful to everyone who has contributed to this journey, and I’ll do my best to acknowledge you here.

First and foremost, my heartfelt thanks go to my supervisor, **Stef**. Your enthusiasm is what drew me to study the cryosphere in the first place, and your positive attitude and endless creativity is what made me decide to pursue this PhD with you. I am very happy that I did, and I hope Proposition #6 makes that clear. Thank you for your trust and support all these years, for listening to me and for pushing me, and for wanting to provide the best opportunities for my future. I am especially grateful for the the extraordinary chance to participate in Antarctic fieldwork, an experience that will forever stay with me. I expect to, and look forward to, keeping collaborating in the future.

I would like to thank the examination committee, **Elmar Eisemann, Anna Hogg, Roderik van de Wal, Roderik Lindenbergh, and Bert Wouters**, for the time they have taken to assess this thesis, and I am grateful for their role in helping to bring this work to completion. I specifically want to thank **Ramon Hanssen** for his role as promotor and for the valuable, critical discussions we’ve had about the project. Furthermore, I have had the privilege of learning a great deal about machine learning from **Sonja, Meiert, Ou, and Francesco** at the eScience Center, and collaborating with them has been a pleasure.

I also want to acknowledge that **the cryosphere community** has been a very welcoming and fun group of amazing, vibrant people. I was fortunate to meet and/or collaborate with excellent scientists within this community, including, but not limited to: **my co-authors**, the people at **Karthaus**, the people from **IMAU** in Utrecht, from **ULB** and **VUB** in Brussels, and from **CU Boulder** in Colorado, and many more. Thank you for your company, assistance, and inspiration!

Next, I want to thank my **colleagues at GRS**, without whom I was lost during the COVID pandemic when we all had to quarantine at home, and who will be missed dearly now that I’ll be leaving. I’ll cherish our coffee breaks, PSOR breaks, and the open atmosphere

in the best office of the building. **Sophie**, my collaborator, my cheerleader, my copy: I am so glad to have had you by my side, I couldn't have done it without you. I really hope we get another chance to share hotel rooms in future conferences. **Ann-Sofie** and **Wietske**, my two power women, thank you for keeping me sane – if it is through cocktails, mental health discussions or through adventure races, I loved sharing this journey with you. Thank you **Debbie, Natascha and Cindy** (and not to forget, Suzanne and Lidwien) for supporting this jumble of a department.

Then, most important in my life, the people close to me. **Mom and Dad**, thank you for always supporting my decisions, my dreams, and my failures. Growing up, I've always felt trusted and understood. This has made me independent and confident, something that has got me here today. Thank you for the relentless questions and interest. **Petra**, my *rots in de branding*, thank you for being so full of love and spirit. You are my role model in life, which makes me proud when people say we are so alike. I am very happy that you brought Rens, Tibbe, Roan and Eska into our family. **Daan**, thank you for supporting me all these years, for listening and keeping me grounded in stressful times, or for standing up for me when necessary. You have been a steadfast source of strength, and I am grateful for your belief in me and the calm confidence you bring to my life.

Lastly, but never least, my friends!! Your laughter, support, and chaos have made all the difference, ensuring that I never lose sight of what truly matters in life. **Berna, Danielle, Denise, Iris, Iris, Isabelle, Katinka, Maaïke, Marloes, Priska, Tine, Veronica, Willemijn**, and all the others, there's not enough room to go into detail, but know I love you.

List of paintings

If you could explain something perfectly,
you'd never need art.

Brandon Sanderson,
Oathbringer, The Stormlight Archive

Watercolor paintings at chapter opening pages were made by the author during the Mass2Ant fieldwork expedition in Antarctica, December-January 2021-2022.

Contents (page vi)	Flags indicating the area of clean snow that is used for drinking water.
Chapter 1 (page 6)	Impression of Lokeryggen Ice Rise, field location of the Mass2Ant expedition.
Chapter 2 (page 22)	The Belgian research station, Princes Elisabeth Antarctica (PEA), seen from a short walking distance South.
Chapter 3 (page 52)	Utsteinen nunatak next to PEA, seen from the West side.
Chapter 4 (page 66)	Sarah Wauthy and Marie Cavitte on their way back to the <i>caboose</i> in a wind storm.
Chapter 5 (page 80)	Vesthaugen nunatak, seen during the traverse back from the field to PEA.
Appendix (page 88)	Impression of the view from inside a snow covered crevasse to the top, while being 'rescued' during training.
Backmatter (page 118)	Romneus nunatak, seen during the traverse between PEA and Lokeryggen ice rise.

Curriculum Vitae

30 Januari, 1994 Born in Vlissingen, the Netherlands

2006-2012 **S.S.G. 'Nehalennia' secondary education**
Middelburg, the Netherlands

2012-2015 **Bachelor of Science in Civil Engineering**
Delft University of Technology
Minor: Applied Physics & Applied Math
Bachelor thesis: Modelling surface waters of Rotterdam Zoo

2016-2019 **Master of Science in Civil Engineering**
Delft University of Technology
Master discipline: Geoscience and Remote Sensing
Master thesis: Cloud Radiative Effect on Antarctic Ice Shelves

2019 **Researcher**
Delft University of Technology
Department of Geoscience and Remote Sensing
Topic: Cloud Radiative Effect on the Greenland Ice Sheet

2019-2024 **Doctoral Candidate**
Delft University of Technology
Department of Geoscience and Remote Sensing

ORCID-ID: 0000-0002-8915-7252

List of publications and presentations

Publications

First author

- **M. Izeboud**, S. Lhermitte, S. de Roda Husman, B. Wouters. Antarctic ice shelves vulnerable to damage in future climate warming, *In review in Nature Climate Change*, *NCLIM-24010280-T*, **2024**.
- **M. Izeboud**, S. Lhermitte (**2023**). Damage Detection on Antarctic Ice Shelves using the Normalised Radon Transform, *Remote Sensing of Environment*, 284, <https://doi.org/10.1016/j.rse.2022.113359>
- **M. Izeboud**, S. Lhermitte, K. van Tricht, J.T.M. Lenaerts, N.P.M. van Lipzig and N. Wever (**2020**). The Spatiotemporal Variability of Cloud Radiative Effects on the Greenland Ice Sheet Surface Mass Balance, *Geophysical Research Letters*, 47, <https://doi.org/10.1029/2020GL087315>

Co-author

- S. Shukla, B. Wouters, G. Picard, N. Wever, **M. Izeboud**, S. de Roda Husman, T. Kausch, S. Veldhuijsen, C. Mätzler, and S. Lhermitte (**2024**). Large Variability in Dominant Scattering from Sentinel-1 SAR in East Antarctica: Challenges and Opportunities, *IEEE JSTARS*, <https://doi.org/10.1109/JSTARS.2024.3438233>
- V. Tollenaar, H. Zekollari, F. Pattyn, M. Rußwurm, B. Kellenberger, S. Lhermitte, **M. Izeboud**, D. Tuia (**2024**). Where the White Continent is blue: deep learning locates bare ice in Antarctica, *Geophysical Research Letters*, 51, <https://doi.org/10.1029/2023GL106285>
- S. de Roda Husman, S. Lhermitte, J. Bolibar, **M. Izeboud**, Z. Hu, S. Shukla, M. van der Meer, D. Long, B. Wouters (**2024**). A High-Resolution Record of Surface Melt on Antarctic Ice Shelves using Multi-Source Remote Sensing Data and Deep Learning, “*Remote Sensing of the Global Cryosphere: Status, Processes, and Trends*” in *Remote Sensing of Environment*, <https://doi.org/10.1016/j.rse.2023.113950>
- Z. Hu, P. Kuipers Munneke, S. Lhermitte, **M. Izeboud**, and M. van den Broeke (**2021**). Improving Surface Melt Estimation over Antarctica Using Deep Learning: A Proof-of-Concept over the Larsen Ice Shelf, *The Cryosphere*, 15 (12), <https://doi.org/10.5194/tc-15-5639-2021>

Selected Presentations

- M. Izeboud and S. Lhermitte: Damage Feedback on Antarctic Ice Shelves: Observations and Future Scenarios, AGU Fall Meeting (C11A-04), San Francisco, United States, 11-15 December 2023.
- M. Izeboud and S. Lhermitte (**solicited**): Long-term and Short-term Damage Changes on Antarctic Ice Shelves, EGU General Assembly (CR3.4), Vienna, Austria, 24-28 April 2023.
- M. Izeboud and S. Lhermitte: Damage Change Detected on Antarctic Ice Shelves, Forum for Research into Ice Shelf Processes (FRISP), Northumberland, United Kingdom, 19-22 September 2022.